2016

Novel Photodynamic Cancer Therapy Agent and Biochemical Phosphate Sensor Based on Nanomaterials

Alaa Fadhel
University of Central Florida

NOVEL PHOTODYNAMIC CANCER THERAPY AGENT AND BIOCHEMICAL PHOSPHATE SENSOR BASED ON NANOMATERIALS

by
ALAA ABBAS FADHEL
University of Al-Nahrain, BSc 2002
University of Al-Nahrain, MSc 2005

A dissertation submitted in partial fulfillment of the requirements
for the degree of Doctor of Philosophy
in the Department of Chemistry
in the College of Science
at the University of Central Florida
Orlando, Florida

Spring Term
2016

Major Professor: Andres D. Campiglia & Kevin D. Belfield

ABSTRACT

Biochemical research and clinical studies have revolutionized the field of medicine in both diagnosis and therapy. Researchers in the field of biochemistry and biotechnology are using nanomaterials in different applications to develop devices and materials that offer benefits to both patients and the health care industry. These include biochemical sensors, enzyme encapsulation, biomarkers, and drug delivery improvements for the treatment of cancer. This dissertation focuses on investigating two biochemical aspects using nanomaterials; namely therapy and clinical diagnosis.

For therapy purposes, Silica nanoparticles were used as drug delivery system to develop a new photodynamic cancer therapy agent photo-acid generator (PAG) that selectively induces necrotic cell death of cancer cells. The developed PAG is oxygen-independent and - when excited at specific wavelengths - drops the pH within the lysosome of cancer cells to produce apoptosis/necrosis. It was specifically designed for *in vivo* applications and conjugated with synthesized, highly monodispersed silica nanoparticles (Si NPs) functionalized with amine groups via amid links (SiN-NH-PAG). Additional Features include high photo-acid quantum yield, high one-photon (1PA) and two-photon absorption (2PA) with low fluorescence quantum yield. *In vivo*, confocal microscope studies with HCT-116 (Human colorectal carcinoma) cancer cells showed that photodynamic processes in the presence of PAG were completed under one-photon absorption (1PA) conditions. In these experiments, cells were imaged at 1 min intervals for a total of 4 hours with the aid of Differential Interference Contrast (DIC). Among the photodynamic therapy agents tested via cytotoxicity experiments with the MTS assay, (SiN-NH-PAG) showed the best efficiency to induce cell death. The increased effectiveness of the new agent is probably due to the large number of PAG groups present on the surface of Si NPs.

Lysosome colocalization indicates that PAGs are mainly built in lysosomes. The increase of acidic content inside the lysosome was demonstrated with the aid of the LysoSensor Green probe. The drop in the intralysosomal pH was approximately 0.3 units. This is a desirable outcome as most cells underwent necrosis at pH $\leq$ 4.4. For clinical diagnosis purposes, a biochemical sensor was developed for the analysis of phosphate ions in urine samples. Abnormal levels of inorganic phosphate in human urine samples are related to the development of certain types of cancers affecting several organs of the human body, including breast, pancreas, lung and thyroid. The new biochemical sensor is based on the fluorescence energy transfer between a lanthanide luminescent probe $[Tb\text{-}EDTA]^{-1}$ and gold nanoparticles (Au NPs) capped with a Cetyltrimethylammonium bromide (CTAB) micelle. With this approach, it was possible to selectively determine inorganic phosphate (Pi) in urine samples at the micro-molar concentration level. Urine samples collected from healthy, non-smoking individuals showed no interference from concomitants usually found in human urine samples. The simplicity of analysis provides an approach well-suited for "real-time" monitoring of phosphate ions. Analysis time is made possible within approximately 10 min per sample.

ACKNOWLEDGMENTS

I would like to thank my research advisors, Dr. Kevin D. Belfield and Dr. Andres D. Campiglia for their guidance and support during my Ph.D. studies. Both professors gave me the opportunity to perform state-of-the-art research in their labs, attend scientific conferences and collaborate with different research groups at UCF. My work at UCF has made me proficient in Fluorescence Microscopy, laser spectroscopy, HPLC, Fluorescence Spectroscopy, light scattering measurements for nanoparticle characterization, NMR spectroscopy and LC-MS. My research at UCF has allowed me to gain a deep understanding of photodynamic cancer therapy, drug design and synthesis, cell culture, nanomaterials, biochemical sensing, clinical chemistry, medicinal and biochemistry, nanotechnology and bio-analytical chemistry. None of this would have been possible without the support of the Iraqi government and the Higher Committee for Education Development (HCED).

This work would have not been possible without the help and guidance of the following group members from Prof. Belfield's lab: Dr. Ghazvini Zadeh, Dr. Morales, Dr. Frazer, Dr. Bondar and Dr. Yue. The same is true for Dr. Koculi and the following members of Prof. Campiglia's lab: Dr. Moore, Dr. Alfarhani, Madeleine Johnson and Maha Al-Temeeme.

This dissertation is dedicated to my wife

Sarah

She has been a constant source of support and encouragement during the challenges of Doctoral study and I am really thankful for having her in my life

My lovely kids

Aya, Retag, and Laya

For inspiring me to not give up and finish the raise

My Parents, my Parents in law, and my brothers and sister

For their love, endless support and encouragement

TABLE OF CONTENTS

LIST OF FIGURES

LIST OF TABLES

LIST OF SCHEMES

CHAPTER 1. BACKGROUND

1.1 Cancer Diseases and Conventional Treatment Methods

Cancer is a group of diseases pertaining to abnormal cell growth with the possibility of spreading to other parts of the body.[1] Symptoms and signs associated with this disease are abnormal bleeding, a prolonged cough, unusual weight loss, and a change in bowel movements.[2] This disease is responsible for 7.6 million deaths (around 13% of all deaths) worldwide in 2008.[3] The conventional methods for cancer treatment are chemotherapy, surgery, and radiotherapy. However, chemotherapy treatment linked to a lot of problems and side effects. High reappearance rate is associated with tumors surgical resection, while radiation is limited based on cumulative radiation dose. Treatment with photodynamic therapy (PDT) is an alternative method for tumor-ablative and function-sparing oncologic intervention.

1.2 Photodynamic Therapy

Photodynamic therapy (PDT) treatment started in early 1900s and its first demonstration in 1975 by Dougherty et al[4] this method undergo wide investigations and has been developed as a disease site specific treatment modal. The basic mechanism for PDT involves the administration of a tumor-localizing photosensitizer (PS) followed by illumination of a tumor with light at a specific wavelength to excited the PS **(Figure 1-1)**. The activated PS transfers its energy to the oxygen generating cytotoxic reactive oxygen species (ROS) such as singlet oxygen ($^1O_2$) that attach to cellular macromolecules leading to death of the tumor cell. **Figure 1-2** represents stages of PDT: Stage I, injection of PS in the body; Stage II, chemicals concentrated

in the tumor site; Stage III, activated the PS using a light, and stage IIII, tumor selectively destroyed. Unlike chemotherapy PDT employs three components (photosensitizer, oxygen, and light), none of which have any toxic or damage effects on the neighboring normal tissues.

In the tissue, oxygen exists in the ground state as a triplet (nonreactive species). However, when light is absorbed by the photosensitizer at a certain wavelength, PS will be promoted to an excited state and transfer to a triplet state by intersystem crossing followed by energy transfer from the PS to oxygen and excited it into a reactive singlet state.

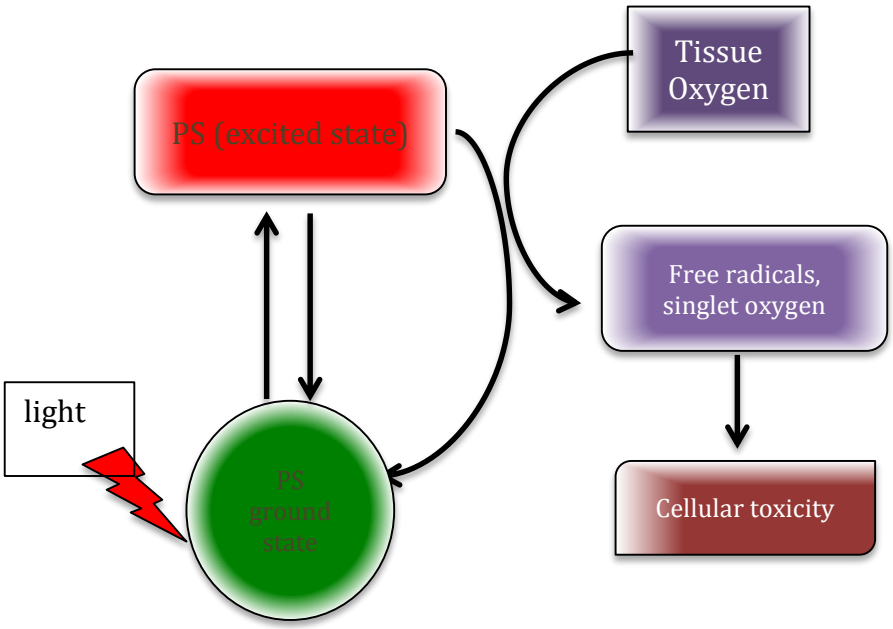

Figure 1-1. Schematic illustration of a typical photodynamic reaction based on photosensitizer (PS).

Currently, many photosensitizer compounds such as porphyrin, texaphyrin, and chlorin [5] have been used clinically to treat different kinds of cancer such as skin cancer, [6,7] bladder cancer,[8] lung cancer,[9] rectum and anus tumors.[10] Promising results were also shown in the treatment of brain tumors.[11]

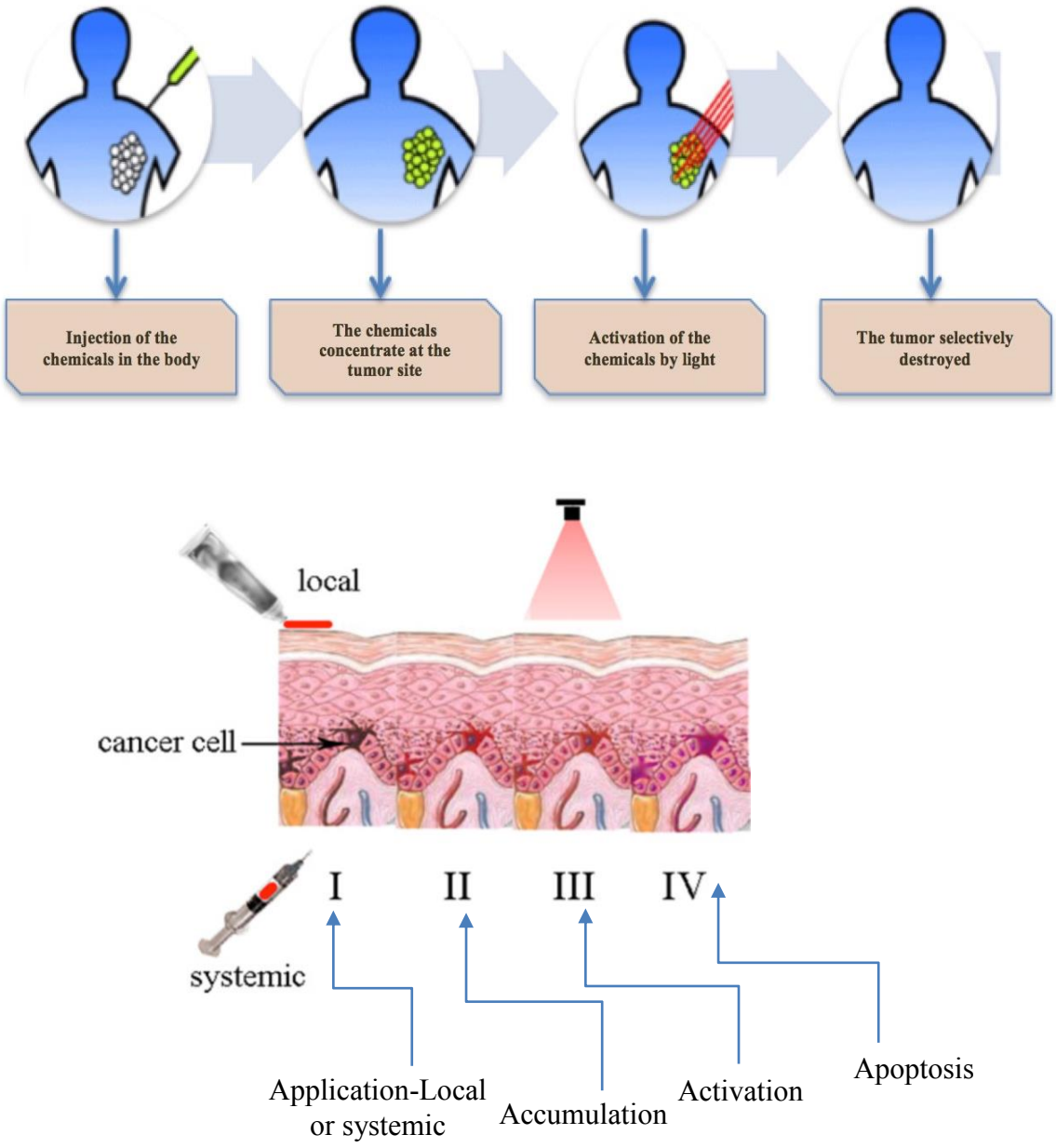

Figure 1-2. Photodynamic therapy principle stages. Photosensitizer (in syringe or tube) is injected locally or systemically (Stage I), accumulates in tumors (Stage II) and is then activated by external illumination (Stage III), and cell damage and death (Stage IIII).

1.3 Drug delivery and Nanoparticles

Most of the drugs are hydrophobic therefore undergo a lot of problems of delivery in blood circulation. As a result the efficacy of the therapeutic drug reduced. Many researches have been done to deliver the hydrophobic drugs more efficiently using different methods like encapsulating or conjugating them with nanoparticles. **Figure 1-3** shows examples of nanoparticles which are used to encapsulate drugs or conjugated drug molecules [12]. Conjugation or encapsulation of therapeutic drugs in nanoparticles has many advantages in comparison with drug alone. For example, Doxorubicin encapsulated in polyethylene glycol coated Liposomes (Doxil nanoparticles) have improved accumulation of doxorubicin and increased circulation time compared to free doxorubicin.[13]

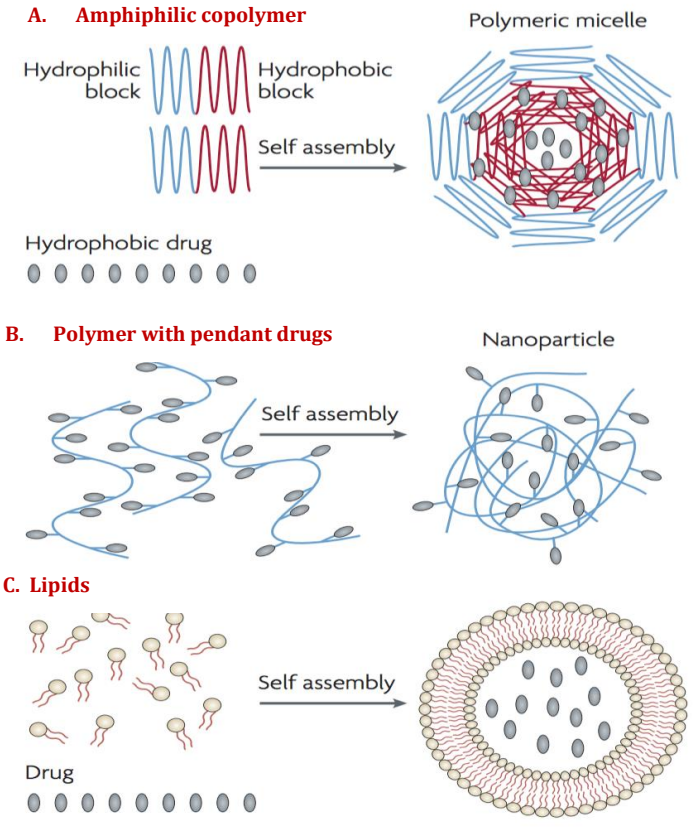

Figure 1-3. A. polymeric micelles encapsulating therapeutic agents B. polymers conjugated with therapeutic agents C. liposomes encapsulating therapeutic agents to enhance the pharmacokinetics and pharmacodynamics by active intracellular delivery. [12]

Quantum dots CdSe-ZnS, encapsulated in ABC triblock copolymer conjugated with tumor-targeting ligand and Poly ethylene glycol (PEG) were also used for drug delivery.[14] This probe was coated with PEG to enhance the circulation in the blood while the ABC triblock were used to protect the optical properties of Qdots in a broad variety of pH. The passive delivery for prostate cancer was achieved by improved the circulation of the probe due to PEG while the active delivery was achived by connecting the probe with prostate-specific membrane antigen (PSMA) monoclonal antibody. **Figures 1-4**, **1-5** show the development of the probe and the uptake of the probe in human prostate cancer cells that expressed and cells which do not express s PSMA. Another examples of using nanoparticles for cancer therapeutics is reported.[15] They used superpapamagnetic nanocrystals for MR imaging which encapsulated in silica nanoparticles and the anticancer drug was stored inside. Silica nanoparticles were coated with phosphonate to enhance the hydrophilicity and attached with folic acid to target the cancer cells. **Figure 1-6** shows the increasing in the uptake of nanoparticles conjugated with folic acid in PANC-1, which overexpresses folate receptors while HFF cells do not overexpress folate receptors.

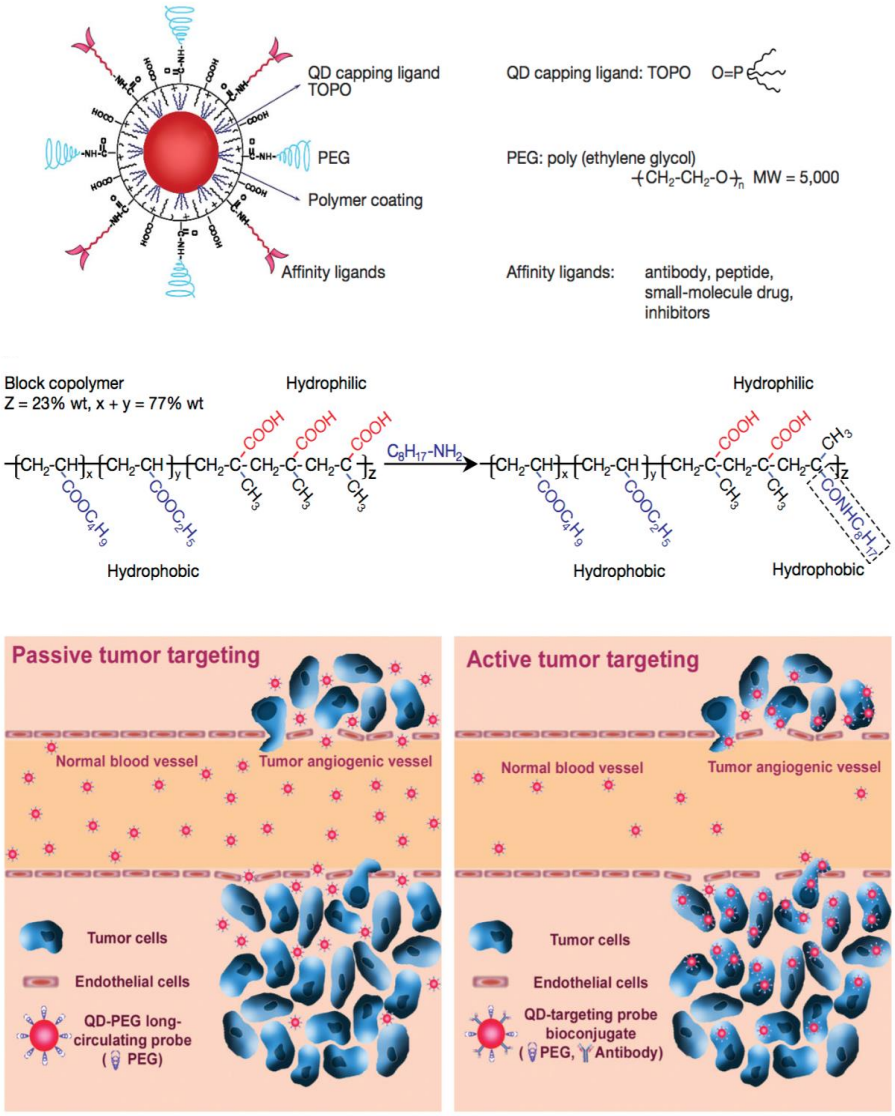

Figure 1-4. Qdots probe development and depiction of passive and active tumor targeting. [14]

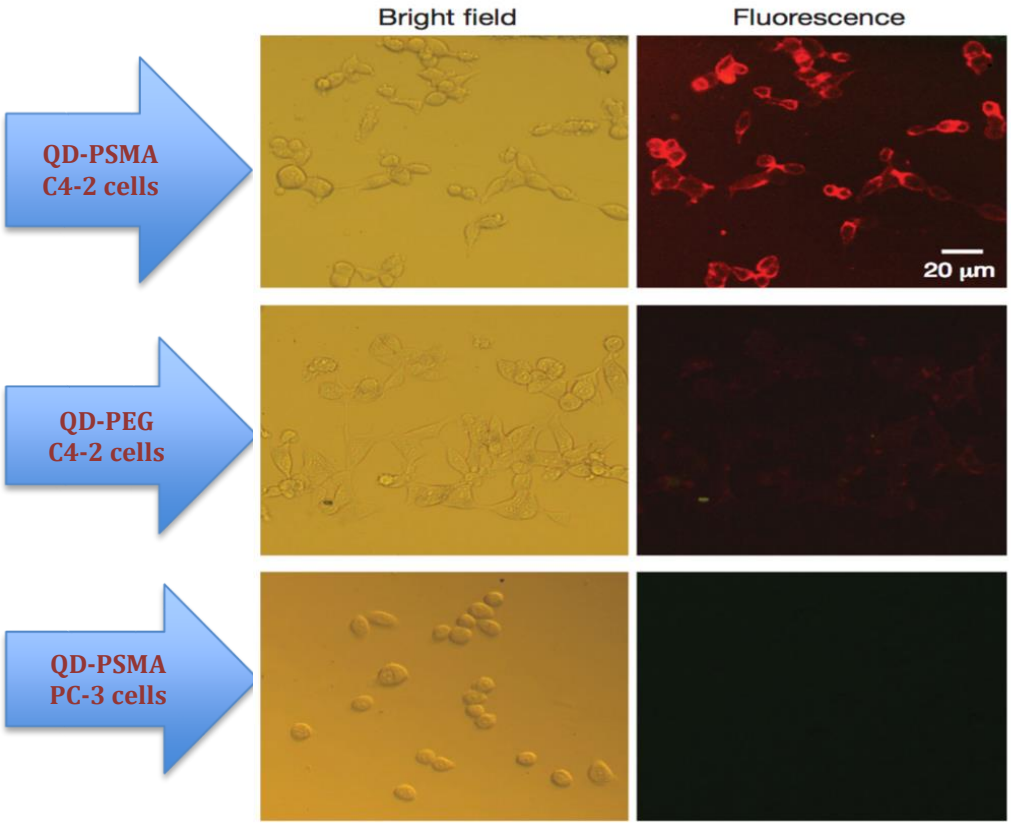

Figure 1-5. Qdot probe uptake in PSMA positive cells (C4-2) amd PSMA negative cells (PC-3). A negative control with no conjugation of antibody is also shown.[14]

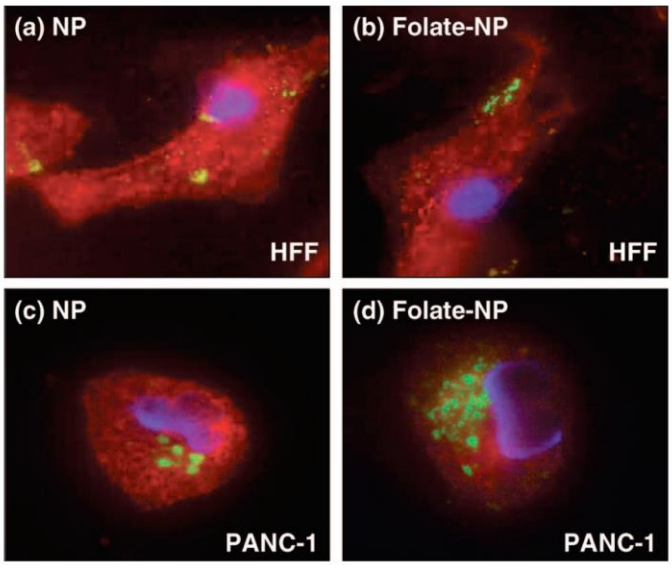

Figure 1-6. Silica nanoparticles uptake in Panc-1 cells which overexpress folate receptors and HFF cells that have no folate receptor overexpression. [15]

1.4 Drug delivery in photodynamic therapy

Water solubility of a compound is very important when applying it to the biological systems. Good water solubility can be obtained either by modifying the molecule or applying a drug delivery system. Addition of Polyethyleneglycol (PEG) moieties or acids groups in the structure of the compound can increase the solubility in the polar solvents such as water. For drug delivery silica nanoparticles, liposomes, micelles are widely used due to their biocompatibility and capability to functionalized with targeting structures.

Drug delivery systems based on polymeric particles (nanoparticles), micellar oil-dispersions, and liposomes have been studied and developed with varying degrees of success. Researchers found oil based micellar drug using polyoxyethylated castor oil (Tween-80, Cermophor-EL etc.) to enhance drug loading and tumor uptake, due to the interaction between this micellar oil and the lipoproteins plasma in blood. However, some emulsifying agents elicit acute hypersensibility reactions. Liposomal formations, can improve efficacy and safety of PS, but are generally unable to establish elevated tumor to normal tissue ratio due to their short plasma half-lives. However, there are some improvements to liposomal formulation reported such as drugs combined inside pH-sensitive polymeric micelles which show an improvement in tumor phototoxicity compared with Cremophor –EL in vitro, but in vivo studies represent poor tumor regression and increase the accumulation in normal tissue.[16, 17] All these techniques suffer from free circulation and accumulation in skin and eyes and the patient become highly sensitive to light.

1.4.1 Nanoparticles in photodynamic therapy

Birrench and Speiser are the first researcher that conceptualized nanoparticles[18], nanospheres and nanocapsules are an umbrella term with diameters less than 100 nm. Recently, Interest in nanoparticles as drug delivery system (either dissolved in the matrix or adsorbed on the surface of NPs) has increased due to the following: (a) nanoparticles can transport hydrophobic drugs in blood, (b) they have large surface area that can be functionalized with groups for additional chemical or biochemical properties, (c) nanoparticles have large volumes of distribution and are taken up efficiently by cells; (d) possibility of drug release; and (e) possibility of numerous synthetic strategies.[19, 20] Currently, there are several researches who are highlighted different approaches for utilizing nanoparticles for PDT. These approaches has been categorized into passive and active nanoparticles depending on either absence or presence of any targeting moieties on the surface or depending on their involvement in PS excitation.[21]

1.5 One photon and Two-photon Absorption Mechanism

Absorption of the photons causes excitation of the molecule to a higher energy electronic state from the ground state. In one photon excitation, usually the molecule can be excited by one photon that has similar energy with its energy gap between the highest occupied molecular orbital and lowest unoccupied molecular orbital. However, when a molecule exposed to high intensity of light undergoes near simultaneous absorption of two photons, the two photon combined energy can also access a stable excited state of the molecule and this process is called two-photons absorption (2PA).[22] The demands for a spatial and temporal overlap of two incident photons to undergo a 2PA generates precisely localized photoexcitation. For that reason, 2PA

has attracted significant attention for different kinds of applications such as photodynamic therapy,[23-25] bioimaging,[26-28] 3D data storage.[29-31]

1.6 One Photon and Two Photon Photodynamic Therapy

PDT compared with other methods has a number of advantages, such as minimally invasive, low toxicity, rapid effect, and low cost. Additionally, PDT treatment can be repeated without inducing resistance or hypersensitivity, which is considered a big problem associated with chemotherapy. However, PDT still undergoes some challenges that limit its broader application such as limited light penetration in tissue and the intense of incidence light can cause tissue damage. In addition, since this process is oxygen dependent, the efficiency would be difficult to increase in the hypoxic tumor system.[32-34]

The limitation of oxygen dependent efficiency can be solved by applying a new type of PDT: photoacid generator (PAG) based PDT. The mechanism of PAG in PDT paradigm is to induce cell death by causing an imbalance in the pH in the cell. This PAG can be excited with one photon absorption (1PA) or two-photon absorption (2PA) and generate strong acid **(Figure 1-7)**. It is hypothesized that this process can cause a fast drop in the pH of cell and induce cell apoptosis or necrosis.[25]

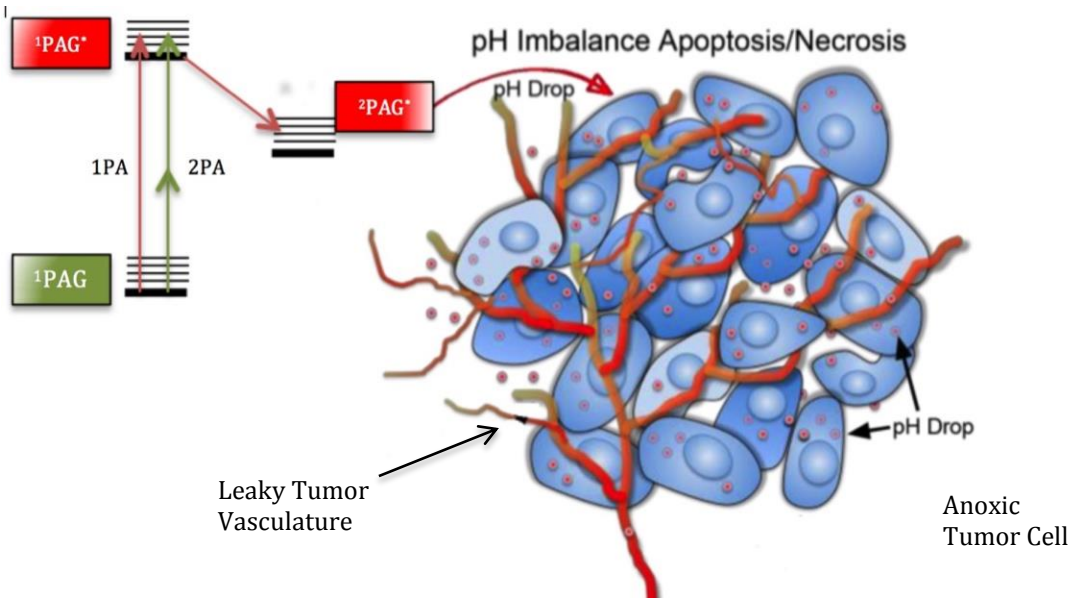

Figure 1-7. One photon and two-photon absorption photoacid generator (PAG) based on PDT. (25)

A 2PA photosensitizer, can be excited with longer wavelength NIR region. This provides deeper penetration and less damage by incident light. Furthermore, 2PA has a quadratic dependence on the intensity of light provided high spatial localization.[35-37] 1PA also has advantage over the 2PA such as the simplicity of that associated with generating photoacid. Furthermore, one photon photoacid generation is more affective process because the excitation source needed for this process is cheaper and easier to use. Another advantage of 1PA is that a large amount of targeted surface mass can be converted within tissue at a faster rate.

1.7 Efficiency of photodynamic therapy

Singlet oxygen quantum yield measurement represents the efficiency of a photosensitizer and shows the productivity of an excited photosensitizer to generate singlet oxygen. Some Photosensitizers undergo fluorescence after excitation, which could be useful in the adjustment of treatment fields.[38] Photosensitizers with a higher fluorescence quantum yield will have lower oxygen quantum yield. In this case, a balance is needed between fluorescence and singlet oxygen generation for an effective photosensitizer.

Furthermore, an effective photosensitizer should have low cytotoxicity in the dark or else healthy tissue will undergo cell death without PDT treatment. Another important consideration is water solubility of photosensitizer so that it can function in biological systems. For clinical treatment, a water-soluble agent can travel easily through the body.[39] Delivery systems also important and can be applied to carry the photosensitizer on the water.

1.8 Fluorene structure and properties

1.8.1 Structure Property Relation

Substitution pattern and different structures can classify compounds and lead to different photophysical properties. So, the desirable properties can be achieved by structural design.

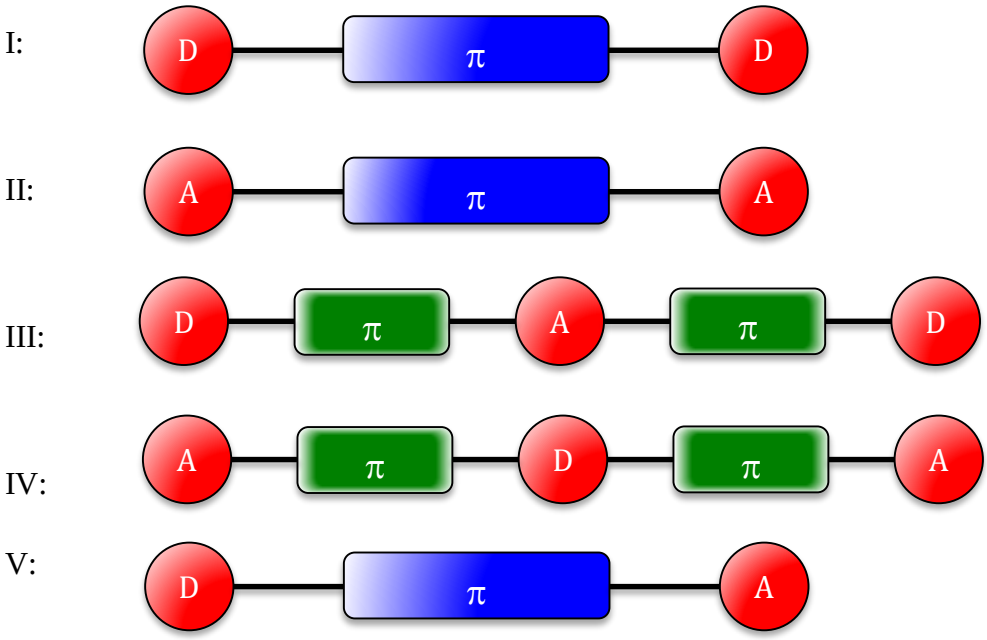

Figure 1-8. Schematic of various linear compounds classified based on the substitution pattern. (D= Donor group; π = π conjugated bridge; A = acceptor group). [(40)]

Usually, molecules with electron-rich groups located at the termini of the conjugated bridge (**Figure 1-8 I**) exhibit an increased 2PA cross section with possibility that 2PA band can also shift to a longer wavelength.[40, 41]

2PA cross section can also be larger when the electron withdrawing groups present in the center of the π conjugated bridge (**Figure 1-8 III**).[40] The extending of π conjugated bridge can cause to an increase in 2PA cross section and a red shift of the 2PA maximum.[41]

Substitution of electron rich and poor groups at the opposite termini of a π conjugated bridge (**Figure 1-8 V**) can cause a dipolar chromophore. Usually, dipolar chromophores have the lowest energy 2PA band at the wavelength two times that of one photon absorption band.[40] Increasing the length of conjugation can also cause increase in the 2PA cross section of dipolar

molecules.[42] The strength of substitution group can influence the 2PA cross section, a stronger electron donor group is expected to yield a higher cross section compared with a weaker substituent group.[42, 43] Larger 2PA cross section are occasionally achieved when a triple bonds are employed compared with double bonds.[44, 45]

1.8.2 Fluorene and Fluorene Derivatives

Fluorene cores has been mostly applied in both quadrupolar (**Figure 1-8 I-IV**) and dipolar (**Figure 1-8 V**) causing large 2PA cross sections. Its planarity and rigidity (**Figure 1-9**) induces large electron delocalization and serves as π conjugated bridge system.[22, 45]

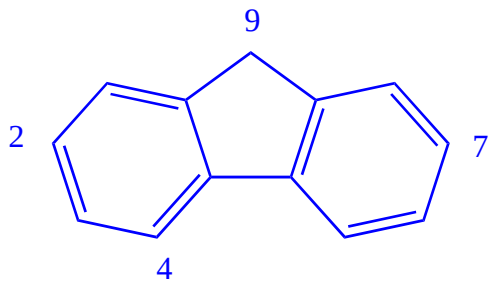

Figure 1-9. Structure of Fluorene core

The core structure of fluorene can be functionalized in positions 2, 4, 7 and/ or 9 (**Figure 1-9**). When the substitution occurs at positions 2, 4, and 7 the conjugation length increases resulting in high 2PA cross-section.[22] Electron withdrawing or electron donating groups can be substituted on these positions in order to obtain D-π-D, A-π-A or D-π-A structures.[27] Two fluorenes can also be used symmetrically in one structure, giving D-π-A-π-D or A-π-D-π-A structures.[26] Position 9 can also be functionalized to introduce alkyl chains or

hydrophilic groups, to achieve solubility in organic solvent or water. The substitution at position 9 will not affect the photophysical properties of the conjugation system.[22] Therefore; targeting groups can be introduced at position 9 for selective delivery in biological application.[42]

1.9 Phosphate in urine as an indicator of potential cancer diseases

Determination of inorganic phosphate (Pi) in human urine plays an important role in clinical diagnosis of various diseases. Phosphate levels in extracellular fluid accounts for about 1% of the total phosphate found in the human body, which is regulated by the parathyroid hormone.[46] Elevated levels of the parathyroid hormone are caused by hyperparathyroidism, which can be diagnosed by abnormally high concentrations of phosphate in urine.[46, 47] Both conditions are associated with different cancer diseases such as bone, breast [48] and parathyroid.[49] Furthermore, the concentration of phosphate is inversely related to the concentration of calcium in urine, which can be associated with other diseases.[46]

A plethora of analytical methods have been developed for the analysis of inorganic phosphate in human urine samples. These include photometric [50], spectrophotometric [51] and ion chromatographic [52] methods as well as fluorometric[53] assays. Their analytical features are summarized in Table 1-1.

Table 1-1. Analytical features of reported methodology for the analysis of phosphate in human urine samples

Detection limit (mmole L^{-1})	Sample volume	Sample preparation	Instrumental method	Interference	Analysis time	Ref.
NA	550 uL	No	Spectrophotometry	Other anions	2 min	50
0.02	10 mL	Centrifugation	UV-vis Absorption	Ketones, albumin	25 min	51
NA	1 mL	No	HPLC-UV-Detection	No	7 min	52
0.005	50 uL	No	Fluorescence assay	Glucose	2 h	53

Although numerous approaches have been developed for the analysis of inorganic phosphate in human urine samples, its determination at relevant biological concentrations via rapid, cost effective and accurate methodology still remains a challenge. The need for sample clean up and pre-concentration steps prior to quantitative analysis often leads to tedious and time-consuming assays. As a tentative means of circumventing the shortcomings of classical methodology, bio-sensing approaches coupled to amperometric[54] and fluorescence[55] detection have been reported in the literature. Table1-2 provides a comparison of the two previously reported sensors.

Table 1-2. Analytical features of sensing approaches for the analysis of phosphate ions in human urine samples

Detection limit (mmole L^{-1})	Sample volume	Sample preparation	Sensor type	Interference	Analysis time	Ref.
0.004	50 uL	No	CoPC-SPCE[1]	Yes	5 min	54
NA	10 uL	Ultracentrifugation	Fluorescence	No	NA	55

CHAPTER 2. DESIGN AND DEVELOPMENT OF NEW PHOTODYNAMIC CANCER THERAPY AGENT SELECTIVELY INDUCES DEATH OF CANCER CELL

This chapter focuses on the design and development of new photodynamic therapy agent photoacid generator (PAG) capable of inducing cell death of cancer cells making this agent an ideal and formal therapeutic drug that can be used in vivo. This therapeutic agent generates acids (H^+ molecules) when excited with light at certain wavelengths; this causes a drop in pH within the cytosol of the cancer cells, which then undergo necrosis. Since Silica nanoparticles (SiNPs) have unique characteristic properties such as biocompatibility and capacity for functionalization with groups for additional chemical or biochemical properties. They are promising tools for biochemical investigation, providing solid media for drug delivery systems and high uptake efficiency by cells. In addition, they are used as safe and biocompatible pharmaceutical additives. Herein, we synthesized silica nanoparticles of ultra-small size (9 nm) covalently bonded with the synthesized photoacid generator (**SiN-NH-PAG**) to enhance the solubility and carry this hydrophobic agent in water as well as decrease the cytotoxicity. SiNPs provide a high loading of functional groups (PAG) without dramatically affecting the structure while exploiting SiNPs properties. On the other hand, we attached PAG with poly ethylene glycol (**PAG-PEG**) to make it water-soluble in order to compare the results between these water-soluble moieties in future studies. PAG was designed with high photoacid quantum yield and high one-photon (1PA) and two-photon absorption (2PA) to enhance the penetration into optically thick tissue with low fluorescence quantum yield.

2.1 Introduction

Over the last 25 years, silica nanoparticles (SiNPs) and other nanomaterial, have attracted tremendous interest from the scientific researchers due to their unique properties that differ from those of their bulk counterparts such as large surface area, large pore volume, narrow distribution, and excellent chemical and thermal stability making these nanoparticles potentially suitable for various biomedical applications.[56] SiNPs opens a new rout of applications in optoelectronics and biological studies purposes.[57] In controlled release applications, SiNPs has shown high ability to store and release the therapeutic agents such as antibiotics.[44] For drug delivery system, SiNPs should be very selective, nontoxic, and show a good clearance rates. Cornell dots (Cdots) are one of the SiNPs platform that meet all these criteria and has been approved by FDA for human clinical trials suggesting SiNPs are a promising delivery system for live animals.[58]

Synthesis of SiNPs has been done using variety of methods, Stober et al [59] in 1968, reported a pioneering method for the synthesis of monodisperse SiNPs form aqueous alcohol solutions of silicon alkoxides using ammonia as a catalyst and different sizes were prepared ranging from 1 um to 50 nm with narrow size distribution. The size of particles depends on the type of silicon alkoxide and alcohol. In methanol solutions, prepared particles are the smallest. As the chain length of alcohol increases the particles size increases. The distribution of particles sizes become broader, when longer chain of alcohol are used as a solvent. After that, many studies were conducted in this area to prepare silica nanoparticles.

For biomedical applications, silica nanoparticles should be water soluble and hydrophilic to prevent aggregation and precipitation in a biological environment. Photoacid generator

(PAGs) are light sensitive compounds that generate acid when exposed to light at certain wavelength, most photoacid generator absorb light in UV or Deep UV region and have several applications such as coatings, paints, anticorrosives, photoresists, and microelectronics, and 2D/ 3D lithographic patterning.[60] Recently, our group successfully used PAG as new photodynamic therapy agent inducing cell death of cancer cells (HCT-116).[25]

There were a lot of attempts to prepare triarylsulfonium salt in high yields. Although the literature contains a number of synthetic procedures for the preparation of these compounds, these procedures were deemed unsatisfactory for them due to their poor yields, high degree of complexity, long reaction times, or general lack of applicability to a variety of substituted symmetrical and unsymmetrical triarylsulfonium salts.[61-63] Nesmeyanov and his co-workers [64] reported that arylation of diphenyl sulfide could occur by using diphenyliodoniumfluoroborate at 220-230 ^{o}C to yield triphenylsulfonium fluoroborate. When they used five times molar excess of diphenyl sulfide, they got around 60% yield of the sulfonium salt.

$$(C_6H_5)_2S + (C_6H_5)_2I^+BF_4^- \longrightarrow (C_6H_5)_3S^+BF_4^- + C_6H_5I$$

Knapcyzk and McEwen obtained a slightly better yield 64% when they repeat the reaction for 35 h using 180 ^{o}C Temperature.[65]

James V. Crivello and Julia H. **W.**Lam [66] developed a new method for preparation of pure triarylsulfonium salts in high yield (97%). They observed that diaryliodonium salts have BF_4^-, AsF_6^-, and PF_6 counterions which can undergo thermolytic decomposition at low temperature 120 – 130 °C in the presence of catalytic amounts of a copper (II). In the absence of

a copper (II) catalyst, these compounds can undergo decomposition near to their melting points in the range 220-250 °C. Prior to that work, Beringer and his co-workers [67] reported that copper (I) and (II) compounds catalyze the decomposition of diaryliodonium halides in solution. In water or methanol, the major products were the aryl halides and the aryl iodide.

$$Ar_2I^+Cl^- \longrightarrow ArI + ArCl$$

It was reported that the reaction undergoes concerted collapse of a complex formed between the diaryliodonium ion and a di or trichlorocurate (I) ion. The same result were reported with Glusker, and Roberts[68] that the diaryliodonium tosylates and trifluoroacetates hydrolysis to aryl halides and phenols is strongly catalyzed by traces of copper (I) and (II) which catalytic activity was assigned to its ability work as an electron transfer agent.

Based on the above information and since the arylation of diphenyl sulfate using copper (II) as a catalyst consumed long time to complete (conventional thermal conditions), our group reported synthesis and characterization of novel sulfonium photoacid generators using micro – assisted synthesis.[60] This method afforded reaction times 90 to 420 times faster, resulting in higher yield than conventional thermal conditions **Table 2-1**.

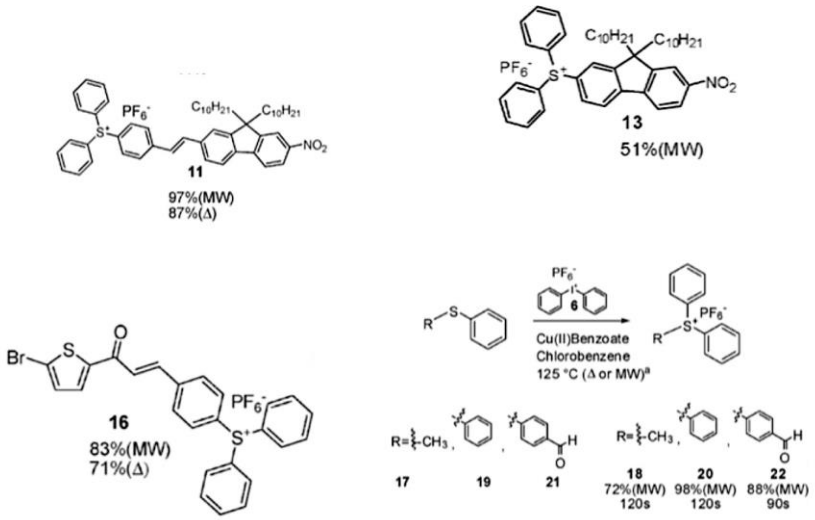

Table 2-1. Microwave assisted Vs. Conventional thermal reaction time for Sulfonium salt PAG formation.[60]

Product	MW Time (yield)	Δ Time (yield)
11	8 min (97%)	8 h (87%)
13	10 min (51%)	70 h (10%)
16	14 min (83%)	24 h (71%)
18	120 s (72%)	3 h (100%)
20	120 s (98%)	3 h (97%)
22	90 s (88%)	3 h (83%)

2.2 Materials and Methods

Compound (**11**) **scheme 2-3** was synthesized as previously reported.[69] Compound (**7**) **scheme 2-1** was synthesized as previously reported.[60] All other chemicals and reagents were purchased from Aldrich or Acros Organics, and used as received unless otherwise noted. ^{1}H and ^{13}C NMR spectroscopic measurements were performed using Varian 400 or 500 NMR spectrometers at 400 or 400 MHz for 1H (referenced to TMS at δ) (0.0 ppm) and 125 or 75 MHz for ^{13}C (referenced to $CDCl_3$ at δ) 77.0 ppm). All glassware was flamed dried and cooled in a desicator over calcium chloride. Most of the reactions were carried out under N_2 atmosphere. All sulfonium salt reactions and purifications were carried out under red light, or in the dark.

2.2.1 Synthesis

Synthesis of Compound 1. Fluorine (6 g, 36.09 mmol) was dissolved in dry THF (150 mL) under nitrogen gas and treated with n-BuLi (1.6 M in hexanes, 22.5 mL) at -78 ˚C drop by drop over 30 min. After the addition complete, the temperature was raised to room temperature and the mixture was stirred for 1 h. The mixture was cooled to -78 ˚C and a solution of ethylbromide (2.6 mL) was added. The temperature was allowed to rise to room temperature and mixture was left stirring for 24 h. The THF was evaporated from the orange solution in vacuum and then extracted with CH_2Cl_2 yielding a yellow oil and purified by column chromatography using hexane to give 6.4 g (91% yield). ^{1}H NMR (400 MHz, $CDCl_3$) δ 7.90 (d, 2H), 7.65 (d, 2H), 7.53 – 7.40 (m, 4H), 4.08 (t, 2H), 3.18 (d, J = 747.2 Hz, 1H), 0.89 (t, 3H).^{13}C NMR (101 MHz, $CDCl_3$) δ 147.31, 141.44, 126.98, 126.90, 124.41, 119.98, 119.87, 119.86, 77.48, 77.16, 76.85, 48.59, 25.83, 9.87.

Synthesis of compound 2. (6 g, 30 mmole) of compound **1** was dissolved in (28 mL) of dry *p*-dioxane at 50 ˚C temperature and degassed under vacuum and nitrogen. After that 40% aqueous solution of Triton B (0.25 mL) was added, the mixture color was changed from light yellow to brown. This solution was then treated with acrylonitrile for 15 min. And the temperature was maintained around 50 ˚C. The resulting brown solution was stirred for 16 h. after which it was neutralized with 10% HCl (aq) and extracted with CH_2Cl_2. The crude product was purified by column chromatography using 5:1 hexane/ethyl acetate to afford white solid (5.9 g mmole (77% yield) mp = 99.2-100 ˚C. ^{1}H NMR (400 MHz, $CDCl_3$) δ 7.70 (d, *J* = 1.1 Hz, 2H), 7.34 (dd, *J* = 3.6, 1.1 Hz, 6H), 2.41 (m, 2H), 2.03 (t, 2H), 1.49 (t, *J* = 4.0 Hz, 2H), 0.31 (t, 3H). ^{13}C NMR (101 MHz, $CDCl_3$) δ 147.26, 141.43, 127.92, 127.81, 127.64, 122.83, 120.22, 119.88, 77.48, 77.16, 76.84, 54.87, 35.65, 32.85, 12.27, 8.30.

Synthesis of Compound 3. (4 g, 17.1 mmole) of compound **2** was dissolved in ethylene glycol (150 mL). (4 M, 50 mL) of KOH was added and heated to reflux for 16 h. After that, ethylene glycol was removed by vacuum distillation to afford yellow oil which was neutralized with 10% HCl (aq) and CH_2Cl_2 was used for extraction. The crude product purified by column chromatography hexane/ethyl acetate (3:1) to produce (3.65 g) (85 % yield) mp = 134.8-135 ˚C. ^{1}H NMR (400 MHz, $CDCl_3$) δ 7.72 (d, *J* = 6.7 Hz, 2H), 7.44 – 7.17 (m, 6H), 2.56 – 2.24 (m, 2H), 2.06 (q, *J* = 7.3 Hz, 2H), 1.68 – 1.49 (m, 2H), 0.34 (t, *J* = 7.3 Hz, 3H). ^{13}C NMR (101 MHz, $CDCl_3$) δ 179.81, 148.45, 141.35, 127.35, 127.35, 127.30, 122.82, 122.82, 119.87, 77.33, 77.02, 76.70, 54.65, 34.25, 32.96, 28.92, 8.31.

Synthesis of Compound 4. (3 g, 11.9 mmole) of compound **3** was dissolved in glacial acetic acid (25 mL). The resulting solution was heated to 55 ˚C and (2 mL) of 70% Nitric acid was

added drop wise. After the addition was complete, the mixture was stirred for 3 h and monitored by TLC. The reaction was stopped by adding 10 mL water and extracted with CH_2Cl_2. The afforded yellow oil was purified by column chromatography 3:1 hexane/ethyl acetate to give yellow solid (2.8 g,) (79% yield). mp = 134.8-136 °C. ^{1}H NMR (400 MHz, $CDCl_3$) δ 8.50 – 8.17 (m, 2H), 7.92 – 7.76 (m, 2H), 7.59 – 7.40 (m, 3H), 2.64 – 2.33 (m, 2H), 2.26 – 2.03 (m, 2H), 1.79 – 1.45 (m, 2H), 0.34 (t, *J* = 7.4 Hz, 3H). ^{13}C NMR (101 MHz, $CDCl_3$) δ 179.39, 150.13, 149.79, 147.82, 147.25, 139.00, 129.63, 128.03, 123.81, 123.29, 121.46, 120.07, 118.50, 77.39, 77.07, 76.75, 55.35, 33.87, 32.72, 28.90, 8.25.

Synthesis of Compound 5. (2 g, 6.7 mmole) of compound **4** was dissolved in (30 mL) glacial acetic acid and placed into three neck flask fitted with condenser, nitrogen gas and thermometer. The mixture was degassed with nitrogen for 15 min. then I_2 (850 mg, 3.3 mmole) was added and the resulting orange solution was stirred for 30 min. After that, (924 mg, 13.4 mmole) of $NaNO_2$ followed by concentrated H_2SO_4 (1.5 mL) was added and the reaction heated to 125 C° and monitored by TLC for 3 h. After the reaction had completed, the reaction was cooled down and extracted with ethyl acetate and the resulting yellow oil was purified by column chromatography using 3:1 hexane/ ethyl acetate to give a yellow solid (2.52 g) (90% yield), mp = 181-182 °C. ^{1}H NMR (400 MHz, $CDCl_3$) δ 8.28 (d, *J* = 8.4, 2.1 Hz, 1H), 8.20 (s, *J* = 3.2 Hz, 1H), 7.86 – 7.73 (m, 3H), 7.54 (d, *J* = 8.6 Hz, 1H), 2.60 – 2.33 (m, 2H), 2.24 – 1.97 (m, 2H), 1.74 – 1.47 (m, 2H), 0.33 (t, *J* = 7.3 Hz, 3H). ^{13}C NMR (101 MHz, $CDCl_3$) δ 179.58, 152.56, 149.59, 147.98, 147.08, 138.95, 137.59, 133.01, 124.29, 123.26, 120.65, 118.89, 96.15, 77.73, 77.41, 77.09, 55.93, 34.06, 32.98, 29.27, 8.60.

Synthesis of Compound 8. In 2 mL of dry DMF (500 mg, 1.18 mmole) of compound **5** and (200 mg, 0.94 mmole) of compound **7** (phenyl (4-vinylphenyl) sulfane) were dissolved with 0.01g, (10% molar) of Palladium acetate, and (1.7 mL) of triethylamine. The resulting brown solution was purged with nitrogen for 10 min. while stirred. The microwave was adjusted to closed vessel standard mode; maximum temperature 160 $^{\circ}$C; maximum pressure 250 psi; maximum power 60 W, and high speed stirring. The run time (a time at which the reaction approaches maximum temperature or pressure) was adjusted for 2 min. and the hold time 30 min. the reaction was monitored by TLC. After starting material was gone, the mixture cooled down and celite plug was used to filter it. The filtrate was extracted with CH_2Cl_2 and washed with water 4x, dried with anhydrous magnesium sulfate and concentrated to afford brown oil which was purified by column chromatography using hexane/ethyl acetate (2:1) to give a yellow crystal (485mg) (99%). Mp = 81-82 $^{\circ}$C. ^{1}H NMR (400 MHz, $CDCl_3$) δ 8.29 (d, *J* = 8.4, 2.1 Hz, 1H), 8.22 (s, *J* = 1.8 Hz, 1H), 7.79 (q, *J* = 8.1, 6.1 Hz, 2H), 7.42 (m, *J* = 14.4, 13.5, 9.2, 7.6, 3.5 Hz, 11H), 7.18 (s, 2H), 2.46 (m, *J* = 8.2 Hz, 2H), 2.24 – 2.10 (m, 2H), 1.62 (t, *J* = 13.2 Hz, 2H), 0.37 (t, *J* = 7.3 Hz, 3H). ^{13}C NMR (101 MHz, $CDCl_3$) δ 178.16, 150.76, 149.98, 147.45, 147.12, 138.77, 138.59, 135.95, 135.68, 135.19, 131.49, 131.45, 130.80, 129.31, 129.06, 128.50, 127.38, 127.30, 126.78, 123.94, 121.73, 120.96, 119.97, 118.46, 77.33, 77.22, 77.01, 76.70, 55.33, 33.93, 32.82, 28.73, 8.30.

Synthesis of Compound PAG9. (370 mg, 0.7101 mmole) of compound **8** was dissolved in (2 mL) of chlorobenzene in a (2 mL) glass reaction vessel, 302.8 mg, (0.711 mmole) of diphenyliodonium hexafluoro phosphate and 0.005 g (5% molar) of copper (II) benzoate were

mixed in the dark while purged with nitrogen for 10 min. while the microwave was adjusted to closed vessel standard mode; maximum temperature 125 °C, maximum pressure 40 psi; maximum power 100 W, high seeped stirring. The run time (the time at which the reaction approaches max temperature or pressure) was set for 1 min. and the hold time 15 min. TLC was used to monitor the reaction every 2 min. upon the completion the solvent was evaporated to produce a brown crude product. The resulting crude was purified by column chromatography using DCM/Methanol 9:1 to afford a yellow solid crystal (470 mg) (87%) mp = 63-64 °C. ^{1}H NMR (400 MHz, DMSO) δ 8.28 (s, *J* = 2.9 Hz, 1H), 8.25 (d, *J* = 2.0 Hz, 1H), 8.15 – 7.97 (m, 4H), 7.93 – 7.75 (m, 14H), 7.66 (d, *J* = 16.3 Hz, 1H), 7.57 (d, *J* = 16.4 Hz, 1H), 2.19 (m, *J* = 30.8, 14.6, 7.7 Hz, 4H), 1.49 – 1.08 (m, 2H), 0.23 (t, *J* = 7.3 Hz, 3H).^{13}C NMR (101 MHz, DMSO) δ 175.81, 152.84, 152.07, 147.67, 143.97, 139.85, 138.24, 135.08, 134.23, 132.65, 132.15, 131.98, 129.64, 128.02, 127.73, 126.26, 124.24, 123.31, 122.85, 122.30, 121.48, 119.12, 116.14, 56.32, 36.17, 32.17, 9.11.

Synthesis of Compound PAG-PEG. Benzotriazole (64 mg, 0.005 mmole) was dissolved in (10 mL) dry DCM in 25 mL round bottom flask while it was purged with nitrogen and stirred at room temperature until the solution became clear. After that 0.1 mL of thionyl chloride was added. After the addition had completed, the solution was treated with (100 mg, 0.13 mmole,) of compound **PAG 9** and the reaction was stirred for another 2 h. Then, 1 equivalent mmole of polyethylenglycole (PEG) was added and stirred for 3 h. the DCM was evaporated to give crude dark yellow oil. The afford crude was purified by column chromatography 5:1 DCM/ Methanol to produce brown oil (165 mg), (70% yield). ^{1}H NMR (400 MHz, MeOD) δ 8.29 – 8.13 (m, 2H), 7.91 (dd, *J* = 18.5, 9.2 Hz, 4H), 7.80 – 7.61 (m, 14H), 7.51 (d, *J* = 10.1 Hz, 1H), 7.27 (d, *J* = 4.4

Hz, 1H), 3.76 – 3.15 (m, 96H), 2.51 – 2.33 (m, 2H), 2.20 – 2.00 (m, 2H), 1.39 (dd, *J* = 17.1, 9.1 Hz, 2H), 0.22 (t, *J* = 6.0 Hz, 3H).^{13}C NMR (101 MHz, MeOD) δ 174.10, 151.58, 151.00, 147.80, 147.64, 144.50, 140.17, 138.15, 134.77, 134.02, 131.88, 131.71, 131.15, 129.33, 127.71, 126.96, 125.54, 123.77, 122.38, 122.10, 121.95, 120.56, 118.72, 71.89, 70.46, 70.41, 70.34, 70.27, 70.07, 69.24, 58.03, 55.97, 48.64, 48.57, 48.43, 48.36, 48.22, 48.15, 48.00, 47.93, 47.72, 47.51, 47.29, 39.20, 34.76, 32.69, 30.71, 7.58.

Synthesis of Compound PAG-NH-Boc. Synthesis of PAG-NH-Boc compound was performed using the same procedure for compound (**PAG-PEG**). ^{1}H NMR (400 MHz, MeOD) δ 8.38, 8.32, 8.30, 8.26, 8.14, 8.12, 8.12, 8.10, 8.09, 8.07, 8.06, 8.05, 8.04, 8.03, 7.89, 7.88, 7.86, 7.84, 7.83, 7.81, 7.77, 7.75, 7.70, 7.66, 7.61, 7.57, 7.47, 6.87, 6.75, 6.72, 3.38, 2.81, 2.52, 2.51, 2.26, 2.17, 2.14, 1.34, 1.20, 1.07, 0.24, 0.23, 0.22. ^{13}C NMR (101 MHz, MeOD) δ 172.63, 157.11, 153.11, 152.31, 148.59, 144.71, 140.70, 139.17, 135.91, 134.98, 133.48, 132.96, 132.77, 130.85, 130.44, 128.63, 127.04, 125.22, 124.19, 123.19, 122.42, 120.17, 116.89, 78.89, 57.01, 56.50, 35.78, 33.23, 31.65, 29.83, 28.51, 27.91, 9.83.

Synthesis of Amine-Terminated Silica Nanoparticles (SiNPs). Synthesis of (**SiNPs**) was performed following the method described by P.N. Prasad et al. with some modifications.[70] The synthesized silica nanoparticles and their bioconjugates with **PAG 9** were schematically described by **Scheme 2-2**. Briefly, the nanoparticles were synthesized by adding polymeric organically modified silica solution into the Tween-80/ 1-butanol micelle solution dissolved in deionized water. First, 0.5 g of Triethoxyvinylsilane (VTES, 97%) was dissolved in 5 mL of N-methyl-2-pyrrolidone **(**NMP) and condensed in the presence of 200 μL of ammonium hydroxide

(28–30%) at room temperature with 16 h stirring in order to get a clear solution of prepolymerized silica solution. After that, the prepolymerized silica solution was filtered using a membrane filter (0.2 μm pore size). Micelles were prepared by mixing 0.1 g of Tween-80 and 0.2 mL of 1-butanol in 5 mL of deionized water.

100 μL of silica solution was mixed with 0.2 mL of NMP and then added to the prepared micelle dispersions drop by drop to induce nanoprecipitation under vigorous stirring. After 10 min, 20 μL of (3-aminopropyl)triethoxysilane (APTES) was added in order to functionalize the surface of SiNPs. The mixture was stirred for further 24 h in order to be sure the sol-gel condensation within the coprercipitation nanoparticles was complete. Purification of nanoparticles was performed by dialyzing the dispersion against deionized water in a 10 KDa cutoff cellulose membrane to remove Tween-80 and 1-butanol for 48 h. The solution was then filtered with a 0.2 μm cutoff membrane filter.

2.2.2 Conjugation of amine-terminated silica nanoparticles with PAG 9

A 0.2 mL of 0.1 M EDC solution was added to a 5 mL of stock solution of amine-terminated silica nanoparticles. After the mixture was stirred for 25 min, an excess of **PAG 9** (3.5mg) was added. The reaction between amine groups with PAG was allowed to proceed for 3 h. After that, the reaction mixture was dialyzed against deionized water in the dark for 48 h in order to remove unreacted molecules. Finally, the sample was filtered with a 0.2 μM cutoff membrane filter and stored at 5 ^{0}C for later use.

2.3 Particle Size

Particle size data was obtained with a Zetasizer Nano ZS90, using Silica nanoparticles capped with amino group solution and Silica nanoparticles covalently bonded with PAG solution. Both of solutions were filtered with 0.2 μm polyethersulfone membrane filters with polypropylene housing.

2.4 Photophysical Characterizations

2.4.1 Absorption spectra

Absorption spectra were recorded by using Agilent 8453UV-vis spectrophotometer. Steady state fluorescence spectra were measured by EDINBURGH INSTRUMENTS FLS980 spectrofluorimeter.

2.4.2 Fluorescence Quantum Yield Measurement

Relative to Rhodamin 6G (Rh6G) in ethanol as a standard, fluorescence quantum yield was determined. The measurement was made in the photon-counting regime of a PMT by using an L-format configuration using EDINBURGH INSTRUMENTS FLS980 spectrofluormiter. The measurement was performed at room temperature in 1 cm quartz cuvettes with concentration 1 $\times 10^{-6}$ M. Using the following equation

$$\phi = \phi_{ref}\left(\frac{OD_{ref}}{OD}\right)\left(\frac{\int I}{\int I_{ref}}\right)\left(\frac{n^2}{n_{ref}^2}\right)$$

where Φ is the fluorescence quantum yield, OD is the optical density at the excitation wavelength, I is the integrated fluorescence intensity, and n is the refractive index of the solvent.

2.4.3 Two-Photon (2PA) Cross Section Measurement

The investigations of the 2PA were performed with a femtosecond laser system (Coherent, Inc.). The output of a Ti:Sapphire laser (Mira 900-F, tuned to 800 nm, with a repetition rate = 76 MHz, average power ~1.1 W, and pulse duration ~200 fs), pumped by the second harmonic of cw Nd^{3+}:YAG laser (Verdi-10), was regeneratively amplified with a 1 kHz repetition rate (Legend Elite USP) providing ~100 fs pulses (FWHM) with energy ~3.6 mJ/pulse. This output at 800 nm was split into two separate beams with average power ~1.8 W each and pumped into two ultrafast optical parametric amplifiers (OPerA Solo (OPA), Coherent Inc.) with a tuning range 0.24−20 μm, ~100 fs (FWHM), and pulse energies up to ~100 μJ. A single laser beam from the first OPA was used for direct 2PA cross-section measurements by the open-aperture Z-scan method.[71]

2.4.4 Photoacid Quantum yield Measurement

Photoacid quantum yield was measured by selectively exciting the PAG solution at the suitable wavelength using LOCTITE. The power of the incident light was measured by using Ophir Power Star power meter, which was equipped with a UV 1.44 cm^2 detector head. To calculate the quantum yield Rhodamine B base was used as a sensor for the photoacid generator, and observed the change on the optical density of sulfonium salt with not exceed 5%. The quantum yield for photoacid generator was calculated by using the following equation:

$$\emptyset H = \frac{\Delta OD_{555} \,.\, N_A}{10^3 \,.\, \varepsilon_{555}^{RhB} \,.\, I_o \,.\, \left[1 - 10^{-\bar{D}}\right] . \Delta t}$$

Where ΔOD^{555} is the change in the optical density during the generation of Rhodamine B measured at 555nm, N_A is the Avogadro number, ε_{555}^{RhB} is the extinction coefficient of rhodamine B at 555 nm, $\overline{D}$ is the average absorption intensity, I_o is the Intensity of irradiation (photon/cm^2.sec), and Δt is the time of irradiation in sec.

2.5 Results and Discussion

2.5.1 Synthesis

The synthesis of triarylsulfonium salts was originally developed by Crivello and Lam. They used a new method for the preparation of pure triarylsulfonium salts with high yield and less time consumption by using a copper (II) benzoate as a catalyst for the reaction.[62] Although there are a lot of synthetic procedures for the preparation of these compounds, these methods were unsatisfactory due to their low yields, reaction taking long time, and complexity. Recently, a microwave-assisted synthetic route has been reported, which is more efficient in preparing triarylsulfonium salts.[60]

Most of commercially (PAGs) available needed ultraviolet (UV) light to achieve his job and this is considerate a major problem since the UV light is a sort of non-selective excitation that maybe caused undesirable side reaction, and offers poor penetration. In order to make PAG more efficient, we designed and synthesized a new PAG that absorbs light at a long wavelength (VIS region), which on utilizing 1PA and 2PA the molecule demonstrates enhance penetration. The synthesis of photoacid generators PAG-PEG, and SiN-NH-PAG are illustrated in **scheme2-1, scheme2-2, and scheme 2-3**. The synthesis **scheme 2-1** started with asymmetric alkylation at

position 9 of fluorene with ethyl and acrylonitrile groups to get intermediate compound **2**. Next, intermediate compound **3** was synthesized by hydrolysis of intermediate compound **2** in basic conditions using aqueous solution of sodium hydroxide in the presence of ethylene glycol and refluxed for 24 hours to get a carboxylic group for further conjugation. Intermediate compound **4** was synthesized by introducing a nitro group at position 2 of fluorene using HNO_3 (70%) acetic acid as a solvent. An iodo group was also introduced at position 7 of fluorene to produce intermediate compound **5**. On the other branch of synthesis, we synthesized intermediate compound **6** starting from p-nitrobenzaldyhade with thiophenol using caesium carbonate reagent in DMSO. Intermediate compound **7** was synthesized according to literature with some modification. Intermediate compound **8** was obtained quantitatively via a microwave-assisted palladium acetate-catalyzed Heck reaction, coupling vinyl sulfide **7** with precursor **5** and the yield for this reaction was 99%. Next, PAG compound **9** was synthesized by pyrolysis of diphenyliodonium counterpart in the presence of diphenylsulfide (intermediate compound **8**) using microwave-assisted synthesis to give 89% yield. Then, intermediate compound **PAG9** was coupled with polyethyelenegycol (PAG-PEG) **Scheme 2-1,** and silica nanoparticles (SiN-NH-PAG) **Scheme 2-2,** for different water-soluble derivatives. PAG was also conjugated with *Tert*-butyl (4-aminobutyl)carbamate to produce PAG-NH-Boc for future study as shown in **scheme 2-3.**

The synthesis and surface modification of silica nanoparticles are schematically described in **Scheme 2-2.** A prepolymerized triethoxyvinylsilane (VTES) sol solution was first prepared. After that, the sol solution was mixed and corecipitated within the nonpolar aqueous Tween-80 micelles by a solvent displacement process. (APTES) was added to the reaction mixture in order

to introduce free amine groups on the silica nanoparticles surface for subsequent bio-conjugation.

Conjugation of amine –terminated silica nanoparticles with PAG 9 was done using EDC coupling reagent and an excess of PAG 9 was added to be sure there is no free amine in the surface of silica nanoparticles.

The PAG was designed to exhibit high 1PA, 2PA cross-section and photoacid quantum yield. Fluorene was selected as a core structure due to high thermal and photochemical stability and the capability of substitution on the position 2-, 7-, and 9. Stilbenyl motifs were introduced in order to extend the π-conjugation and two acceptor groups (nitro and triarylsulfonium) were attached to get net structure of A-π-π-A . Nitro group was introduced in the structure in order to enhance the photoacid quantum yield by increasing the chance of spin orbit coupling to make intersystem crossing and reducing the radiative decay pathway. As a result decrease the fluorescence quantum yield. In case of PAG with high fluorescence quantum yield, the molecule will undergo radiative decay (fluorescence) before forming photoacid.[25]

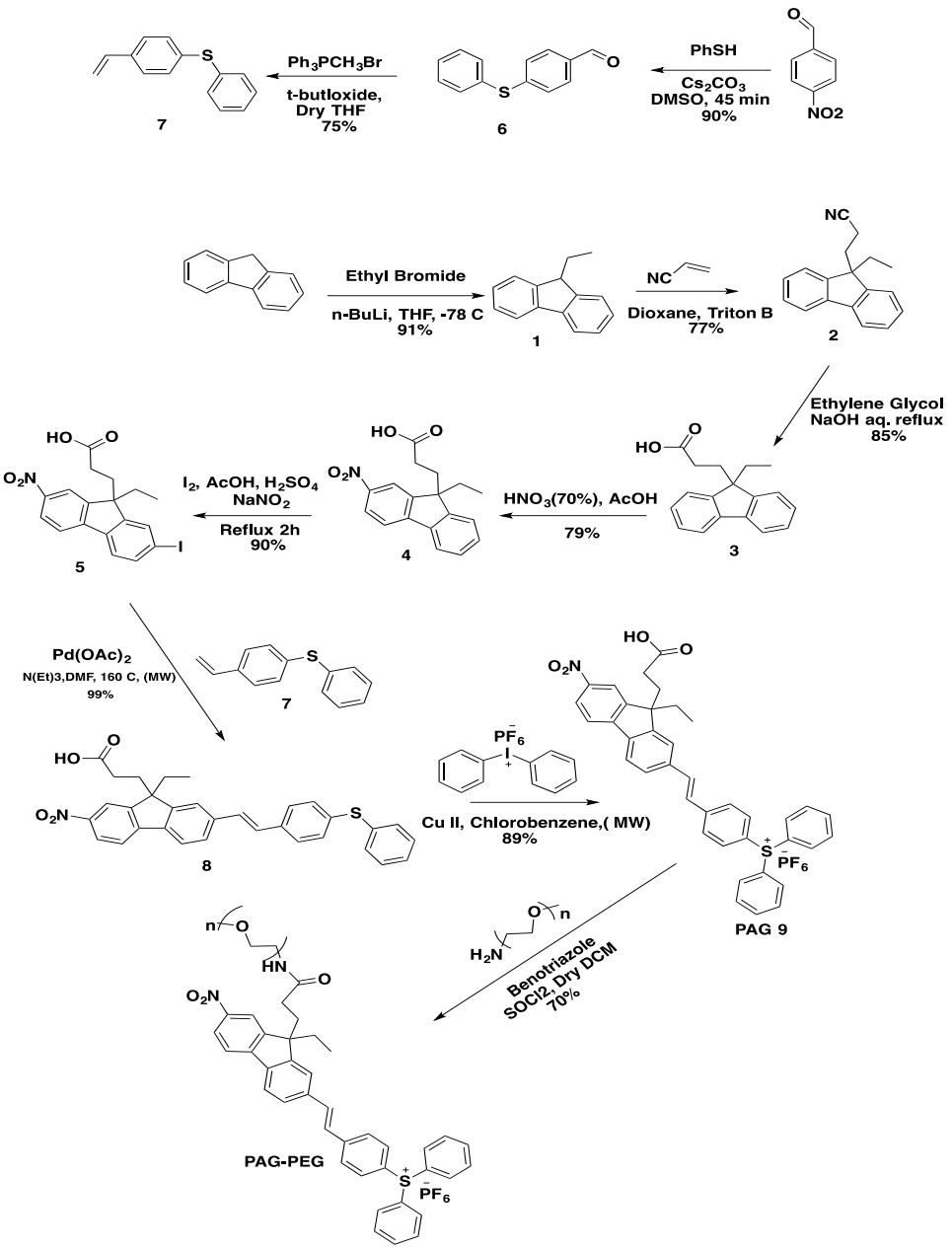

Scheme 2-1. Synthesis of water-soluble photoacid generator bonded with polyetheylengylcol (PAG-PEG).

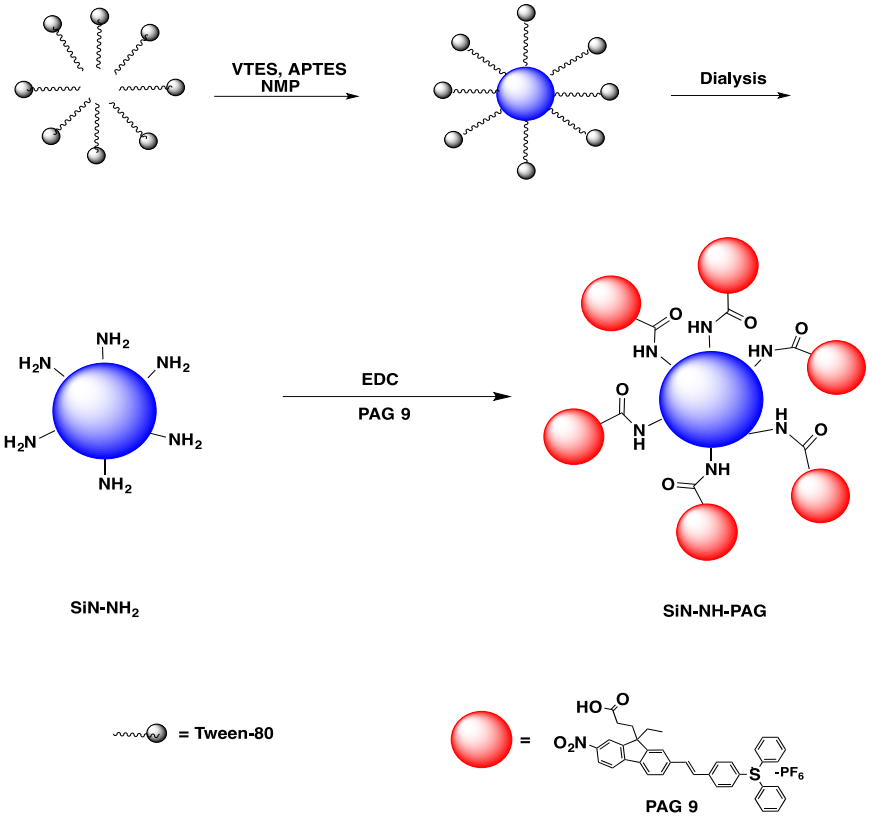

Scheme 2-2. Silica nanoparticles conjugated with photoacid generator (SiN-NH-PAG).

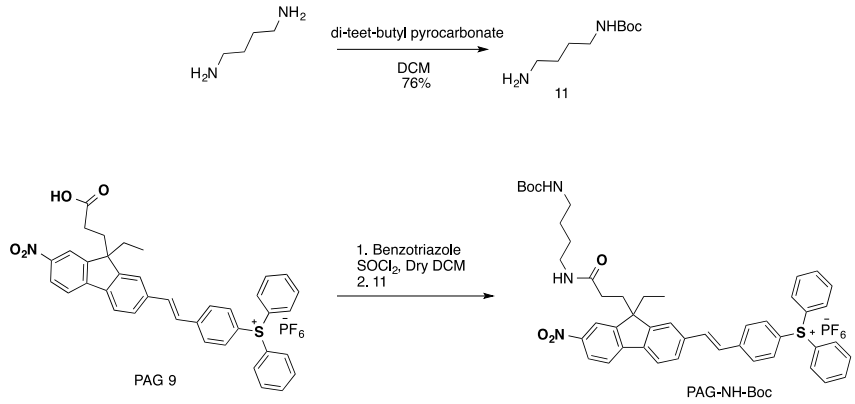

Scheme 2-3. Design and synthesis PAG-NH-Boc.

2.5.2 Photophysical Characterization

2.5.2.1 Absorption and Fluorescence Emission Spectroscopy

The photophysical properties of (**PAG 9**) and **PAG-PEG** compounds were examined by UV-vis absorption and fluorescence emission spectroscopy. The measurements of absorption and fluorescence emission were carried out in different solvents DCM, MeOH, and ACN and it showed no difference in the absorption and emission bands. **Figure 2-1** and **Figure 2-2**, show the UV-vis and fluorecsnce emission of **PAG 9** in DCM and **PAG-PEG** in water respectively. Both of them are showing maximum wavelength of absorption about 385 nm and emission around 520 nm.

Fluorescence quantum yields of PAG 9 and PAG-PEG were also investigated. As shown in the **Table 2-2**, both of them exhibited low fluorescent quantum yield of approximately 0.02.

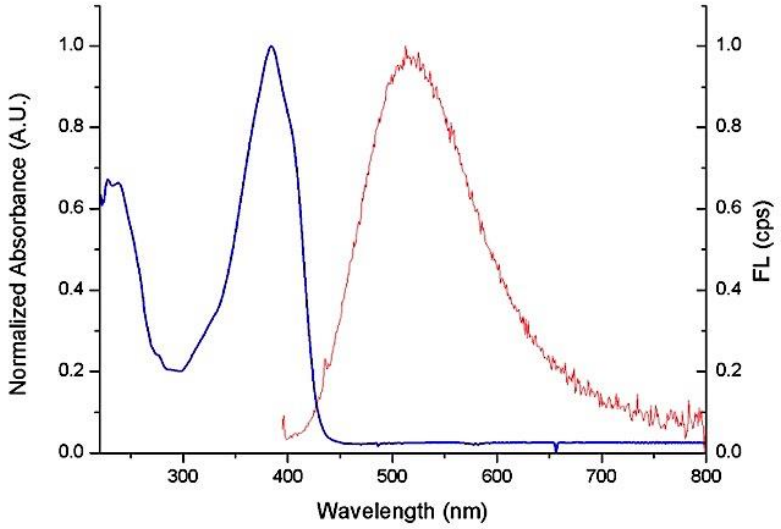

Figure 2-1. UV-vis absorption (blue line) and fluorescence emission (red line) spectra of PAG 9 in DCM.

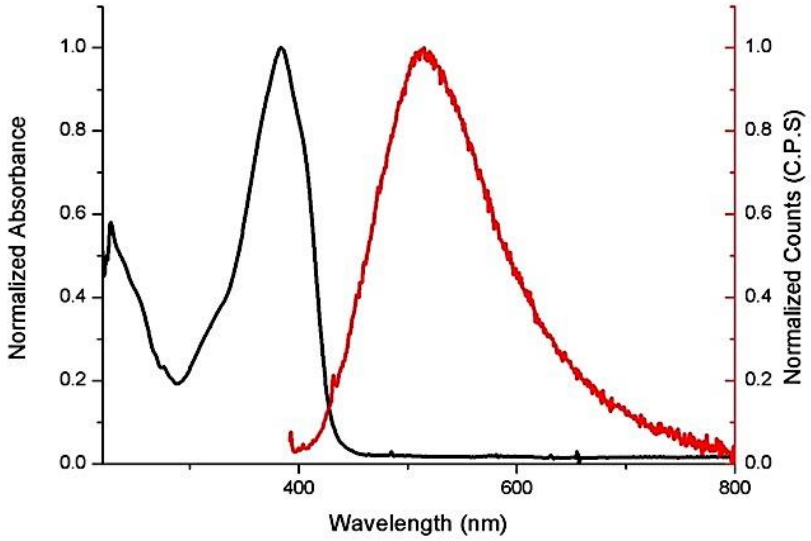

Figure 2-2. UV-vis absorption (black line) and fluorescence emission (red line) spectra of PAG - PEG in water.

Table 2-2. Photophysical Properties of PAGs

PAG	λ ab (nm)	λ em (nm)	Φ_F	Φ_{H+}
PAG 9	384 ± 2	522 ± 2	0.04 ± 0.03	0.41 ± 0.02
PAG-PEG	387± 3	513 ± 2	0.02 ± 0.01	0.39 ± 0.04
SiN-NH-PAG	384 ± 2	533 ± 3	0.08 ± 0.03	-----

Φ_F Fluorescence quantum yield of **PAG 9** in DCM and **PAG-PEG, SiN-NH-PAG** in water with diphenylanthracene in cyclohexane as the standard, Φ_{H+} photoacid quantum yield at 366 nm with rhodamine B base

2.5.3 Two-Photon Properties

Two-photon absorption measurement was also obtained using femtosecond laser system (Coherent, Inc.). Since all of synthesized PAGs have the same system A-π-π-A, PAG-PEG was selected for 2PA cross-section investigation. The 2PA spectra were recorded in DCM at room temperature using open aperture z-scan measurements. The results showed PAG-PEG has a 2PA

cross-section (δ_{2PA}) around 120 GM as shown in **Figure 2-3,** and **Table 2-3.** This gives a good promising result for using them as a 2PA photodynamic therapy agent.

Table 2-3. Two-photon absorption of PAG-PEG properties

Solvent	DCM
λ_{Abs} (nm)	385 ± 1
λ_{Em} (nm)	513 ± 1
Φ_{FL}	0.02 ± 0.002
δ_{2PA} (GM)	120

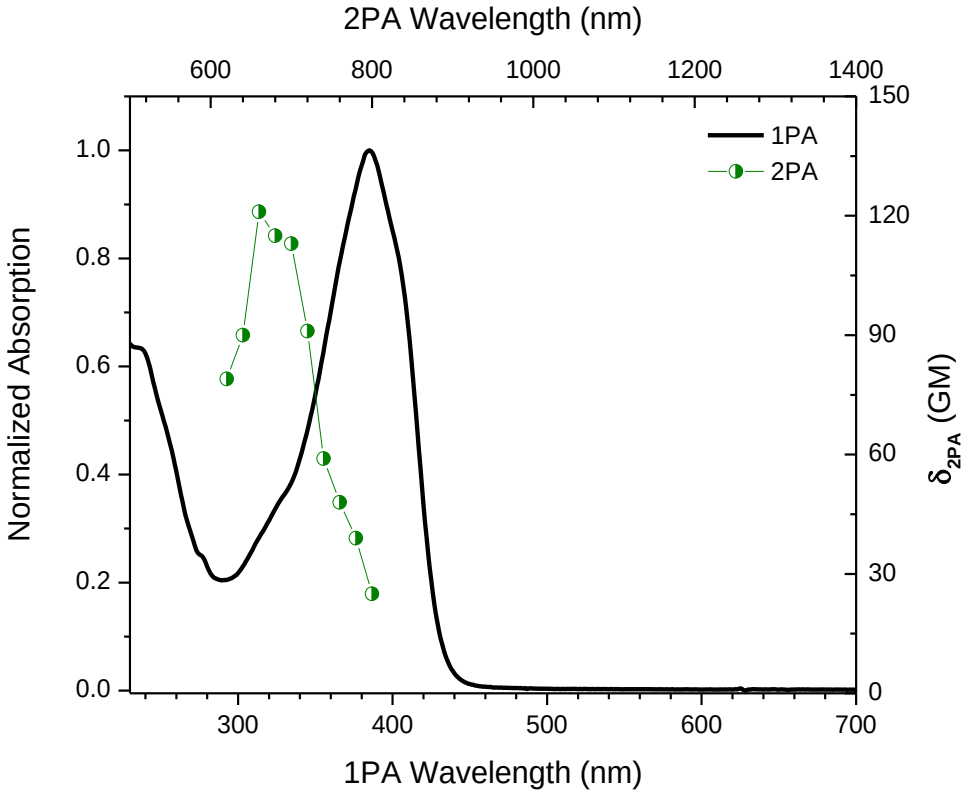

Figure 2-3. One-Photon Absorption (1PA) in DCM (black line), and two-photon absorption (2PA) in DCM (green line) spectra for PAG-PEG.

2.5.4 Calculation of Photoacid Generator Quantum Yield

Photoacid generator quantum yield was measured by using rhodamine B base as sensor in DCM. Rhodamine B base represents a closed-ring structure as shown in **Figure 2-4,** when protonated from an acid the close ring opens yielding rhodamine B.

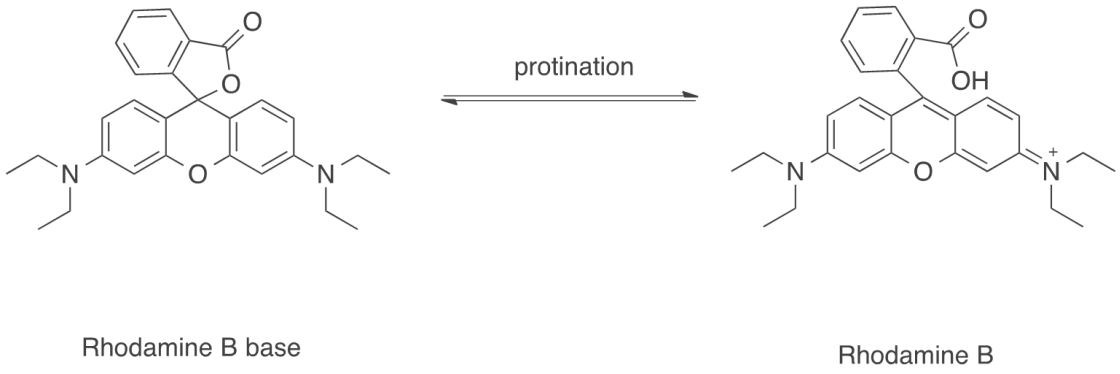

Figure 2-4. Rhodamine B base and rhodamine b structures.

Rhodamine B base has no absorption peak in the area 550 nm; when protonated the absorption peak at 550 nm will increase gradually. Based on **Figure 2-4**, we measured the photoacid quantum yield using rhodamine B base as an indicator. PAGs at concentration of 10^{-4} M were mixed with rhodamine B base at concentration 10^{-5} M and illuminated for different time intervals as shown in **Figure 2-5.** The **PAG 9**, **PAG-PEG** exhibited high photoacid quantum yields of about 0.4 as shown in **Table 2-2**

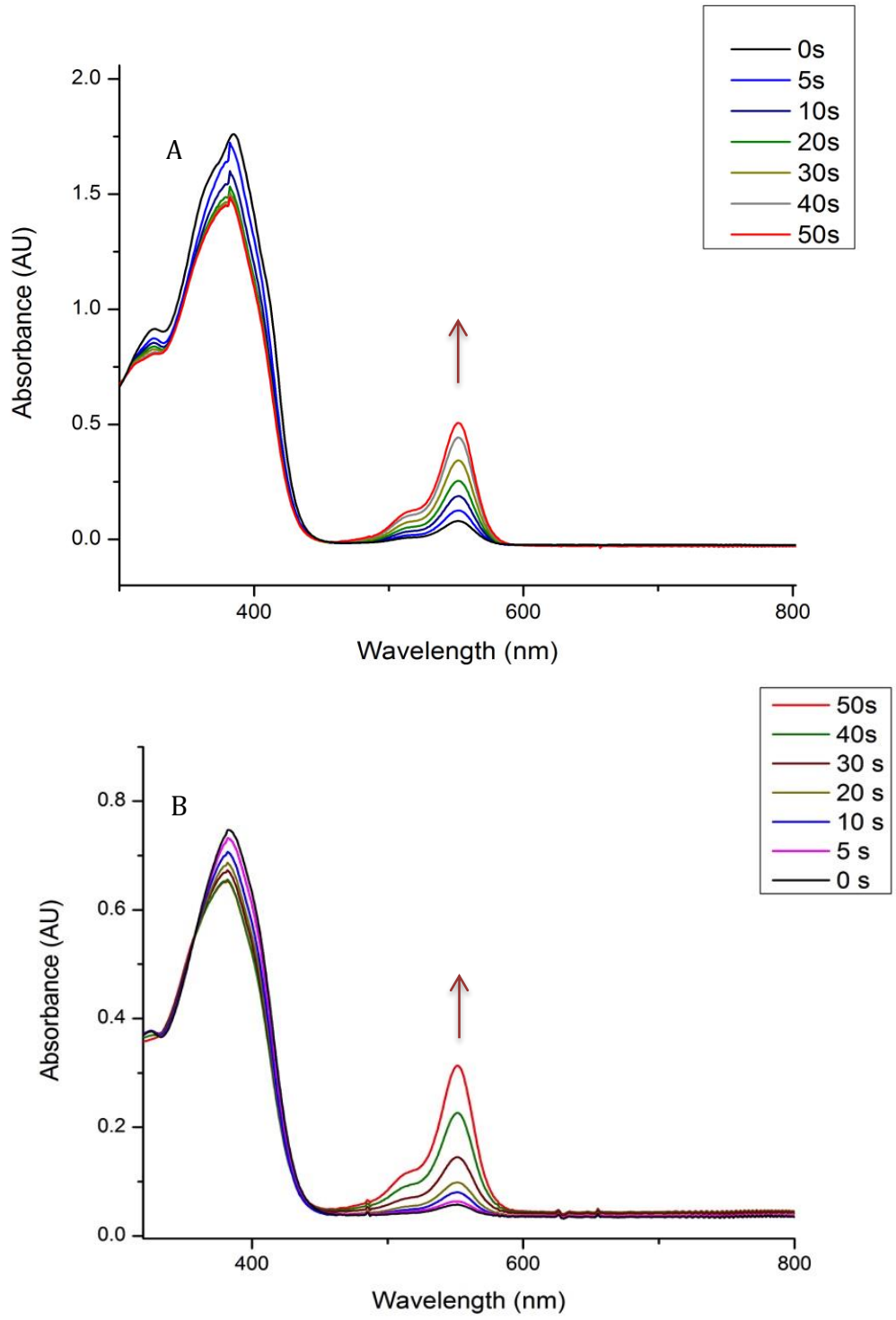

Figure 2-5. (A) Absorption spectra of 10^{-4} M concentration of PAG 9 mixed with 10^{-5} M concentration of RhB base as indicator using 87 µW @ 366 power light, (B) 10^{-4} M concentration PAG-PEG mixed with 10^{-5} concentration of RhB base as indicator, using 92 µW @ 366 nm power light for irradiation with different times.

2.6 Characterization of Silica Nanoparticles

2.6.1 UV-vis Characterization

Silica nanoparticles dispersed in water solution were characterized by measuring UV-Vis spectra using Agilent 8453UV-vis spectrophotometer as shown in (**Figure 2-6 A, B**); it is clearly indicated that the absorbance peak at λ_{abs} 384 nm is related to PAG.

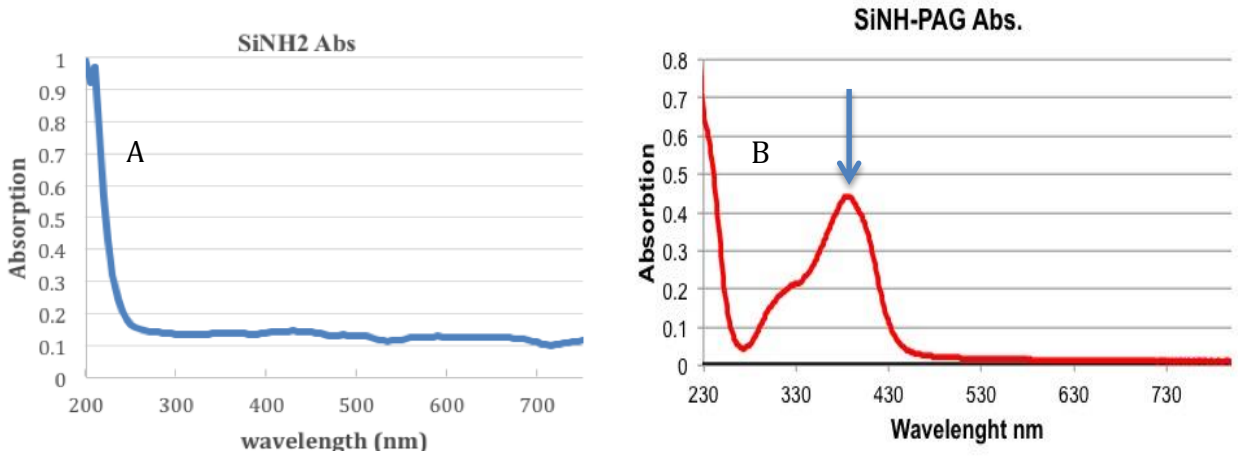

Figure 2-6. A- Absorption spectra of surface modified SiNPs Capped with amine groups, B- Absorption spectra of surface modified SiNPs covalently bonded with PAG 9 via amid links dispersed in water, λ_{abs} 384 nm.

2.6.2 Particles Size

Silica nanoparticles sizes and zeta potential were measured with a Zetasizer Nano system and the results compared to that before and after coupling with **PAG 9**. Size of silica nanoparticles capped with amine groups before coupling was (4 nm), after being covalently bonded with PAG 9 via amid links became (9 nm), while the zeta potential did not show any significant different before and after coupling as shown in **Table 2-4** and (**Figure 2-7**).

Table 2-4. Particle size and zeta potential of silica nanoparticles functionalized with amino groups before and after coupling with PAG 9.

Particle size SiN-NH_2	Particle size SiN-NH-PAG
4 nm	**9 nm**

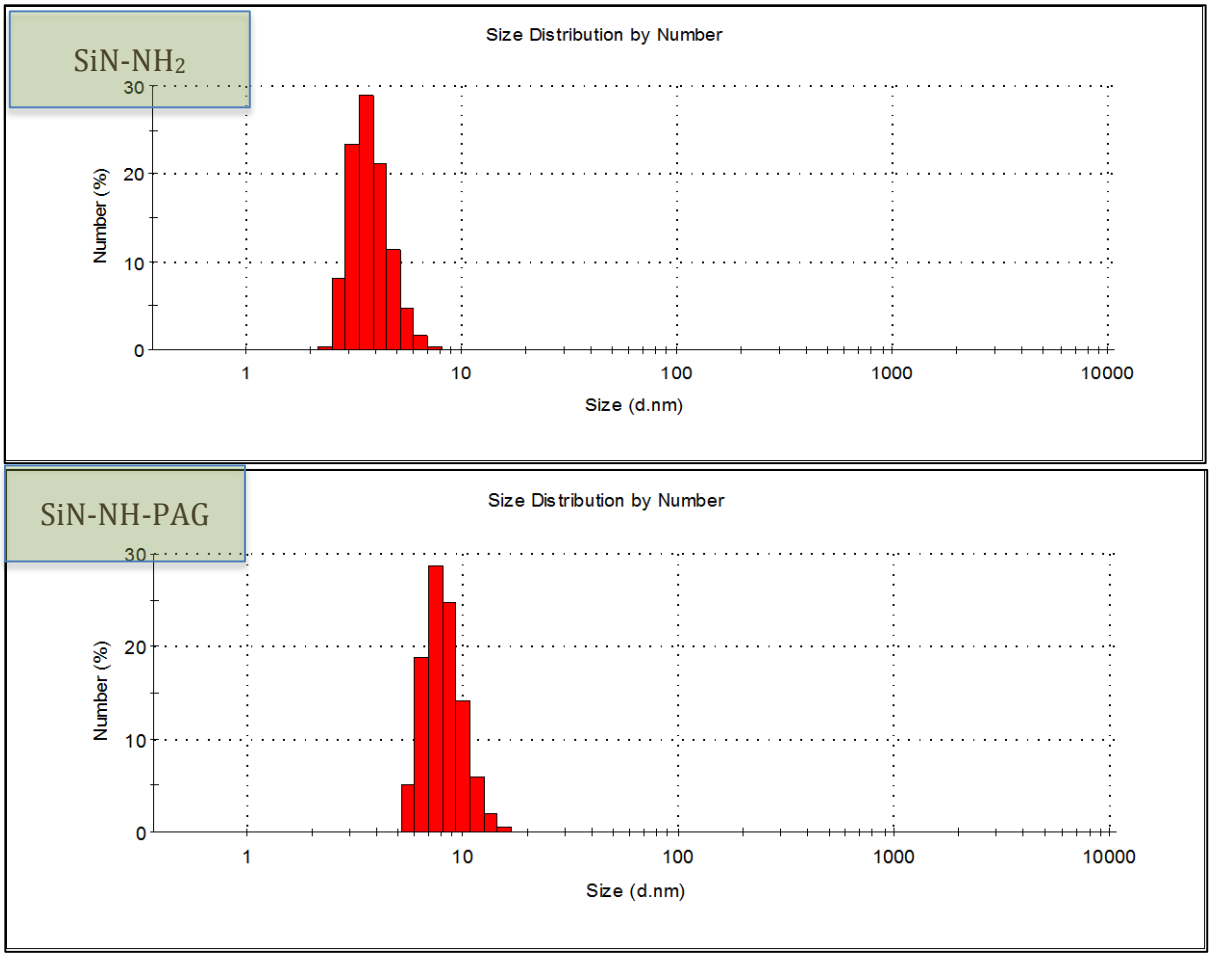

Figure 2-7. Silica Nanoparticles size Functionalized with Amine Groups before and after coupling with PAG 9 using Zetasizer Nano system.

2.6.3 [1]HNMR Characterization

Further characterization was done using [1]HNMR and the results indicate an obvious PAG peak at 7.69 ppm as shown in **Figure 2-8 B**.

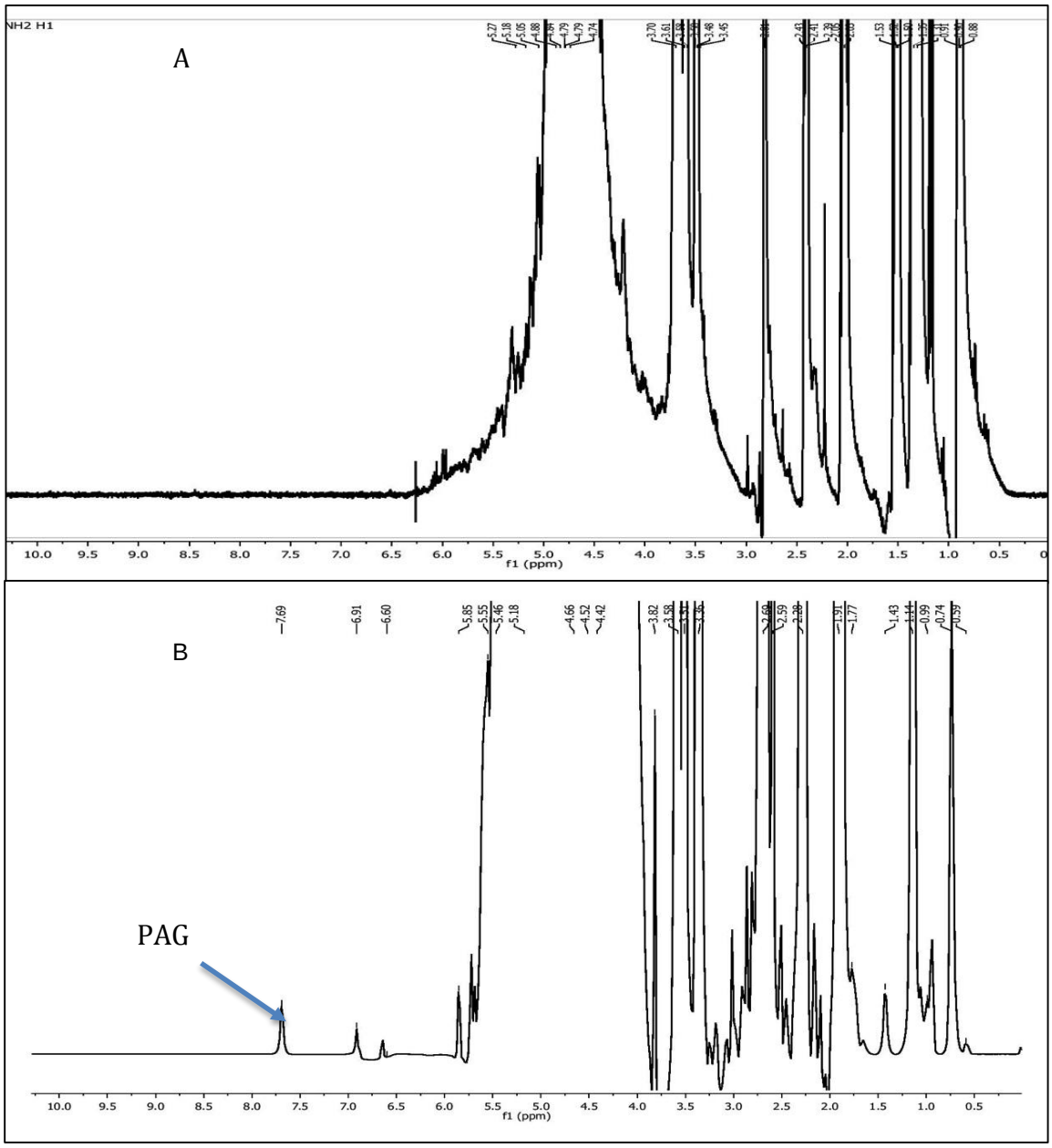

Figure 2-8. A- [1]H-NMR for Silica nanoparticles functionalized with amine (SiN-NH_2), B- [1]HNMR for Silica nanoparticles covalently bonded with PAG (SiN-NH-PAG) in D_2O.

2.7 Conclusions

Design and development of new photodynamic therapy agent (PAG) is reported here. PAG was conjugated first with polyethylenegylcole (PEG) polymer PAG-PEG. Second PAG was covalently bonded with synthesized ultra-small size silica nanoparticles surface modified with amine groups to get a formal and ideal agent for photodynamic therapy treatment that can be injected in vivo. These water-soluble derivatives were fully characterized using ^{1}HNMR and ^{13}C and mass spectroscopy. In addition, photophysical properties were also measured. Generally PAG fluorescence quantum yield is around 0.0 ± 0.02 while photoacid quantum yield is around 0.41 ± 0.02. A 2PA cross-section for PAG was also measured and found to be around 120 GM. These results encourage us to test them (water soluble agents) in the HCT-116 cells and compare the results in chapter 3.

CHAPTER 3. TESTING AND MONITORING OF THE NEW PHOTODYNAMIC CANCER THEARPY AGENT WITH HUMAN COLORECTAL CARCINOMA (HCT-116) CELL

Photodynamic therapy (PDT) processes with singlet oxygen sensitizers are facing a lot of difficulties and complexities since they rely heavily on the concentration of oxygen present in the tissue to be treated. Most cancer lesions have low levels of oxygen (hypoxic) because of the poor vasculature of these regions. As a result, these hypoxic cells have a resistance to death by irradiation using photosensitizer compounds. Herein, we test new photodynamic therapy (PDT) agents, such as an oxygen-independent agent sulfonium salts (photoacid generator) that cause a pH drop within cancer cells by generation of acid within cytosol.

Two different water-soluble photoacid generators (PAG) have been tested using HCT-116 cell line and the results compared. First, PAG was connected with ≈ 23 units of polyethylene glycol (PEG) groups PAG-PEG to produce a highly water solubility and low cytotoxicity compound. Second, PAG was conjugated with highly monodispersed silica nanoparticles ultra-small size functionalized with amine groups via amid links. Each particle has an average size of 9 nm with PAG monomers attached to the surface of each particle. PAG covalently incorporated within the delivery vehicles and is anticipated to solve the drawback of their premature release, thus enhancing the results of PDT. The PDT processes were completed using one photon absorption (1PA) of endocytosed photoacid generator (PAG) and the results indicated that silica nanoparticles with PAG (SiN-NH-PAG) induced cell death more than (PAG-PEG). The increased effectiveness of the nanoparticles is assumed to be because of the large number of PAG groups present on the nanoparticles. Which results in a greater number of PAGs present per unit volume of substrate, compared to the single molecule species. The drop in the

pH in the Lysosome was measured around 0.3 units (approximately pH $\leq$ 4.4) inside the lysosomes and this is undoubtedly a good event as most cells underwent necrosis. Cells were imaged with confocal microscope (Olympus IX-81) at 1 min interval for 4 hours by using DIC channel.

3.1 Introduction

Photodynamic therapy (PDT) has been established as a cancer treatment which employs light sensitive nontoxic compounds that when irradiated with light at a specific wavelength results toxifying of the target area, namely malignant and diseased cells and tissue.[72] PDT has been known for hundred years, but only at the end of the nineteenth century did it became widely used and utilized. Usually the first component is a photosensitive compound (photosensitizer) that localizes to target cell. The second component is light of specific wavelength to activate the sensitizer. When the photosensitizer is promoted to an excited state in the presence of oxygen, it will transfer energy from the light to the oxygen to generate singlet oxygen. The reactive oxygen species will attack any organic compounds and are highly cytotoxic.[73] Photodynamic therapy with photosensitizer compounds has a lot of problems because of the low oxygen concentration in the cancer cells (hypoxic). In order to make it successfully work with photosensitizer, we need to carefully balance three important factors and these factors should be presented at the time of therapy: Oxygen saturation of the tissue (the most important condition), the photosensitizer concentration should be enough throughout the lesion, and enough intensity of light should be available. All these conditions are present in heterogeneous concentrations and doses even in a single gland like the prostate. This makes the process difficult and compromised the production of singlet oxygen photosensitized.[74,75.]

A challenge that PDT has for a considerable period of time is the production of singlet oxygen in an oxygen-depleted environment. Healthy tissues have very well structured vessels and the inner walls are conformed by well-differentiated endothelial cells. On the other hands, the tumor vessels have poor morphology conformed by immature cells in a mesh like construction, which give a leaky character to the vessel. This leaky property related to these vessels, produce a hypoxic and acidic environment.[76] Since the hypoxic environment has a limited amount of oxygen to be excited, this leads to poor outcomes in the production of singlet oxygen. Furthermore, this will lead to ischemia, a malady which compromises the flow of oxygen to the tumor and hinders complementary chemotherapeutic agent delivery via the bloodstream.[75,77]

Since nanomaterials have biological and chemical flexibility, nontoxic, and multimodality of the surface, they become revolutionized the fields of medicine (in both diagnosis and therapy), bioimaging, and photonics.[78-80] Recently, nanomaterials have been widely used in the application of gene delivery as DNA carriers,[81] photodynamic therapy carrying the photosensitizer,[82, 83] and bioimaiging nanopropes.[70,84] Most of the PAGs have hydrophobic nature, for that reason, we trying to develop an ideal photoacid generator formulation that can be easily used and injected in vivo. Recently, many methods have been reported to achieve stable aqueous dispersion as well as site-specific and time controlled delivery of the therapeutic agents by using a delivery vehicle.

Because drugs are not a prerequisite for their therapeutic action in PDT,[85] covalently incorporating the PAG within the delivery vehicles is anticipated to solve the drawback of their premature release thus enhancing the results of PDT.

Herein, we test new photodynamic therapeutic agents (photoacid generator, PAG) **Figure 1-3**. These afforded oxygen-independent PDT by inducing imbalance of the pH within the cytosol of the cells that were targeted instead of inducing cell death by singlet oxygen from photosensitization, also constructed a molecule with a greater extinction coefficient for 1PA and a greater 2PA absorption cross section. In both cases we tailored the molecule to absorb at longer wavelengths, which promotes deeper penetration of therapy. Also hydrophilic **PAG 9** was conjugated with silica nanoparticles and polyethylene glycol (PEG) group ≈ 23 units making it highly water-soluble and low cytotoxicity. We synthesized silica nanoparticles that consist of a highly aqueous stable design of organically functionalized amine groups covalently bonded with PAG molecules via amid link with ultralow size (9 nm). These nanoparticles are well suited for in vivo experiments when compared with larger sizes. These results in a highly monodispersed, and stable species in aqueous solution making theme able to generate acid molecules during the photoactivation and treat the cancer.

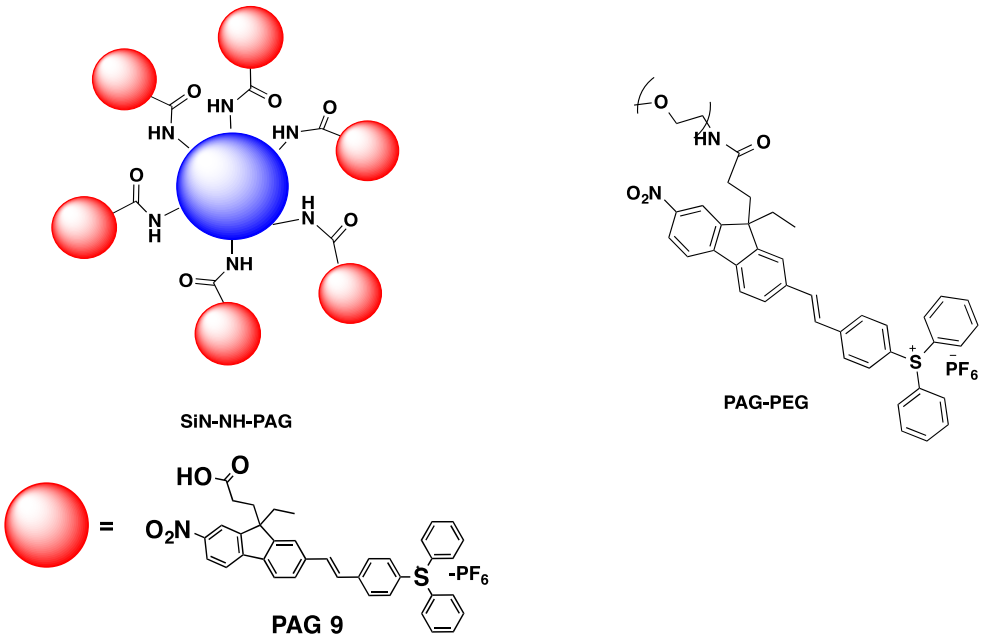

Figure 3-1. Hydrophilic PAGs (SiN-NH-PAG), and (PAG-PEG).

3.2 Materials and Methods

3.2.1 Cell Culture

Cells HCT-116 (ATCC, USA) were cultured in RPMI-1640 medium, supplemented with 10% FBS, 1% penicillin-streptomycin, at 37 C in a 95% humidified atmosphere containing 5% CO_2. Cells were splitted every two days when they reach 70-90% confluency. Briefly, soaking all medium from the plate then 2 ml of Trypsin was added (to detach the cells from the bottom of the plate) and put it back in incubator. After 10 min., (8 ml) of fresh medium was added and the solution was centrifuged for 5 min at 1000 rpm speed. The old medium was removed and (10 ml) of fresh medium was added and then split in a new plate and incubated again.

3.2.2 Cell Counting (Hemocytometer)

Cells were counted using chamber called a Hemocytometer. A Hemocytometer contains a thick glass microscope slide with a grid (perpendicular lines scraped in the middle). In this grid, there are specific dimensions so the area covered by the lines is known and counting number of cells in specific volume of solution becomes possible.

A coverslip was placed over the counting surface and then cell suspensions were loaded (20ul) a using pipette tip into one of V-shaped wells as shown in **Figure 3-2**. Then, the loaded Hemocyometer was placed on microscope stage and cells were counted.

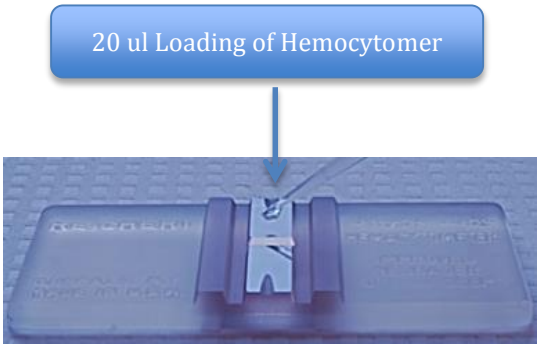

Figure 3-2. Loading the Hemocytometer

The Hemocytometer grid contains nine squares, each of them is 1 mm **Figure 3-3.** The central hemocytometer counting area contains 25 large squares and each one has 16 smaller squares. Cells were counted only on the lines of two sides of the large square in order to avoid counting cells twice. Dead and viable cells were distinguished according to their shape and size. Cell concentration was calculated using the following formula:

Total cells/ml = (Total cells number / No. of Squares) × 10000 cells/ml

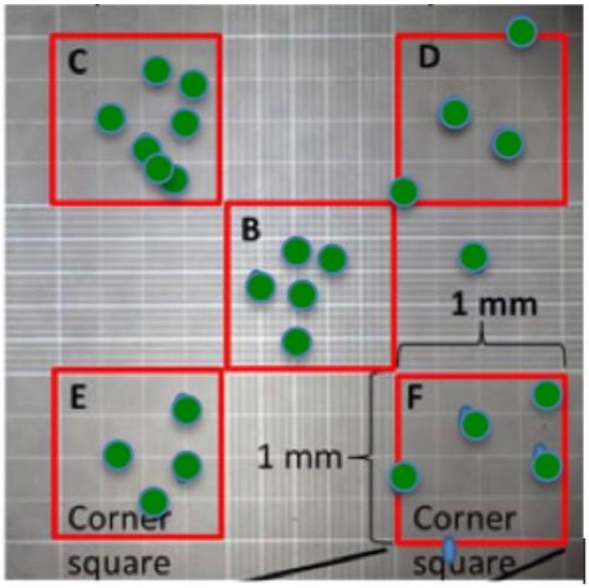

Figure 3-3. Hemocytometer counting cell

3.2.3 Dark Cytotoxicity

In 96-well black wall clear bottom plates (Corning, USA) HCT-116 cells were seeded at 8×10^4 cells/well and incubated for 48 hours. For dark cytotoxicity experiment, PAG-PEG was diluted to 1.5 μM, 3.12 μM, 6.25 μM, 12.5 μM 25 μM, 50 μM, and 100 μM from the stock solution; SiN-NH-PAG was diluted with different concentrations starting with 0.6 μM, 1.25 μM, 2.5 μM, 5 μM, 10 μM, and ending with 20 μM. Cells were then incubated with diluted PAG-PEG or SiN-NH-PAG for another 24 hours as shown in **Figure 3-4**. Cell viability was determined by adding 20 μL of CellTiter 96 Aqueous One Solution Reagent (Promega, USA) into each well, followed by further incubation for 2 h. Absorption at 490 nm was measured for the corresponding MTS-fomazan with a SpectraMax M5 Microplate Reader. The results were then compared with a control, which was incubated in the absence of the PAGs to calculate relative cell viability.

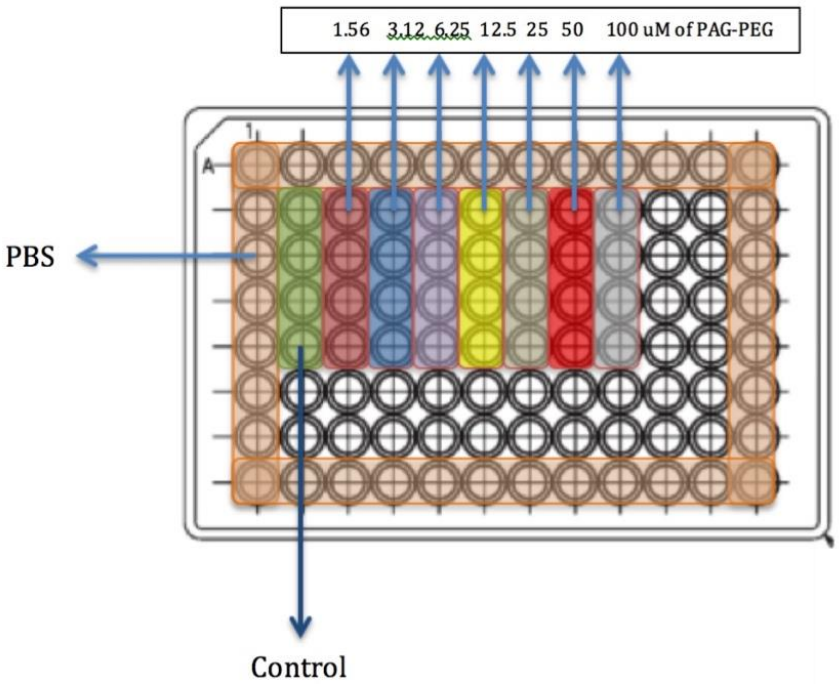

Figure 3-4. Dark cytotoxicity cell culture scheme, using 96-well black wall clear bottom plates.

3.2.4 Photo Cytotoxicity

For photocytotoxicity experiment, 50 μM of **PAG-PEG** or 10 μM **SiN-NH-PAG** was added to the HCT-116 Cells as shown in **Figure 3-5.** The 96-well black well plate was placed on an inverted microscope (Olympus IX81) coupled with a 100 W mercury lamp. The distance between the bottom of the plate and the objective was set at 1 cm in order to irradiate the whole well with UV light. A customized filter cube was employed (Ex 377/50, DM 409, Em 460/50) to excite PAG. The final power reaching the plate was 5.4 mW/cm^2. Different irradiation times were used (0 min., 1 min., 5 min., and 10 min.). After irradiation, the plate was incubated for another 24 hours before the cell viability was measured.

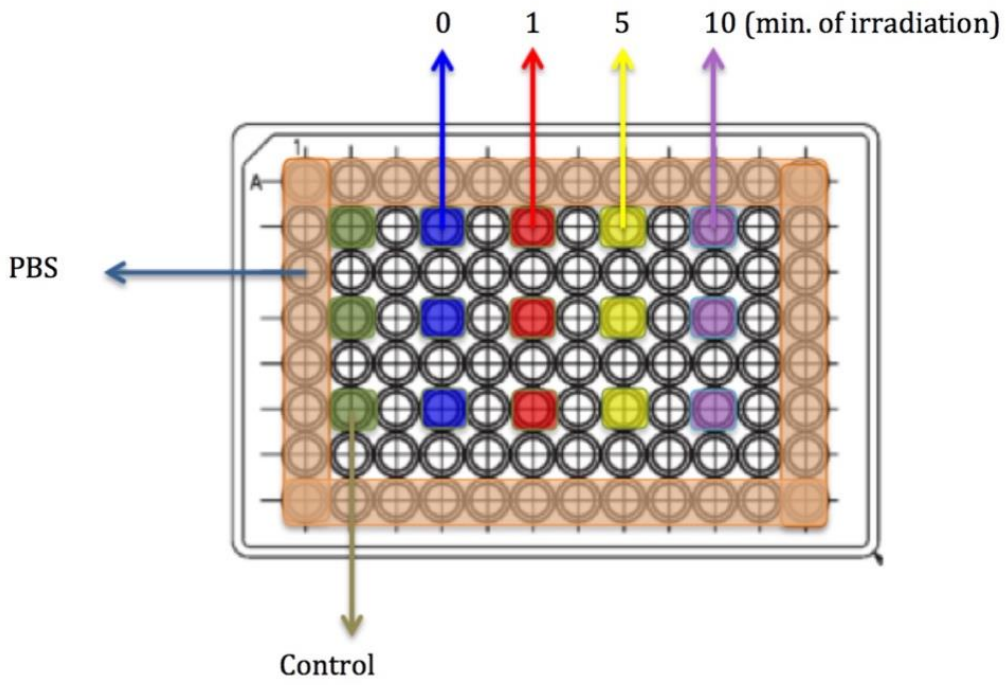

Figure 3-5. Photocytotoxicty cell culture scheme using 96-well black wall clear bottom plates.

3.2.5 Lysosome Colocalization

In 12 mm poly-D-lysine functionalized coverslips HCT-116 cells were cultured for 48 hours. PAG-PEG was then added into the cells at a concentration of 50 μM with LysoTracker Green at 2 μM for 1 hour. After that, coverslips were washed with PBS two times. Coverslips were imaged using Olympus IX-81 confocal microscope. A customized filter (377/50, 409, 460/50) was used for PAG-PEG and (Ex 477/50, DM 507, DM 536/40) was used for LysoTracker green.

3.2.6 Live Cell Imaging of PAG-PEG and SiN-NH-PAG

In 40 mm poly-D-lysine functionalized coverslips, cells were cultured for 48 hours. After that, PAG-PEG or SiN-NH-PAG was added to the cells. 24 hours later, the coverslip was washed with PBS twice and set onto a bioptics live cell-imaging chamber. After irradiation with UV lamp for 2000 ms (5.4 mW/cm^2) cells were imaged with confocal microscope (Olympus IX-81) at 1 min interval for 4 hours by using DIC channel. Cells were kept in 37 ^0C RPMI-1640 whole culture medium with 5% CO_2, while imaging.

3.2.7 Calculation of the Increasing in Acidic Contain of Lysosome

In order to calculate the increasing in the acidic contain of lysosome in vivo, cells were incubated with PAG-PEG at 50μM concentration for 24 hours. Then, 2mM of LysoSensor Green (Invitrogen, USA) was added for another 2 hours. After 2000 ms irradiation, cells were imaged at 1 min interval for 60 min with FITC filter cube (Ex 477/50, DM 507, DM 536/40) to collect fluorescence of LysoSensor Green. The fluorescence intensities were calculated at different time points with SlideBook. Cells were kept in 37 ^0C RPMI-1640 whole culture medium with 5% CO_2, while imaging.

3.2.8 Estimation of Lysosomal pH Drop

The pH drop in Lysosome was measured according to method reported by Zhu et al.[74] A solution of PAG-PEG (50μM) and Rh B Base (0.1mM) in DCM was mixed in the dark and exposed in order to make a dose dependent calibration curve. By assuming the number of acid molecules generated the same as the number of Rh B Base molecules converted to Rh B+.

3.3 Results and Discussion

3.3.1 Dark Cytotoxicity of SiN-NH-PAG and PAG-PEG

An ideal phototherapeutic agent needs a PAG compound that exhibits low cytotoxicity in the absence of light and induces high percentage of cell death when illuminated at certain wavelength. In order to evaluate the intrinsic toxicity of the PAGs, an assay of cell viability was done in the dark (dark viability) to prevent the production of photoacid and enabling the choice of suitable concentration for photodynamic therapy.

The cytotoxicity was evaluated using a standard MTS assay.[86] HCT-116 (human colorectal carcinoma) were incubated with different concentrations of 1.5, 3.12, 6.25, 12.5, 25, 50, 100μM solutions of **PAG-PEG** in medium for 24 h at 37 ^{0}C. As shown in **Figure 3-6,** cell viability of HCT-116 Cells incubated with up to 100 μM of **PAG-PEG** were quite close to 100%, which means that **PAG-PEG** at that concentration exhibited almost no level of cytotoxicity.

Different concentrations of **SiN-NH-PAG** 0.62, 1.25, 2.5, 5, 10, and 20 μM were also incubated with HCT-116 cells in medium for 24 h at 37 ^{0}C and the results indicates that

SiN-NH-PAG with up to 10 μM was close to 100% viability as shown in **Figure 3-7** which indicated that **SiN-NH-PAG** at that concentration also exhibited almost no level of cytotoxicity. Even higher concentrations of **SiN-NH-PAG** were not able to do much damage to cells. After incubation with 20 μM about 77% of HCT-116 cells were still viable.

All these data above demonstrate that the dark cytotoxicity of both **PAG-PEG** and **SiN-NH-PAG** are very low making them suitable for being applied to photodynamic therapy experiments.

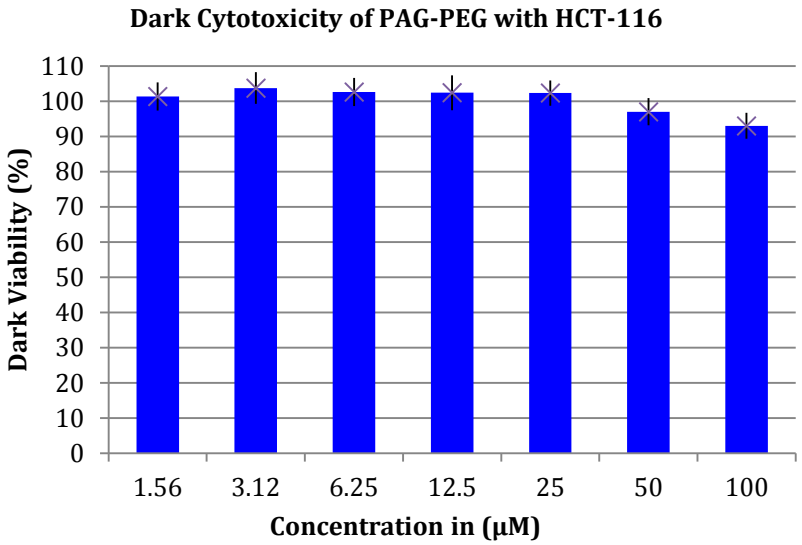

Figure 3-6. Dark cytotoxicity of HCT-116 cells incubated with PAG-PEG and exhibit low cytotoxicity

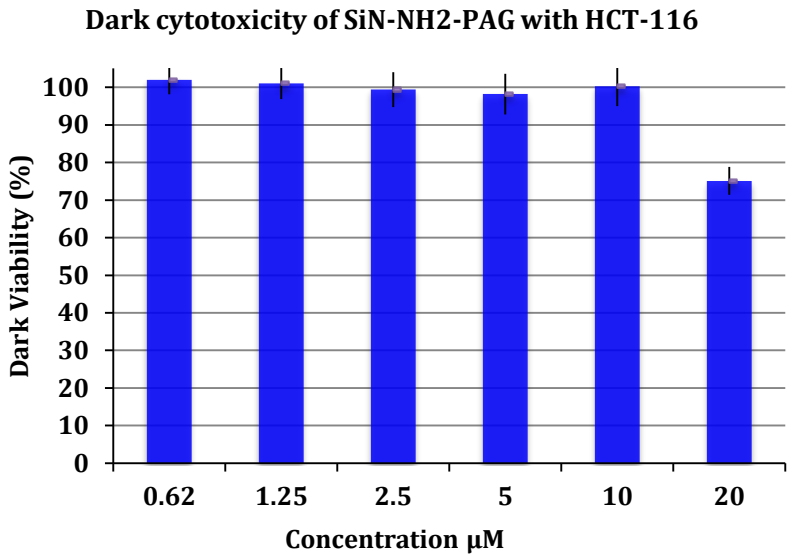

Figure 3-7. Dark cytotoxicity of HCT-116 cells incubated with SiN-NH-PAG and indicates low cytotoxicity at 10 µM.

3.3.2 Photo Cytotoxicity of SiN-NH-PAG and PAG-PEG

Photo-cytotoxicity was achieved (exposure experiment) by using 50µM concentration of the **PAG-PEG**. This concentration exhibited the most appreciable changes in viability (from dark viability to postexposure viability) **Figure 3-6**.

As shown in **Figure 3-8**, HCT-116 cells incubated with 50 µM of **PAG-PEG** with 10 min exposure, promoted a drop from 97% viability to 64% viability, a result consisted with the photoacid quantum yield **(Table 2)**; the cell death induction was directly proportional to the amount of acid generated. For **SiN-NH-PAG,** 10µM concentration was used since this concentration showed the most appreciable changes in dark viability **Figure 3-7**; cells were incubated with 10µM concentration of **SiN-NH-PAG.** As shown in **Figure 3-9,** within 10 min exposure promoting a drop from 98% viability to about 42% viability.

Based on the results from the photocytotoxicity experiments, we indicate that **SiN-NH-PAG** works more efficiently as a PDT agent than **PAG-PEG**; even though the concentration of **SiN-NH-PAG** was 10 μM, which was less than the concentration of **PAG-PEG** (50 μM). Solubility of nanoparticles was found to be higher in comparison to the single molecular PAG due to the salt form of this sulfonium PAG results in increased solubility of silica nanoparticles. A comparison of the silica nanoparticles **SiN-NH-PAG** and single molecules **PAG-PEG** shows that the former have a greater efficacy at a concentration of 10 □M. Our construction of these nanoparticles is based on the surface modification of the silica surface with amine groups followed by the addition of the PAG molecules via amid links. The increased effectiveness of the nanoparticles is assumed to be because the large number of PAG groups present on the nanoparticles resulting in a greater number of PAGs present per unit volume of substrate compared to the single molecule species. Also the biocompatibility and high efficiency taken up of silica nanoparticles by cells add more efficient properties for PAG agent.

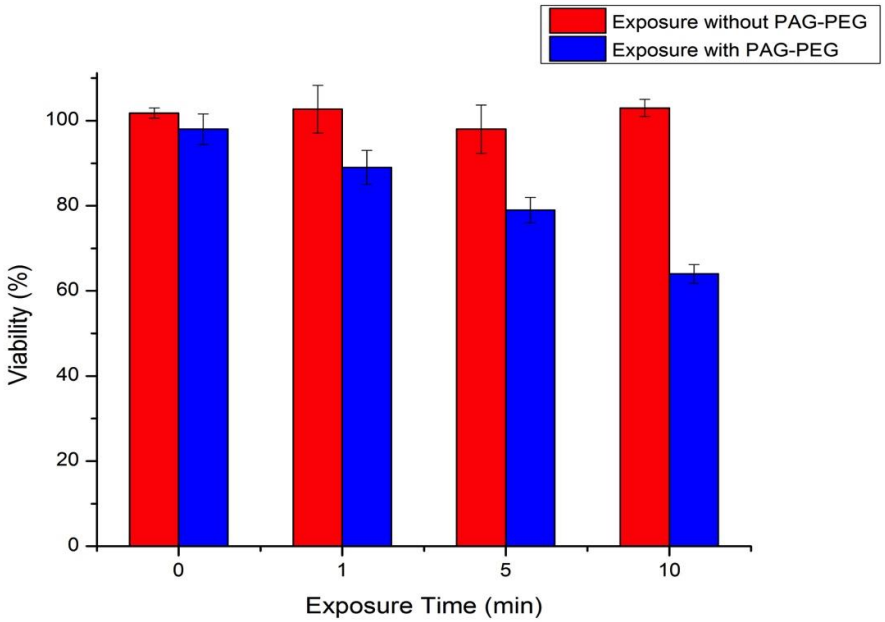

Figure 3-8. Postexposure viability of HCT-116 cells with 50 μM of PAG-PEG concentration exhibited low intrinsic (dark) cytotoxicity and high postexposure cytotoxicity.

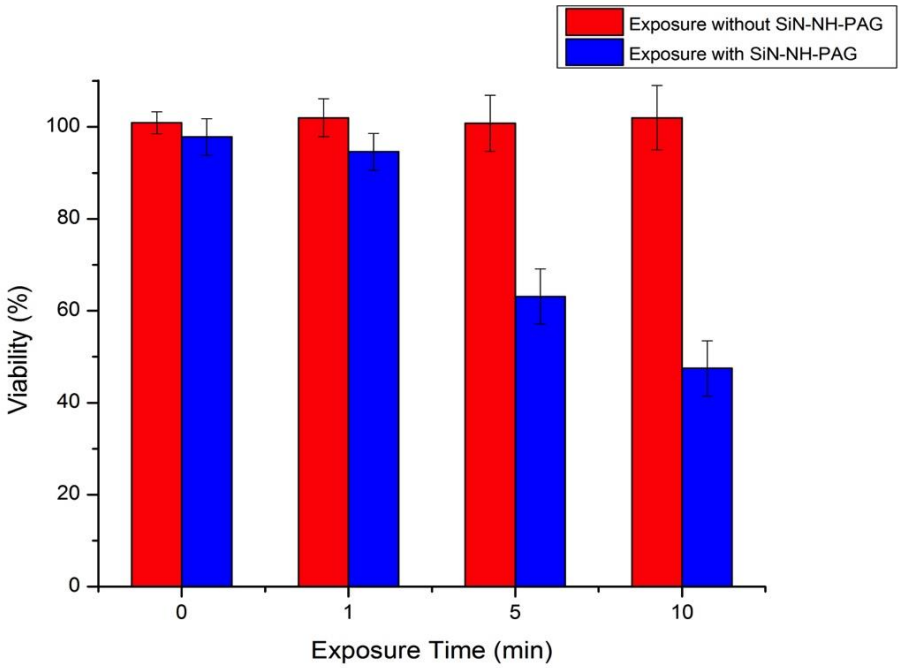

Figure 3-9. Postexposure viability of HCT-116 cells with 10 μM of SiN-NH-PAG concentration exhibited low intrinsic (dark) cytotoxicity and high postexposure cytotoxicity

3.3.3 Colocalization of PAG and LysoTracker Green

In order to investigate and know where the **PAG-PEG** travels to inside HCT-116 cells, cells were incubated with **PAG-PEG** and LysoTracker Green. **PAG-PEG** fluorescence was collected inside cells (**Figure 3-10, C**), showing a good uptake efficiency of **PAG-PEG**. Overlay image (**Figure 3-10, D**) exhibited a good colocalization between **PAG-PEG** and LysoTracker Green, and indicated PAG-PEG mainly built in lysosomes.

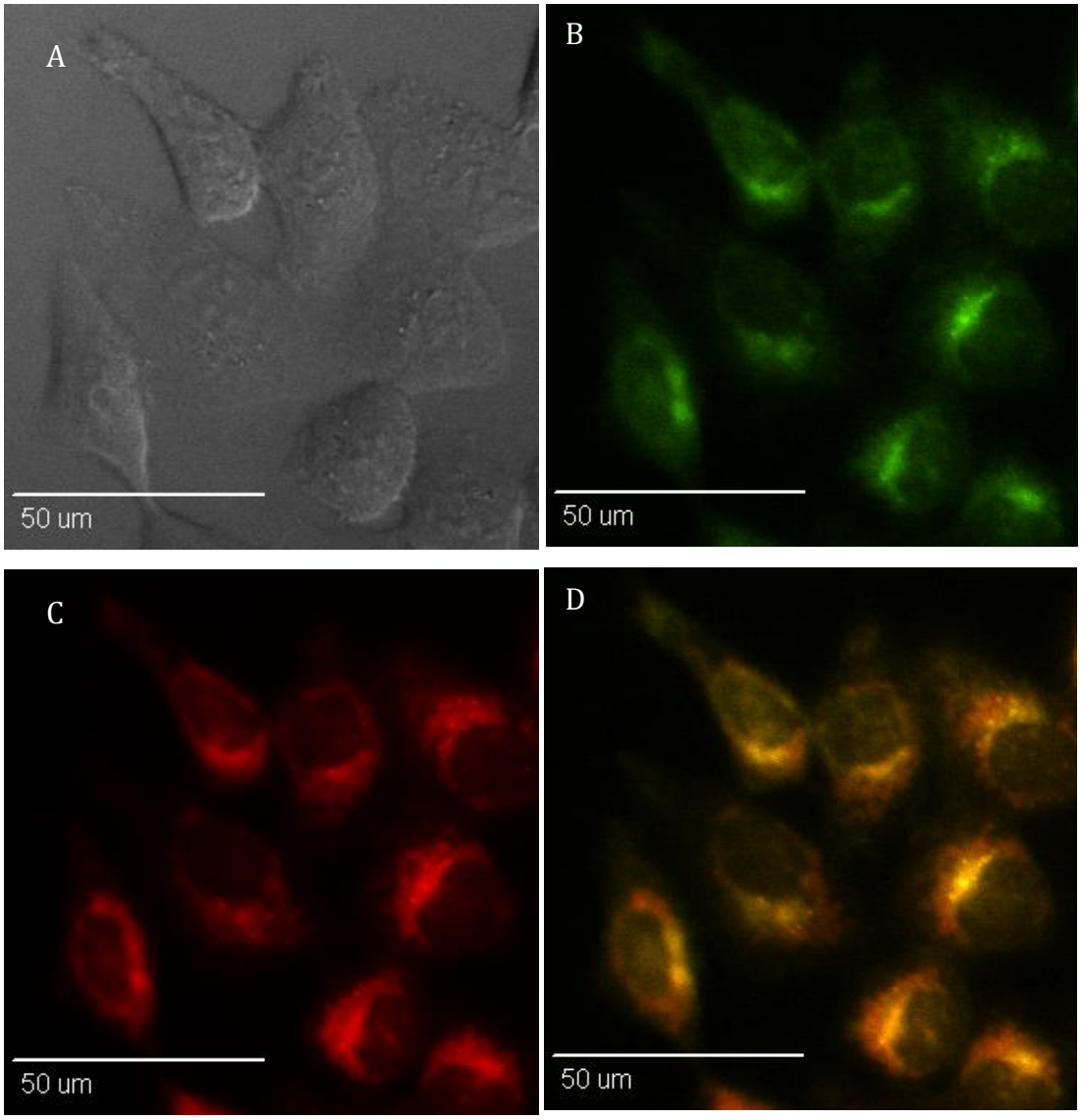

Figure 3-10. DIC (a) and confocal fluorescence micrographs of HCT-116 cells incubated with PAG-PEG using (50 μM) and (b) Lysotracker Green. (c) Shows the PAG-PEG in cells and colocalization in d (overlay of b and c) with Lysotracker green shows the PAG-PEG mainly build up in lysosomes and endosomes. Using scale bar 50 μm.

3.3.4 The Increasing in Acidic Contain of Lysosome

LysosSensor Green has been reported to be an acidic pH monitoring dye within the cells.[25] We used this dye to verify the decreasing in the lysosomal pH. The quantum yield of LysoSensor Green is known to increase when the acidic compartment increased.[25] The increase in the fluorescence intensity as a function of exposure was indeed observed within the cells that were incubated with PAG-PEG (50 μM) and LysoSensor Green. This indicates a drop in internal lysosomal pH (of already acidic compartments) followed by irradiation in HCT-116 cells. The drop in the fluorescence intensities as a function of irradiation dose in control HCT-116 cells can be attributed to the photobleaching of the pH indicator, which is acidified by the acidic character of the lysosomes (**Figure 3-11**).

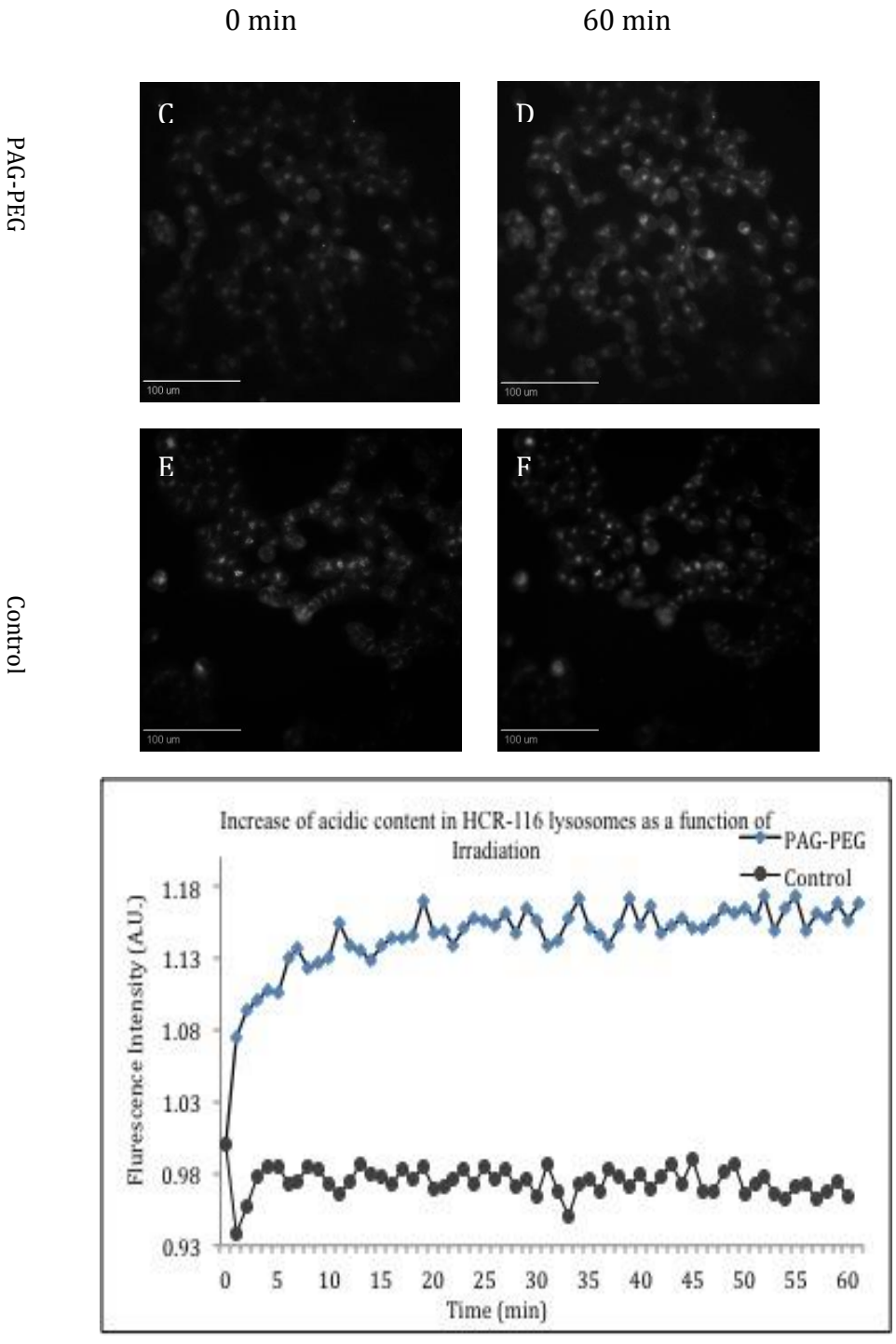

Figure 3-11. Acidic content increasing in the lysosomes as a function of exposure dose in HCT-116 cells incubated with PAG-PEG (50 μM) for 24 h and with 2 μM of LysoSensor Green 2 h. after 5 s irradiation, 5.4 mW/cm2. (C,D,E,F) cells were imaged with 1 min intervals time for 60 min with FITC channel. SlideBook was used to calculate the intensities at different time points.

3.3.5 Estimating Lysosomal pH Drop

It is assumed that the number of acid molecules generated by PAG is the same as the number of Rhodamine B base molecules converted to Rhodmiane B^+, this causing an increase in absorption peak around 555 nm. We estimate that 50 μM concentration of **PAG-PEG** would at least generate 9.1×10^{-6} M of H^+ using radiation dose (10 min). This radiation dose caused cell viability to be reduced to 64%. The lysosomal pH would conservatively be reduced by at least 0.3 pH units to be approximately pH ≤ 4.4 inside the lysosomes and this is undoubtedly a good event as most cells underwent necrosis. The generation of acid molecule was measured to be 9.1 x 10^{-6} M by extrapolation of the calibration curve as shown in **Figure 3-12.**

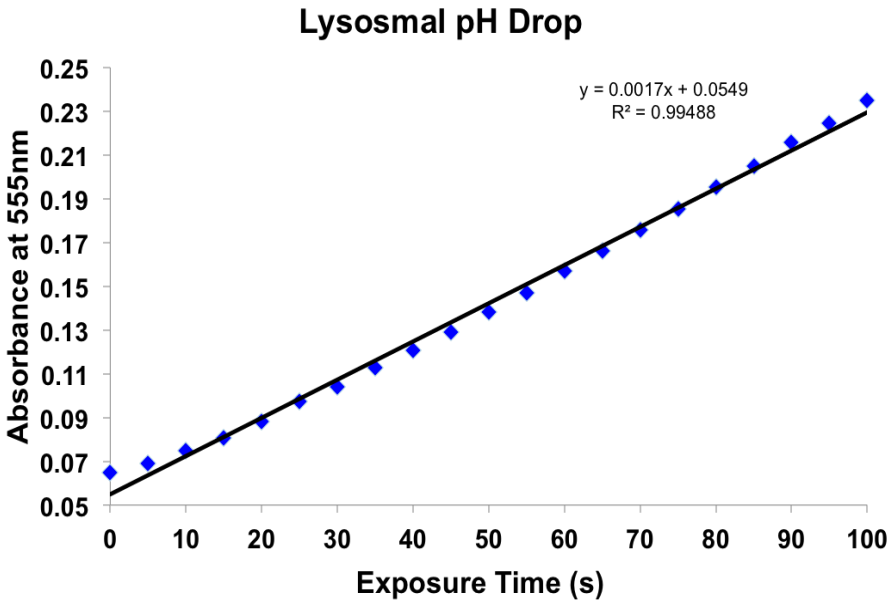

Figure 3-12. A solution of PAG-PEG (50 μM) mixed with Rh B Base (0.5 mM) was exposed to prepare a dose dependent calibration curve using 5.4 mW/cm2 power light.

3.3.6 Excitation of PAG in Cell Free System with LysoSensor Green

In order to demonstrate that the PAG-PEG causes an increase in the acidic content of lysosomes, and eventually increases the fluorescence intensity of LysoSensor Green in cell free system, we mixed around 150 μM of PAG-PEG with LysoSensor Green and then measured the fluorescence intensity at 0 min of irradiation using EDINBURGH INSTRUMENTS FLS980 spectrofluormiter and later on irradiated the mixture at 1 min, 2 min, and 3 min using LOCTITE at 5.4mW/cm^2 power light. We recognized that the fluorescence intensity of LysoSonser green increased as time of radiation increased as shown in **Figure 3-13**.

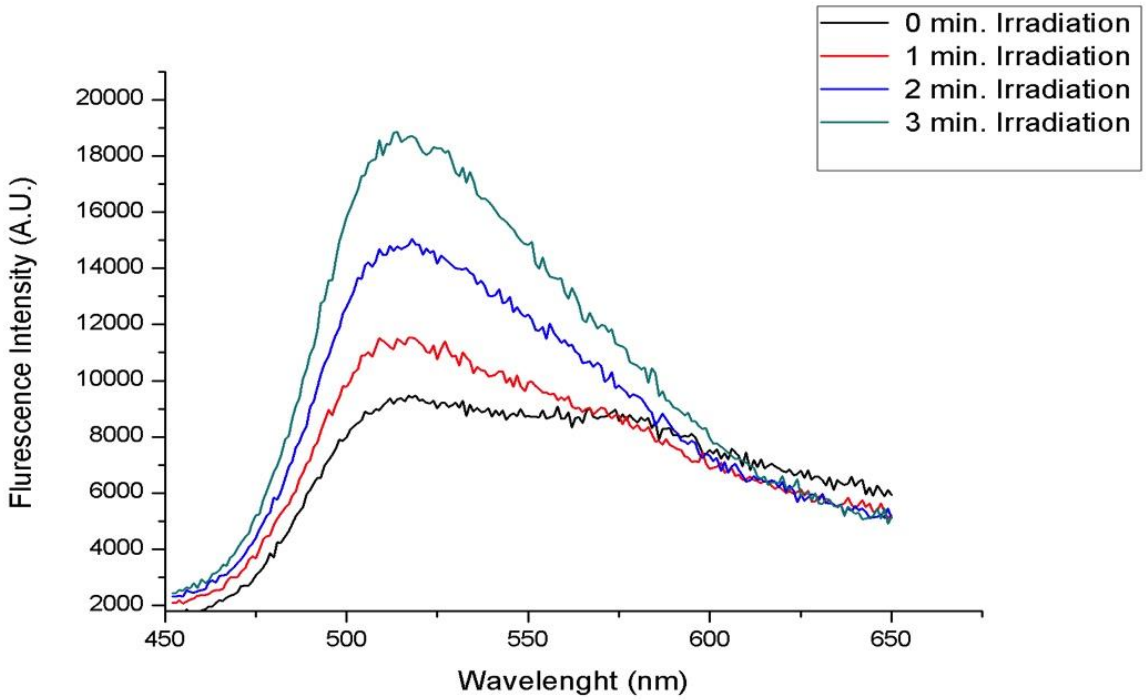

Figure 3-13. Mixing of 150 μM PAG with Lysosensor green in cell free system using different time of irradiation its indicates that the fluorescence intensity of LysoSensor green dye increased as a time of irradiation increased.

3.3.7 Cell Death and Live Cell Imaging

Cell death by **PAG-PEG** was demonstrated by live cell imaging experiment in which, HCT-116 cells were incubated with 50 μM concentration of **PAG-PEG** for 24 h at 37 ^{0}C. Time-lapse images were taken in order to show the process of cell death by PAGs after light irradiation.

Cells were irradiated with (2000 ms) (5.4mW/cm^2) and imaged with confocal microscope (Olympus IX-81) at 1 min intervals for 4 hours by using DIC channel. **Figure 3-14** shows the progressive change in the cells morphology after the generation of photoacid. Loss of the cell adhesion (yellow arrows) is followed by a blebbing – like activity (blue arrows). The integrity of the nuclei in these cells is a sign that chromatin condensation is not occurring; therefore, the process is not apoptotic. After that, the cell was swelling significantly which is characteristic of necrosis (red arrows). This experiment was repeated and applied again with 10μM concentration of **SiN-NH-PAG** incubated with HCT-116 cells for 24 h and showed the same behavior with PAG-PEG (**Figure 3-15**).

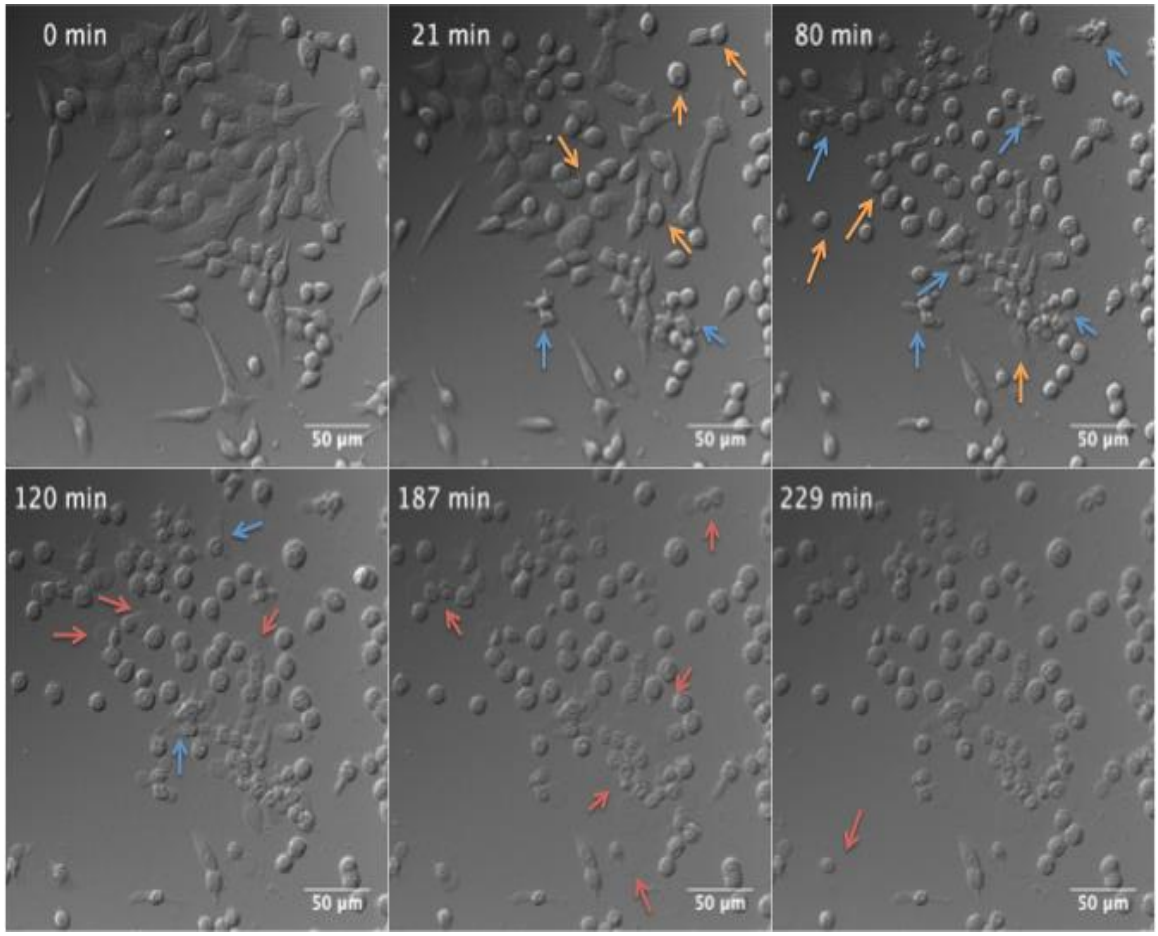

Control

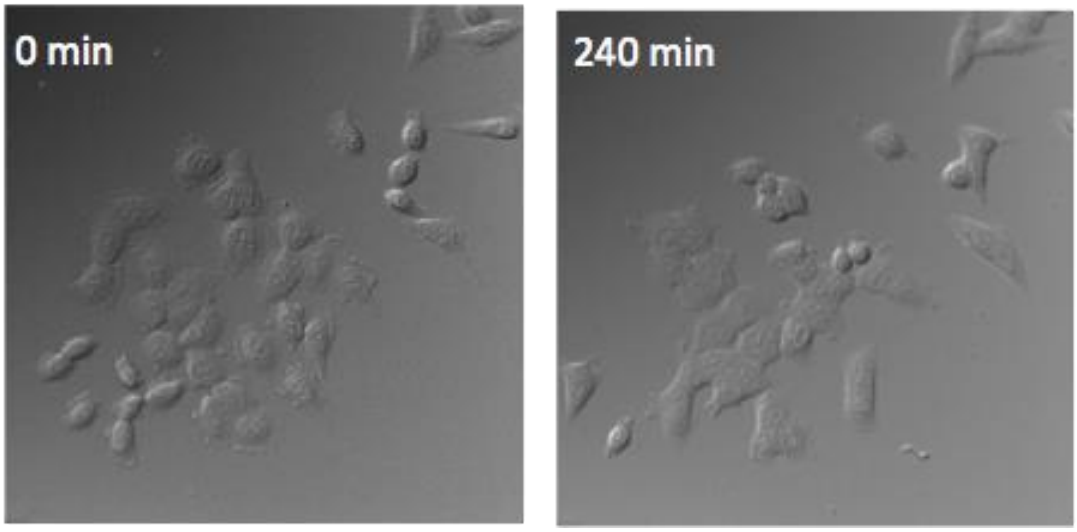

Figure 3-14. HCT-116 Human Colorectal Carcinoma cells incubated for 24 h with PAG-PEG (50 µM). Confocal microscope (Olympus IX-81) at 1 min intervals for 4 hours by using DIC channel. Yellow arrows show loss of cell adhesion, bule arrows show blebbing – like activity, and red arrows cell swelling. Scale bar is 50 µm .

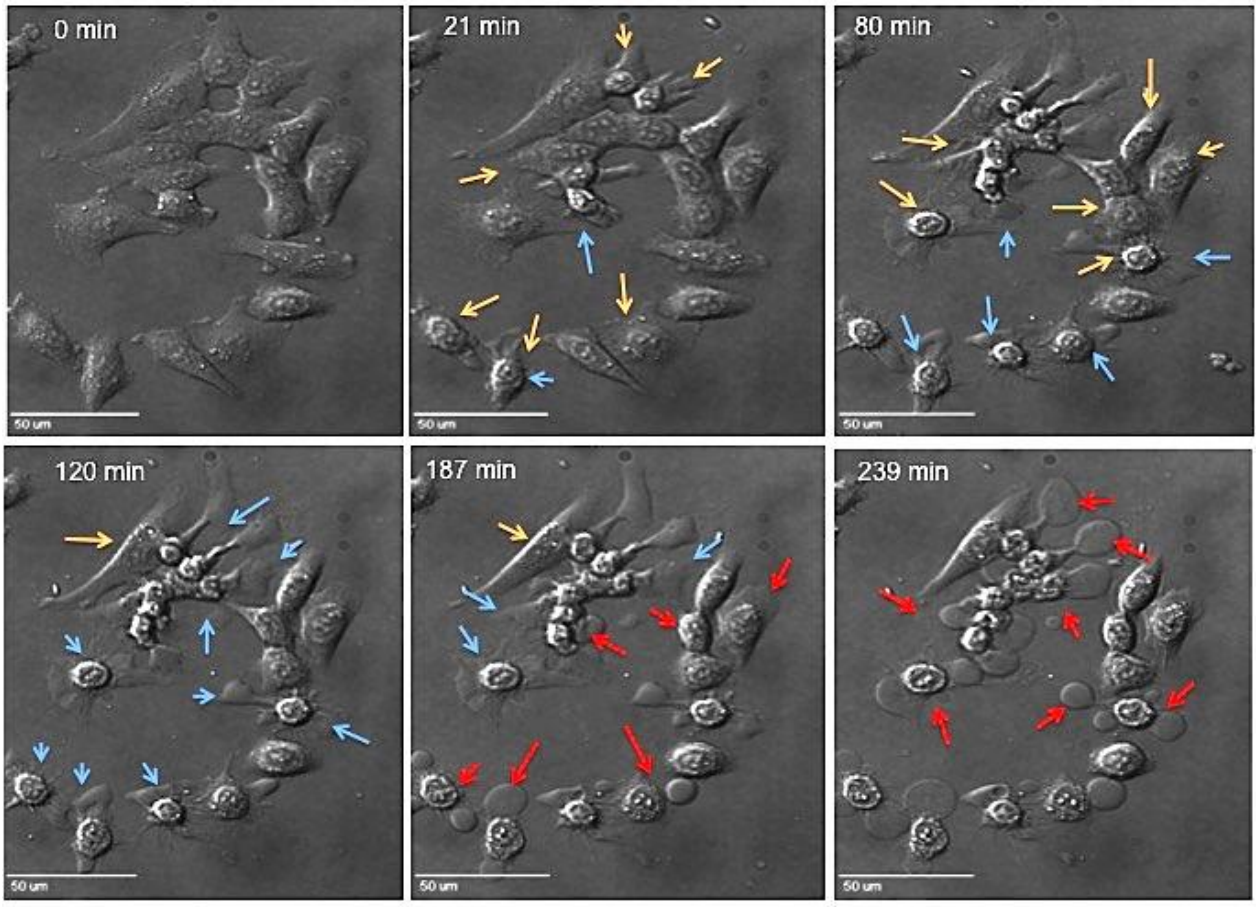

Control

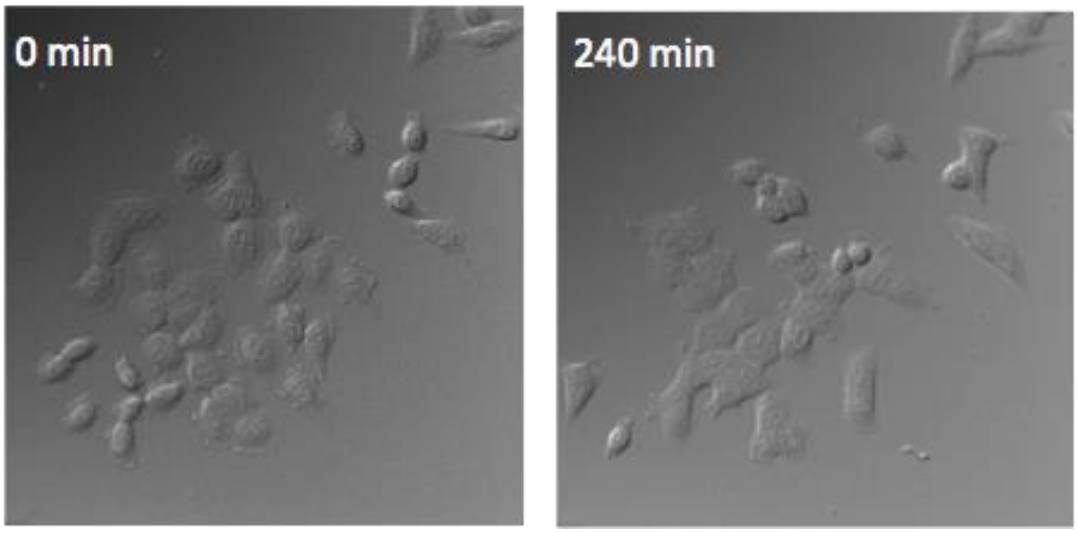

Figure 3-15. HCT-116 Human Colorectal Carcinoma cells incubated for 24 h with SiN-NH-PAG (10 μM). Confocal microscope (Olympus IX-81) at 1 min intervals for 4 hours by using DIC channel. Yellow arrows show loss of cell adhesion, blue arrows show blebbing – like activity, and red arrows cell swelling. Scale bar μm 50.

3.4 Conclusions

The use of photoacid generators to induce cell death by making a grave pH imbalance in cells has been reported. We demonstrated that sulfonium-based PAGs can be used to selectively induce cell death during photoexcitation and this will open the possibility of inducing cell death in an oxygen-independent manner. More exclusively, PAG-PEG and SiN-NH-PAG have induced necrotic cell death via generation of photoacid in the lysosomes in HCT-116 cells. SiN-NH-PAG has showed a greater efficacy at a concentration of 10 μM compared with single molecule species PAG-PEG 50 μM. This assumed to be because the large number of PAG groups present on the nanoparticles. Resulting in a greater number of PAGs present per unit volume of substrate compared to the single molecule species.

H^+ molecules were generated using 1PA since the simplicity of that associated with generating photoacid. Also one photon photoacid generation is more effective process; the excitation source that needed for this process is cheaper and easier to use. 1PA is also an advantage because a large amount of targeted surface mass can be converted within tissue at a faster rate.

CHAPTER 4. SELECTIVE NANO-SENSING APPROACH FOR THE DETERMINATION OF INORGANIC PHOSPHATE IN HUMAN URINE SAMPLES

4.1 Introduction

The level of phosphate metabolites in cells can be used as an indicator of dysfunctions and/or disorders in biological systems.[87] Abnormal levels of phosphate in urine samples are also related to the development of certain types of cancer affecting several organs of the human body, including breast, pancreas, lung and thyroid. As such, the development of assays that can determine phosphate on real-time bases is essential to biochemical studies as well as clinical diagnosis.

Scheme 4-1 illustrates the concept of the proposed sensor, which is based on Fluorescence Resonance Energy Transfer (FRET). The Terbium-Ethylenediaminetetraacetic acid complex $[Tb\text{-}EDTA]^{-1}$ is used as a luminescence donor probe. Gold nanoparticles (Au NPs) capped with Cetyltrimethylammonium bromide (CTAB) are used as acceptors with positive charges on the surface. Hydrophilic and electrostatic interactions between $[Tb\text{-}EDTA]^{-1}$ ions and Au NPs-CTAB provide the close proximity between donor and acceptor that is needed for FRET to occur and quench the luminescence of $Tb[EDTA]^{-1}$ (sensor off). The interaction between phosphate ions and CTAB displaces $Tb[EDTA]^{-1}$ from the proximities of Au NPs to the extent that FRET does not longer occurs (sensor on).

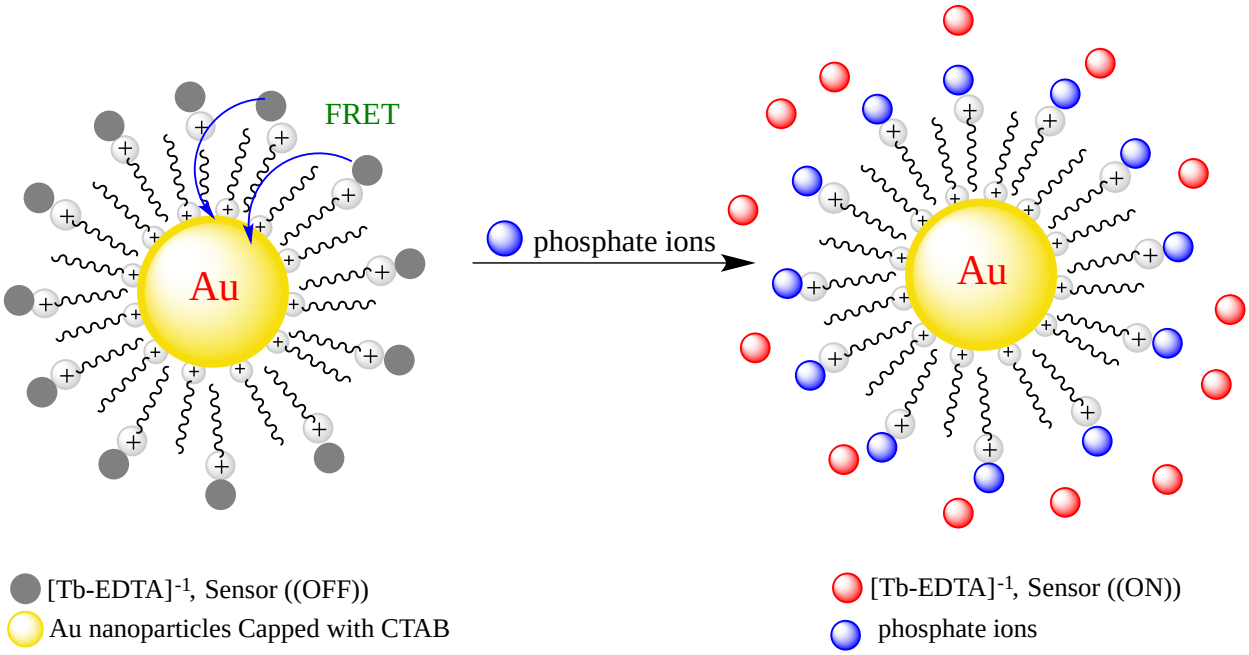

Scheme 4-1. Sensing approach based on Fluorescence Resonance Energy Transfer (FRET) between $[Tb\text{-}EDTA]^{-1}$ and Au NPs followed by chemical displacement of $[Tb\text{-}EDTA]^{-1}$ by phosphate ions at the head of CTAB receptors.

FRET involves a mechanism in which the energy of the emitting donor will transfer via non-radiative dipole-dipole interaction to an acceptor. The efficiency of FRET is inversely proportional to the sixth power of the distance (R^{-6}) between donor (fluorophore) and the acceptor (quencher) within 10-100 Å. During the process of energy transfer, the proximity between donor and acceptor reduces the quantum yield of the donor's emission. When the distance increases, the intensity of emission is effectively restored.[88] This technique is often used in biochemistry and structural biology to study macromolecular complexes of DNA, RNA, and proteins.[89-90] Au NPs have demonstrated excellent potential as bio-sensing platforms for a wide range of applications varying from chemical to biological samples.[91-95] This popularity is partially due to the possibility of functionalizing the surface of Au NPs with peptides, proteins and antibodies that provide the required specificity toward cellular targets in complex biological matrixes. The achievement of additional selectivity is possible by using fluorescent dyes

optically active in the near-infrared, a wavelength region with relatively lower spectral interference from biological matrixes.[96,97]

Our approach is based on time-resolution techniques. The long-lived luminescence of lanthanide ions (particularly Tb^{3+} and Eu^{3+}), which occurs in the milliseconds time domain, makes possible to time-discriminate against short-lived background fluorescence and scattered excitation light with rather simple, off-the-shelve, commercial instrumentation. Since their emission results from shielded electronic transitions (f-orbital manifold), the luminescence intensity of Eu^{3+} and Tb^{3+} has shown less susceptibility to oxygen quenching than traditional fluorescent dyes.[98-101]

CTAB is an amine based cationic quaternary surfactant often used to avoid aggregation of Au NPs in aqueous solution via electrostatic repulsion. CTAB molecules show strong chemical affinity for phosphate ions that makes them selective receptors in the presence of other inorganic ions.[102]

Although individual elements of our approach have been anticipated and implemented previously, the optimal combination of these features has not been realized and the techniques have generally not been practical enough for straightforward implementation. The main significant aspect of our proposition is the practical, smooth way we are integrating all these features together.

4.2 Materials and Methods

All the reagents and solvents were purchased from different commercial providers and used without further purification. Sodium phosphate (Na_3PO_4), sodium acetate, sodium fluoride, and sodium sulfite were obtained from Aldrich. Sodium carbonate, urea, creatinine, sodium nitrate, sodium hydroxide, and sodium iodide were obtained form Alfa-Aesar. Nanopure water was also used throughout obtained from a Barnstead Nanopure Infinity water purifier.

4.2.1 Instrumentation

Excitation and emission spectra were recorded with a commercial spectrofluorimeter (FluoroMax-P from Horiba Jobin-Yvon) equipped with a continuous 100 W pulsed xenon lamp with broadband illumination from 200 to 1100 nm. The excitation and emission monochromators had the same reciprocal linear dispersion (4.2 $nm \cdot mm^{-1}$) and accuracy (±0.5 nm with 0.3 nm resolution). Both diffraction gratings had the same number of grooves per unit length (1200 $grooves \cdot mm^{-1}$) and were blazed at 330 nm (excitation) and 500 nm (emission). A photomultiplier tube (Hamamatsu, model R928) with spectral response from 185 to 650 nm was used for fluorescence detection operating at room temperature in the photon- counting mode. Commercial software (DataMax) was used to computer-control the instrument. Measurements were made by pouring un-degassed liquid solutions into micro-quartz cuvettes (1 cm path length x 2 mm width) that held a maximum volume of 400 μL. Fluorescence was collected at 90° from excitation using appropriate cutoff filters to reject straight-light and second order emission.

4.2.2 Synthesis of Gold Nanoparticles (Au NPs) capped with CTAB

The synthesis of the Au NPs was carried out via a method similar to the one reported by Nikoobakht. [103] The modifications implemented in these studies are shown in **scheme 4-2**. All glassware was washed with aqua-regia (1:3 HNO_3/HCl v/v) to remove the presence of any gold crystals. A seed solution was prepared with 1mL of 2.0M CTAB and 1mL of nanopure water. In order to keep the CTAB from precipitating out, the solution was heated to about 35^oC. 18uL of 0.029M $HAuCl_4$ was added to the CTAB aqueous solution, which became yellow in color and was mixed slowly. 120uL of ice-cold 0.010 M $NaBH_4$ was then added to the mixture causing the color to turn brown. Prior to use, the seed solution was allowed to mix for ½ hour.

Growth solutions were prepared in 10mL beakers by adding 5mL of nanopure water and 5mL of 2.0 M CTAB. The growth solutions were mixed and heated to about 35^oC to avoid CTAB precipitation. 180 uL of 0.029M $HAuCl_4$ were added and stirred until the solution appeared homogenous. 60, 70, or 80uL of 0.0788M Ascorbic Acid were then added to different growth solutions to test which concentration of Ascorbic Acid would be optimal. 20, 30 or 40uL of seed solution were transferred to the different growth solutions to find out the optimal volume of seed solution. The resulting mixtures were agitated for several seconds to disperse the seed evenly and then allowed to sit for about 10 minutes during which the color changed from clear to deep purple. After 10 minutes the solutions were removed from the heat source and kept at room temperature until further use.

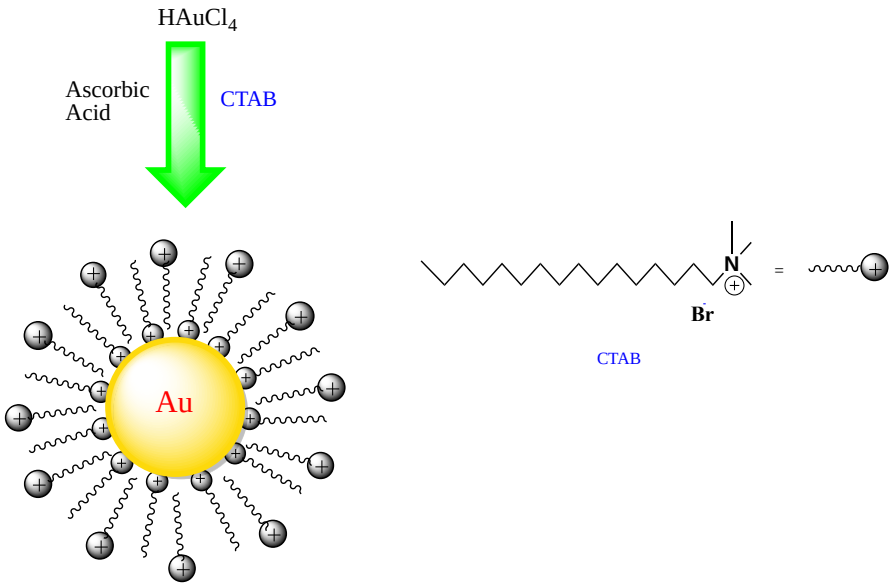

Scheme 4-2. Synthesis of Gold nanoparticles in CTAB micelles.

4.2.3 Characterization of Gold Nanoparticles (Au NPs)

4.2.3.1 UV-vis Characterization

The synthesized Au NPs were characterized via absorbance spectroscopy using a Cary 50 spectrophotometer equipped with a 75-W pulsed Xenon lamp (spectral radiance of 190-1100nm), a monochromator (fixed optical band-pass of 1.5nm), a beam-splitter and two silicon photo-diode detectors.

4.2.3.2 Particle Size

The particle size distribution of Au NPs was obtained via light scattering with a Zetasizer Nano ZS9 instrument purchased from Malvern .

4.2.4 Preparation of $[Tb\text{-}EDTA]^{-1}$ (probe)

Stock solutions of Tb^{3+} and $EDTA^{-4}$ in HEPES buffer pH ≈7.4 were prepared at a concentration of 10^{-3} M. In order to obtain the maximum luminescence signal from the $[Tb\text{-}EDTA]^{-1}$ complex, various mixtures with the following concentration ratios of 10^{-3} M Tb^{3+} and 10^{-3} M $EDTA^{4-}$ were prepared: 1:0, 1:0.25, 1:0.5, 1:1, 1:1.5. The resulting mixtures were shaken for 5 minutes prior luminescence measurements. After selecting the best Tb^{3+}-$EDTA^{4-}$ ratio, serial dilutions were made to reach final Tb^{3+} concentrations equal to 10^{-4}, 10^{-5} and 10^{-6} M.

4.2.5 Sensor Preparation

350μL of Au NPs-CTAB stock solution (optical density = 0.74 OD) were added to 150μL of a 10^{-5} M $[Tb\text{-}EDTA]^{-1}$ solution. After 5 minutes of mechanical shaking, the mixture was ready to use for phosphate sensing.

4.2.6 Interference studies

The following chemical species were tested for possible interference at the 75x 10^{-5} M concentration: PO_4^{-3}, NO_3^- , NO_2^- , CH_3COO^- , OH^- , CO_3^{2-} , Cl^- , SO_3^{-2}, F^-, I^-, Urea, and Creatinine.

4.2.7 Urine Analysis

Urine samples from healthy, non-smoking volunteers were used as representative clinical samples. Urine samples were prepared following a previously reported procedure [95] and used within one hour of sample collection. After two filtration cycles with filter paper Whatman #50,

the concentration of phosphate ions in each sample was determined via the multiple standards addition method.

4.3 Results and Discussion

4.3.1 Sensing Mechanism

As shown in **Figure 4.1**, the absorption spectrum of Au NPs-CTAB displays a strong Surface Plasmon Resonance (SPR) absorption band with maximum wavelength at approximately 541 nm. The overlapping of this absorption band with the luminescence spectrum of $[Tb\text{-}EDTA]^{-1}$ is an essential condition to promote FRET between the donor and the acceptor. Hydrophilic and electrostatic interactions between $[Tb\text{-}EDTA]^{-1}$ and Au N-CTAB provide the close proximity that is needed for FRET to occur and quench the luminescence of $Tb[EDTA]^{-1}$ (sensor off).

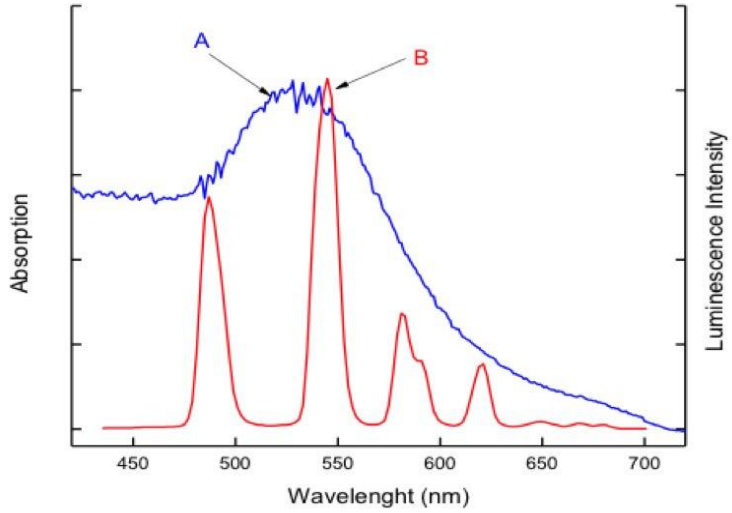

Figure 4-1. (A) UV-vis absorption spectrum of Au NPs-CTAB; and (B) luminescence emission spectrum of Tb-EDTA.

The interaction between phosphate ions and the CTAB displaces $Tb[EDTA]^{-1}$ from the proximities of Au NPs to the extent that FRET does not longer occurs. As a result, the luminescence signal of the donor increases (sensor on) as shown in **Figure 4.2.**

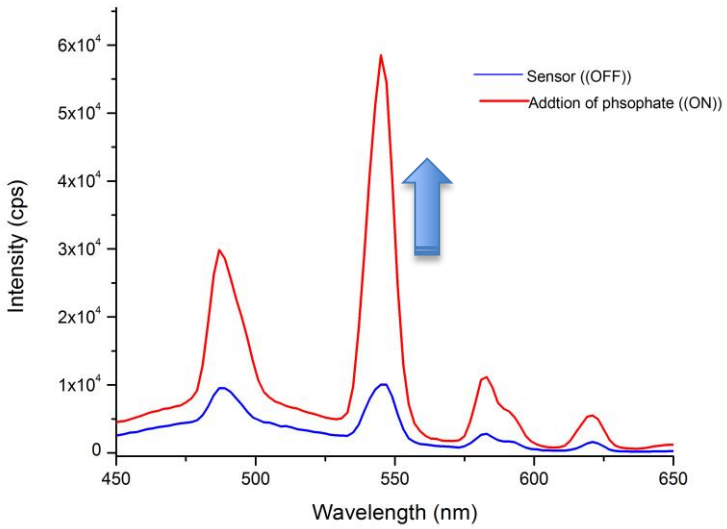

Figure 4-2. Luminescence signal (blue) and after (red) the addition of 75 × 10^{-5}M of inorganic phosphate to the optimized sensor using Ex/Em 240/545 nm, band pass 15/5 nm, Tg 9.00 ms and Td 0.01 ms

4.3.2 Synthesis of gold nanoparticles in CTAB micelles

The synthesis of Au NPs was monitored via UV-vis absorption spectroscopy. The optical density of the SPR band at 541nm reached maximum intensity with 70uL of Ascorbic Acid and 30uL of seed solution. Upon addition of 70uL or more of ascorbic acid, the solution changed colors from yellow to colorless indicating that the growth solution had been completely reduced. Volumes of Ascorbic Acid lower than 70uL caused the solution to remain yellow indicating that it was not fully reduced. Volumes of seed solution lower than 30uL yielded nanoparticles with the desired dimensions – i.e. SPR maximum wavelength ~ 541nm - but a lower concentration than the optimum concentration at maximum optical density. Volumes of seed solution higher

than 30uL created smaller spheres that did not absorb at the desired wavelength range. The excess of CTAB and reactants was removed from the final solution via centrifugation. It was observed that three centrifugation cycles at 13,000 rpms for 30 minutes allowed the sensor to function while still keeping the nanoparticles from aggregating.

4.3.3 Particles size of Gold nanoparticles

Figure 4-3 shows the particle size distribution obtained from three light scattering measurements of three Au NPs-CTAB solutions produced by the synthetic protocol described previously. The size distribution of Au NPs ranges from 10 - 70 nm with an average mean size of approximately 25 nm. This average size is consistent with the maximum wavelength of the SPR absorption band at 541nm[104].

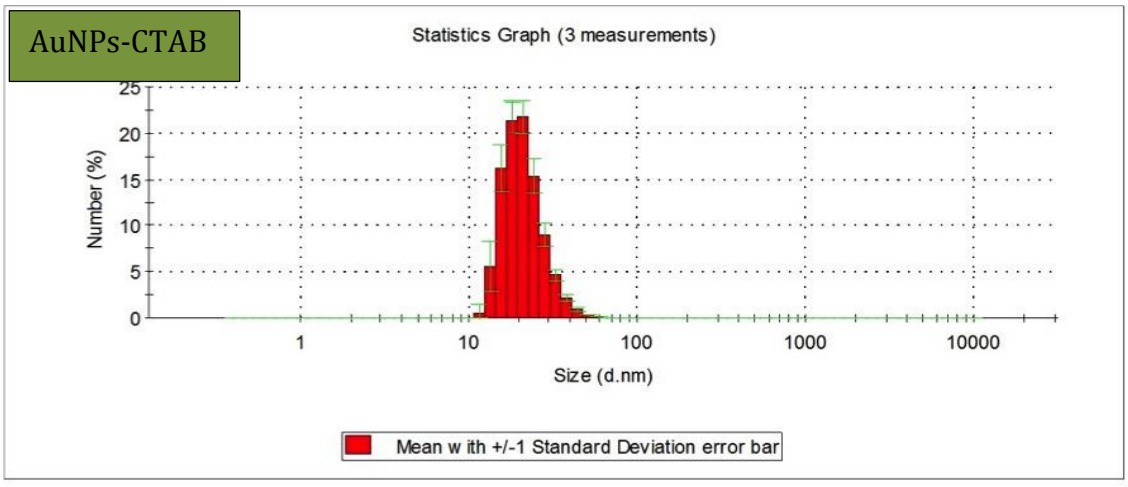

Figure 4-3. Number-averaged particle size distribution of Au NPs-CTAB.

4.3.4 Optimization Studies

4.3.4.1 Optimization of Signal to Background Ratio for Analytical Use

The coordination of water molecules to Tb^{3+} quenches the luminescence signal of the lanthanide ion. The maximum luminescence signal is obtained when the ligand $EDTA^{4-}$ removes all the water molecules from the coordination sphere of Tb^{3+} [105]. As shown in Figure 4-4A, the maximum luminescence signal is obtained for a Tb^{3+}-$EDTA^{4-}$ molar ratio of 1:1. At this molar ratio and upon excitation at 235nm, $[Tb\text{-}EDTA]^{-1}$ provides a spectral signature with an acceptable signal-to-background (S/B) ratio for analytical use. Optimization of instrumental parameter for best S/B ratio resulted in 20 excitation pulses per data point, a 15/5nm excitation/ emission band-pass, and delay (T_d) and gate (T_g) times of 0.01 and 9ms, respectively.

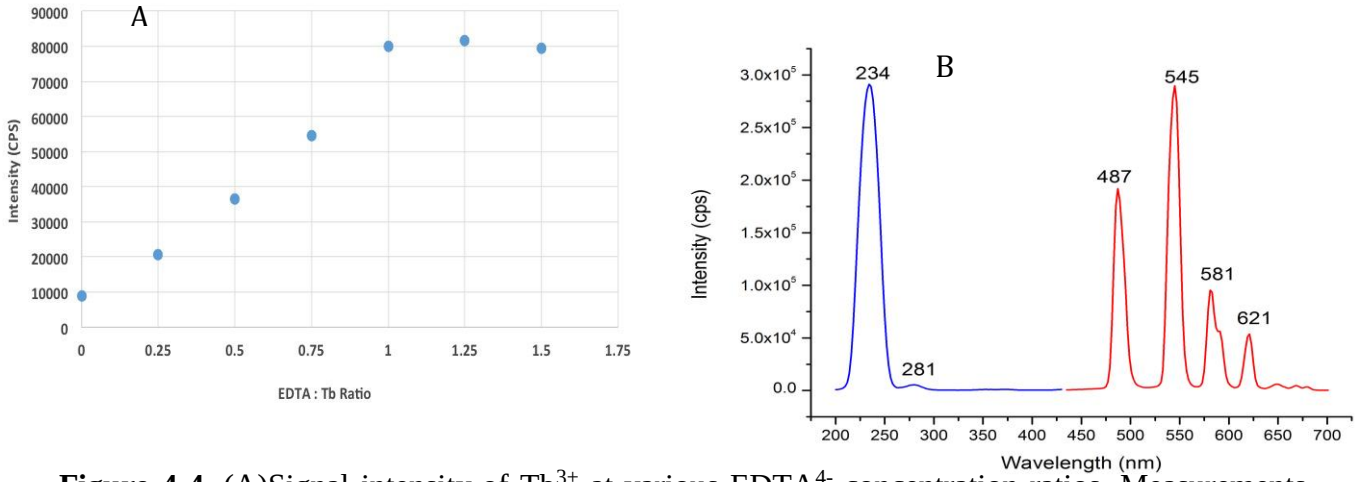

Figure 4-4. (A)Signal intensity of Tb^{3+} at various $EDTA^{4-}$ concentration ratios. Measurements were made with a 10^{-5}M Tb^{3+} solution in HEPES buffer at pH 7.5. (B) Time-resolved spectra of 10^{-3}M of Tb-EDTA in HEPES buffer. Ex/Em 234/545 nm, band pass 15/5 nm, delay (T_d) 0.01 ms and gate (T_g) times 9 ms, respectively.

4.3.4.2 Optimization of probe displacement time

Figure 4-5 shows the signal intensity of Au NPs – CTAB – $[Tb\text{-}EDTA]^{-1}$as a function of shaking time after adding phosphate ions to the sensing solution. All solutions were shaken at 1,200rpm. For a 10^{-5}M $Tb\text{-}EDTA^{-1}$ solution and within the concentration range of phosphate ions tested (25-75×10^{-5} M), the time it took to reach the maximum signal depended on the concentration of phosphate ions. The shortest time (3 min) was obtained with the highest phosphate ion concentration (75×10^{-5}M). In order to provide enough time for the complete displacement of $[Tb\text{-}EDTA]^{-1}$, all further measurements were carried out after 10 min of shaking time.

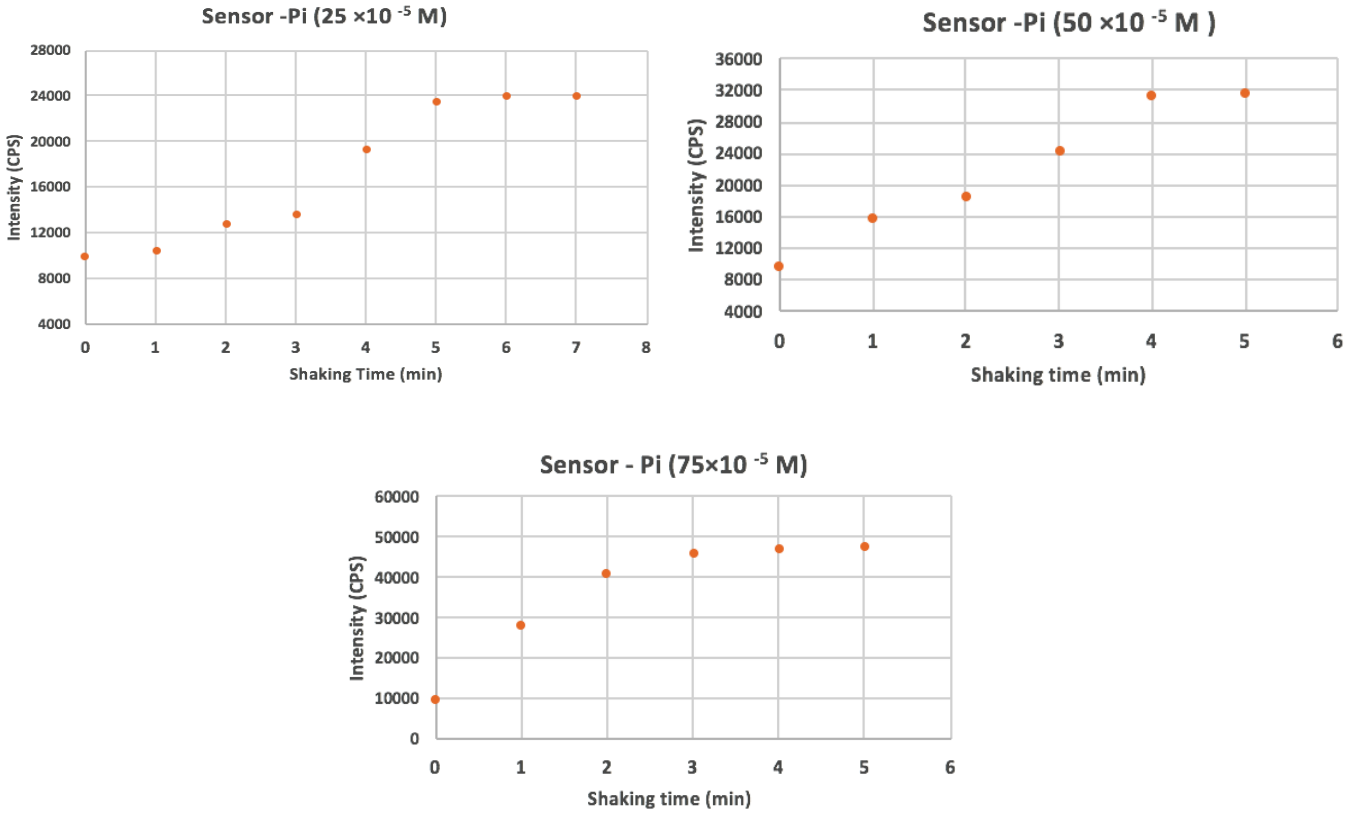

Figure 4-5. Signal intensity of Au NPs-CTAB-[10^{-5}M $[Tb\text{-}EDTA]^{-1}$ as a function of shaking time.

4.3.5 Interference Studies

Potential matrix interference was investigated by comparing the response of the senor in the absence and the presence of several chemical species commonly found in urine samples. Their concentrations were adjusted to mimic the natural composition of human urine. The obtained results are shown in Figure 4-6. With the exception of the phosphate ion, all the other species provided signals with statistically equivalent intensities to the one of the control signal ($P = 95\%$; $N_1 = N_2 = 3$). The obtained results indicate that the investigated ions do not release $[Tb\text{-}EDTA]^{-1}$ from the positive charges of the CTAB receptors into the bulk of the sensing solution. This is probably due to a lower chemical affinity between the potential interference and the CTAB receptor. When compared to the $Tb\text{-}EDTA^{-1}$ complex and the studied interference, the higher affinity of the phosphate ion for the CTAB receptors could be attributed to tetrahedral shape of the predominant phosphate species in solution (HPO_4^{2-}), which makes its negative charge more polarizable than the other investigated anions. [102,106,107]

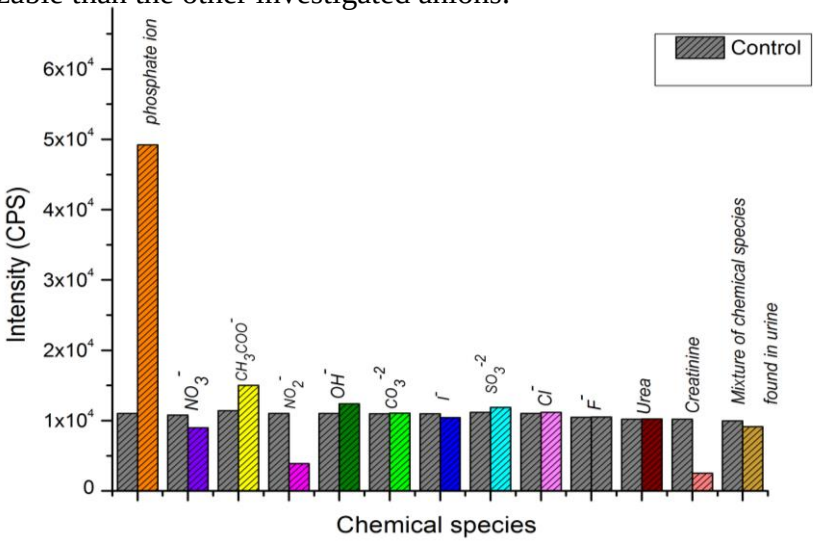

Figure 4-6. Comparison of luminescence intensities in the absence and the presence of potential interference at the concentrations commonly found in urine samples, namely 10^{-4}M for all the ions with the exception of urea (10^{-3}M). All measurements were made with a $75x01^{-5}$M sensing solution

4.3.6 Analytical Figures of Merit

A calibration curve was built in HEPES buffer pH 7.5 with external standards containing different concentrations of phosphate ions (PO_4^{-3}) and fixed concentrations of creatinine, urea, NO_3^-, Cl^-, F^-, SO_3^{-2}, CO_3^{-2}, OH^- and I^-. The concentrations of concomitants mimicked those in real urine samples, namely10^{-4}M for all the ions with the exception of urea (10^{-3}M). The direct correlation that was observed between signal intensity and the phosphate concentration is shown in **Figure 4-7**. Linear regression via the least squares method provided a linear dynamic range (R^2 = 0.9894) ranging from 6.3x10^{-6}M to 7.5×10^{-4}M. The limit of detection (1.8 uM) was calculated as $3S_B/m$; where S_B is the standard deviation of 16 blank measurements and m is the slope of the calibration curve.

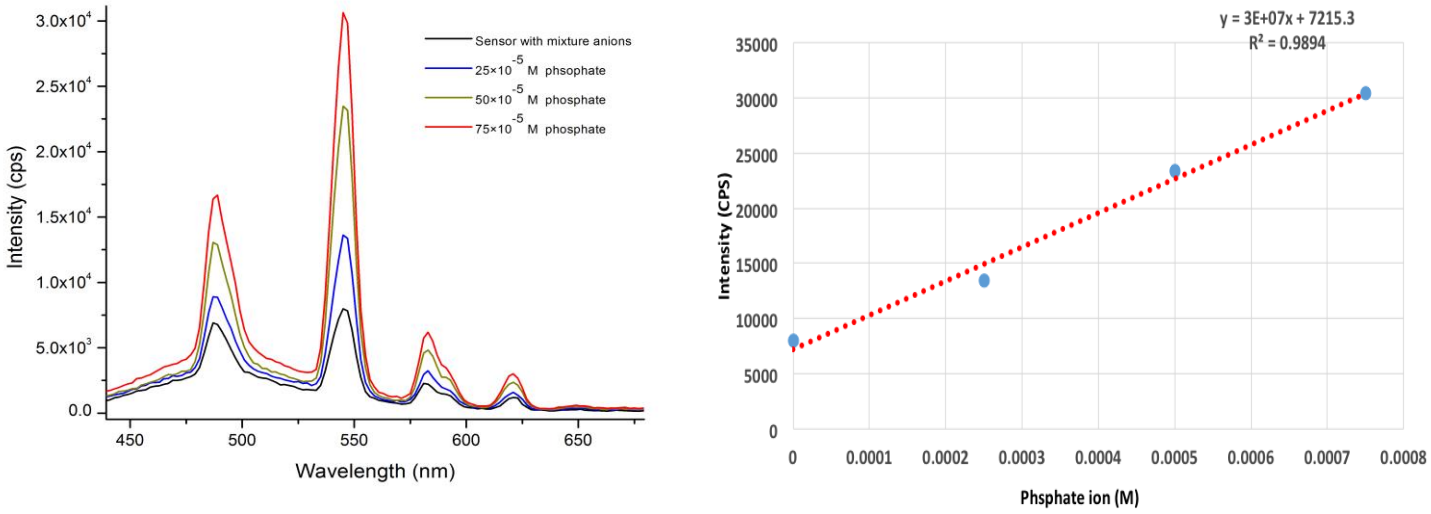

Figure 4-7. Luminescence spectra (left) and signal intensities (right) at different phosphate concentrations.

4.3.7 Urine Analysis

Urine analysis was carried out via the multiple standard additions method. Urine samples were diluted 70 times to reach a final volume of 500uL. All measurements were made in HEPES buffer pH ≈ 7.5. Multiple standard additions were carried out with µL volumes of a 0.025M (PO_4^{-3}) standard solution. **Figure 4-8** shows the multiple standard additions plot. The best linear fit was obtained with the least squares method. Comparison of the linear equations obtained from the calibration curve and the multiple standard additions plot shows the same slope ($3x10^7$). This is a strong indication of the lack of chemical interference in the urine sample. The concentration of phosphate found in the urine sample (399 ± 24 mgL^{-1}) was within the reported values of urine samples collected from healthy individuals.

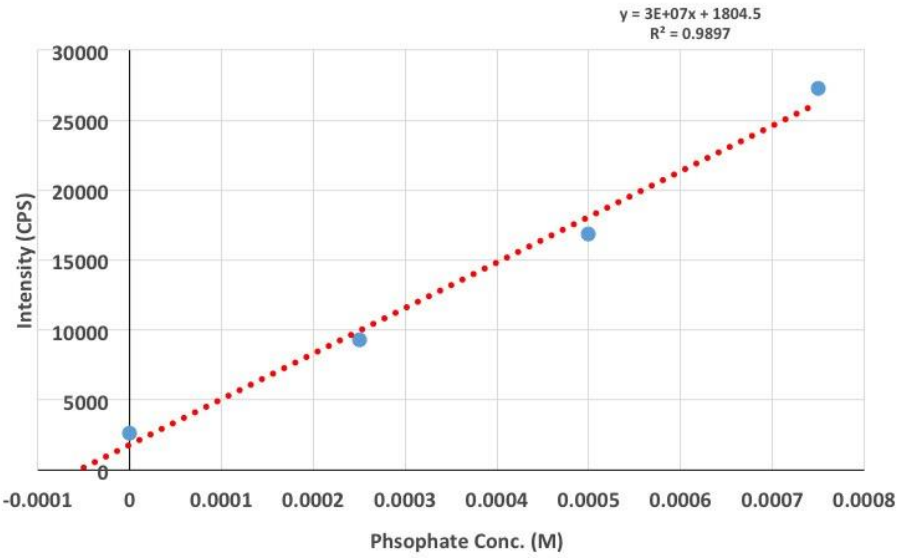

Figure 4-8. Standard addition calibration plot for the determination inorganic phosphate in human urine.

4.4 Conclusion

A novel sensor for inorganic phosphate in urine samples was developed that takes advantage of the FRET that occurs between $[Tb\text{-}EDTA]^{-1}$ (donor) and Au NPs capped with CTAB acceptors. The limit of detection (1.8uM) was within the concentration range of sensing approaches reported previously. The main advantages of the proposed sensor relate to its selectivity, simplicity of operation and analysis time. The new sensor presented no interference from chemical species commonly found in urine samples, including creatinine, urea, NO_3^-, NO_2^-, OH^-, CO_3^{-2}, SO_3^{-2}, Cl^-, F^-, CH_3COO^-**,** and I^-. The simplicity of analysis provides an approach well-suited for "real-time" monitoring of phosphate ions. Analysis time is made possible within approximately 10 min per sample.

CHAPTER 5. FUTURE WORK

Future applications for chapter two and three can be focused on encapsulating silica nanoparticles with 2PA imaging probes and PAG and functionalized the surface of silica nanoparticles with site specific tumor cell like RGD peptide or folic acid and applying this agent on live animal experiment. Furthermore, using of a windows chamber results better comparison by tracking the cancer progression on the individual model. The PDT agent can be irradiated through windows chamber and treatment efficiency can be estimated by measuring the tumor sizes.

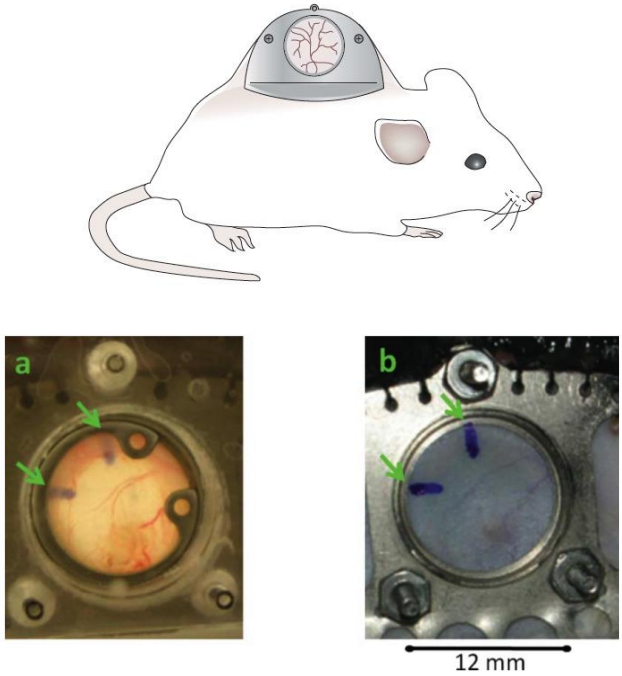

Figure 5-1. Introducing of the window chamber on the skin of the mouse.[108]

Future work can also be focus on the conjugation of synthesized PAG-NH-Boc **Figure 5-1** with proper polymer. This polymer can also be conjugated with RGD peptide and 2PA imaging probes. RGD peptides have been well known for their selective binding properties with vasculatures of tumor cells. 2PA imaging probes can be used due to the deep penetration of 2PA excitation. This way, the therapeutic agent (PAG) can be tracked by the imaging probes.

RGD and PAG-NH-Boc can be introduced to the polymer by applying N-hydroxyscuccinimide on one of the monomers termini to react with the primary amine group PAG and RGD (a lysine residue). As a result, polymer with 2PA fluorescence probes and PAG agents with RGD peptide are proposed for live animal experiment work.

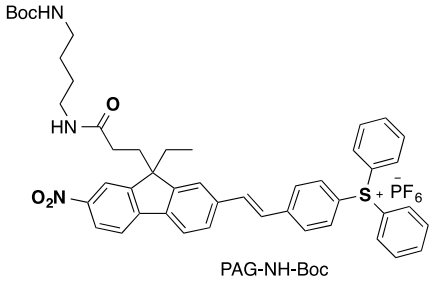

PAG-NH-Boc

Figure 5-2. Structure of PAG-NH-Boc.

PAG 9 can also be conjugated with RGD peptide by introducing N-hydroxyscuccinimide on the PAG 9 and coupled with RGD as shown in **scheme 4-1**

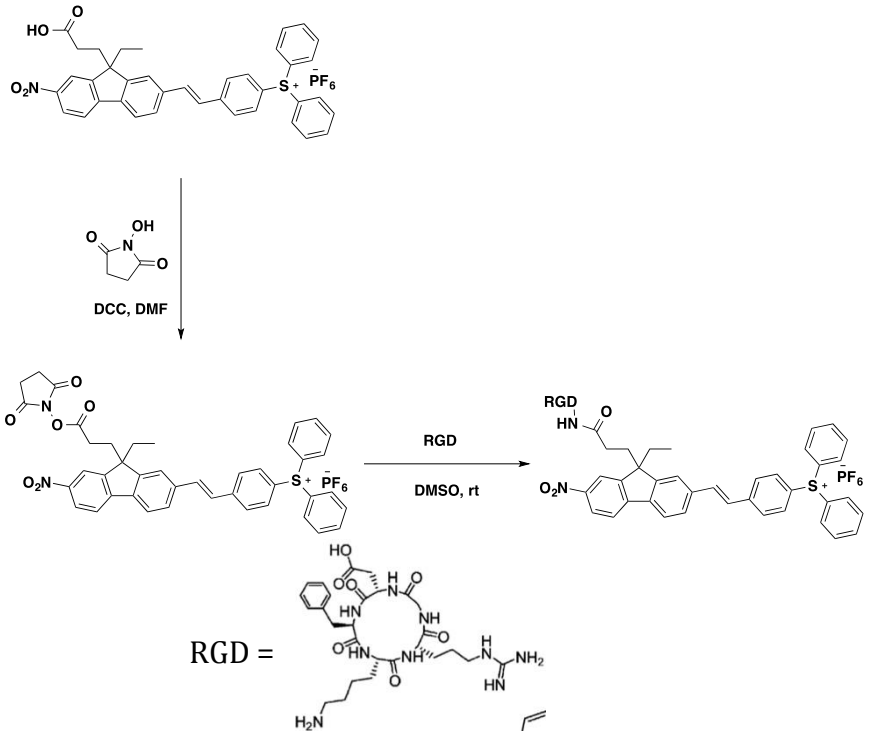

Scheme 5-1. PAG 9 conjugated with RGD peptide.

Future work on the phosphate sensor (chapter 4) will be focused on developing an antenna capable to enhance the luminescence emission of the $[Tb\text{-}EDTA]^{-1}$ probe. The enhancement of the luminescence signal will allow the detection of lower $[Tb\text{-}EDTA]^{-1}$ concentrations in the bulk of the sensing solution. A lower range of detectable concentrations of released $[Tb\text{-}EDTA]^{-1}$ is expected to correlate to lower concentrations of phosphate ions and, therefore, better limits of detection.

APPENDIX CHAPTER TWO

^{1}H NMR of 1

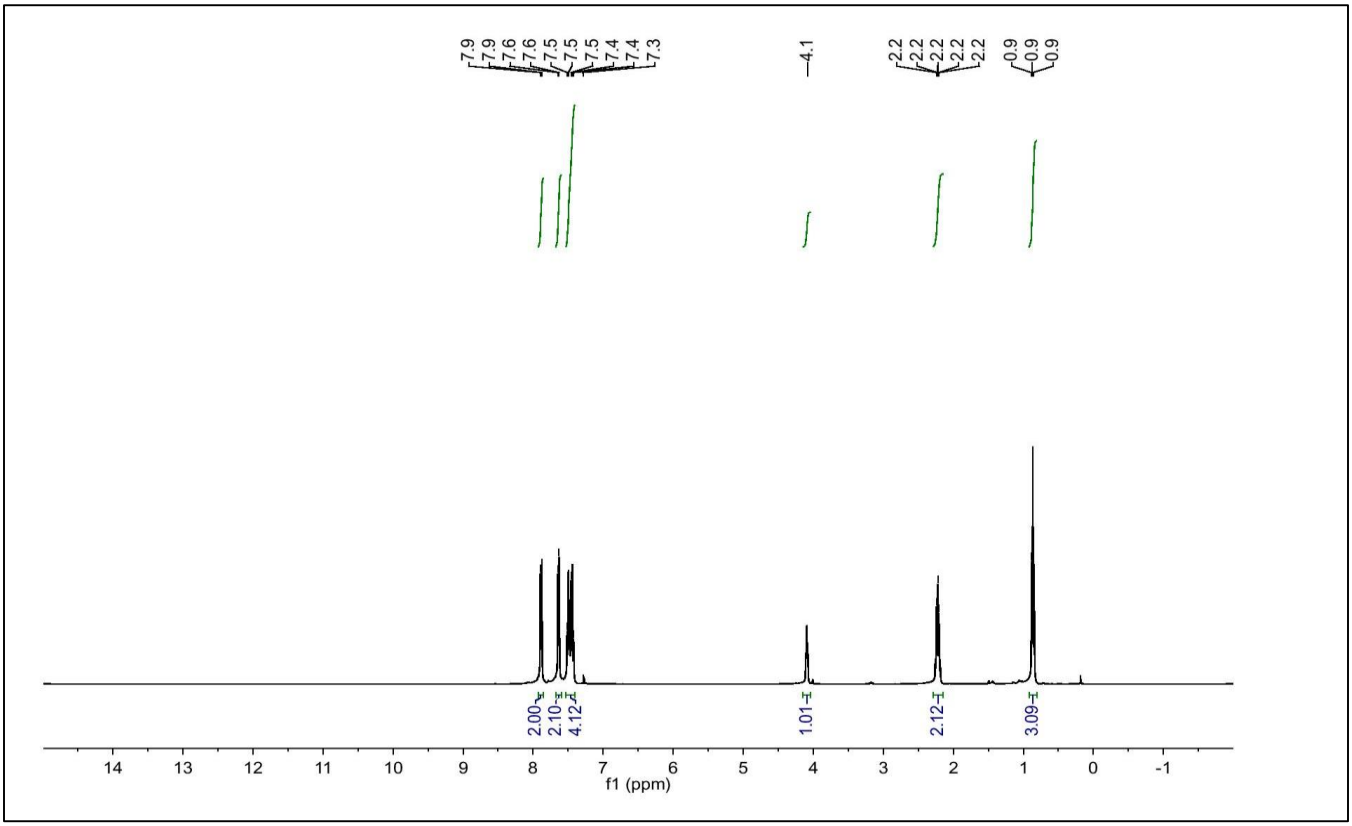
7.9
7.9
7.6
7.6
7.5
7.5
7.5
7.4
7.4
7.3
4.1
2.2
2.2
2.2
2.2
2.2
0.9
0.9
0.9
2.00
2.10
4.12
1.01
2.12
3.09
14
13
12
11
10
9
8
7
6
5
4
3
2
1
0
-1
f1 (ppm)

^{13}C NMR of 1

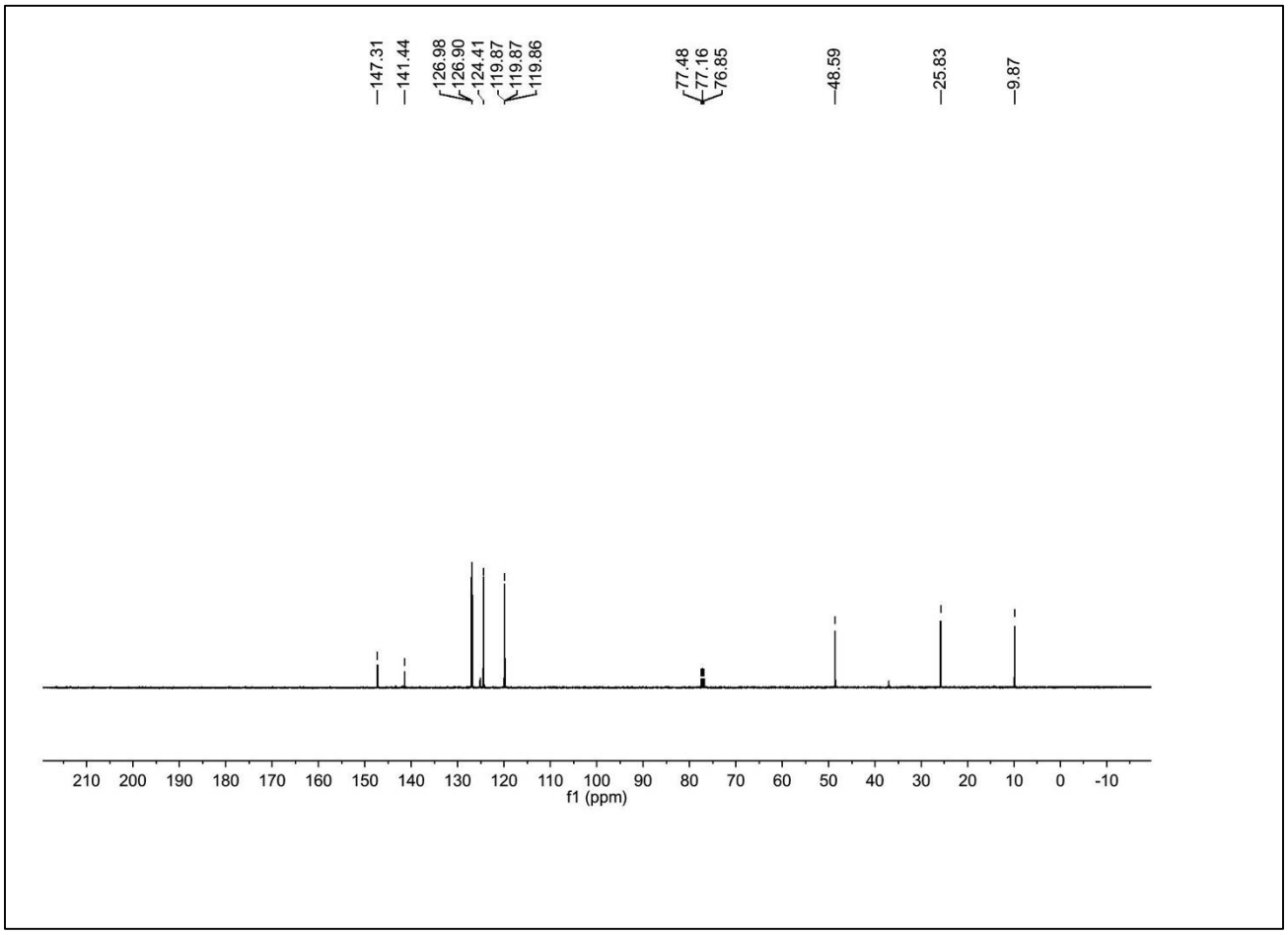
147.31
141.44
126.98
126.90
124.41
119.87
119.87
119.86
77.48
77.16
76.85
48.59
25.83
9.87
210 200 190 180 170 160 150 140 130 120 110 100 90 80 70 60 50 40 30 20 10 0 -10
f1 (ppm)

^{1}H NMR of 2

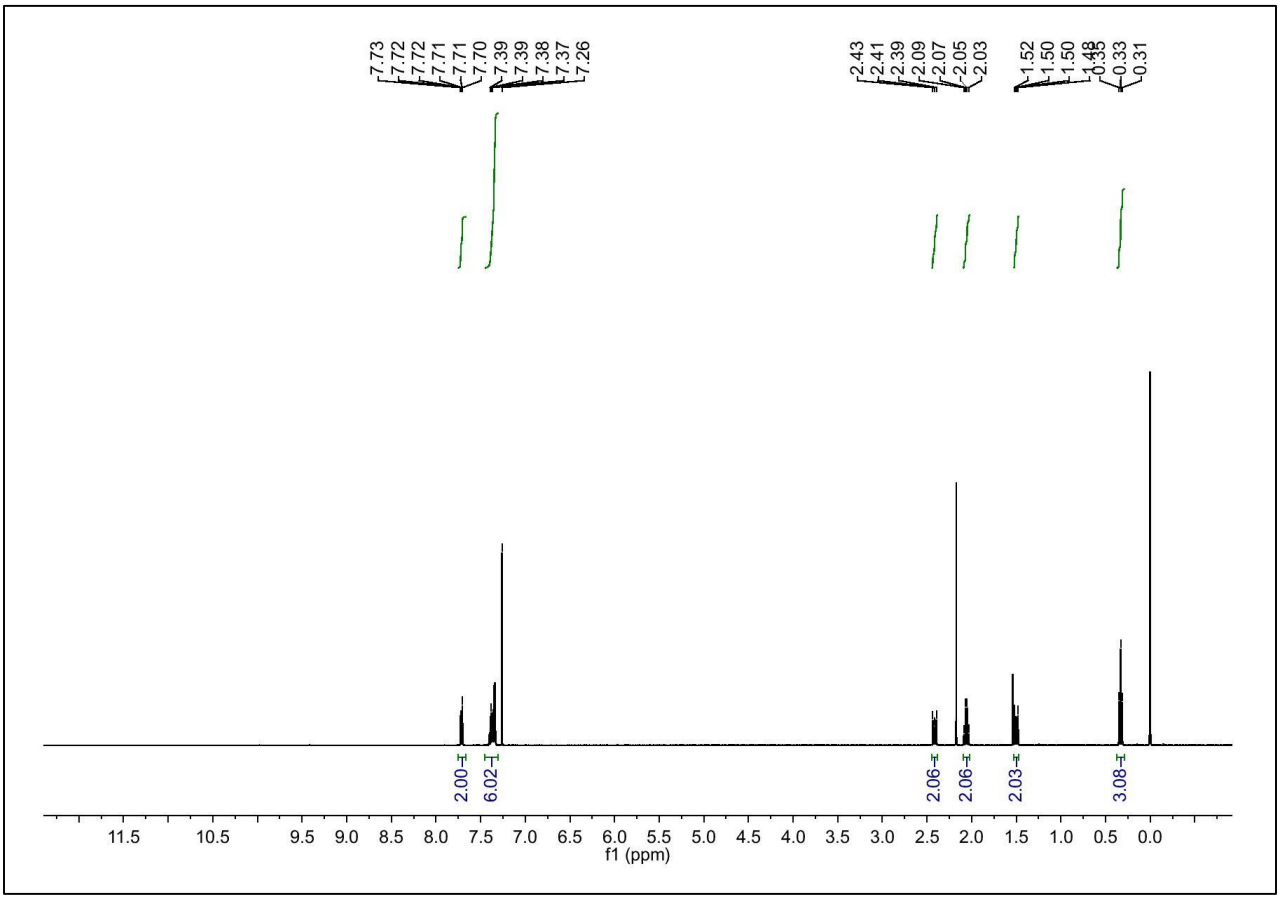
7.73
7.72
7.72
7.71
7.71
7.70
7.39
7.39
7.38
7.37
7.26
2.43
2.41
2.39
2.09
2.07
2.05
2.03
1.52
1.50
1.50
1.48
0.35
0.33
0.31
2.00
6.02
2.06
2.06
2.03
3.08
11.5
10.5
9.5
9.0
8.5
8.0
7.5
7.0
6.5
6.0
5.5
5.0
4.5
4.0
3.5
3.0
2.5
2.0
1.5
1.0
0.5
0.0
f1 (ppm)

^{13}C NMR of 2

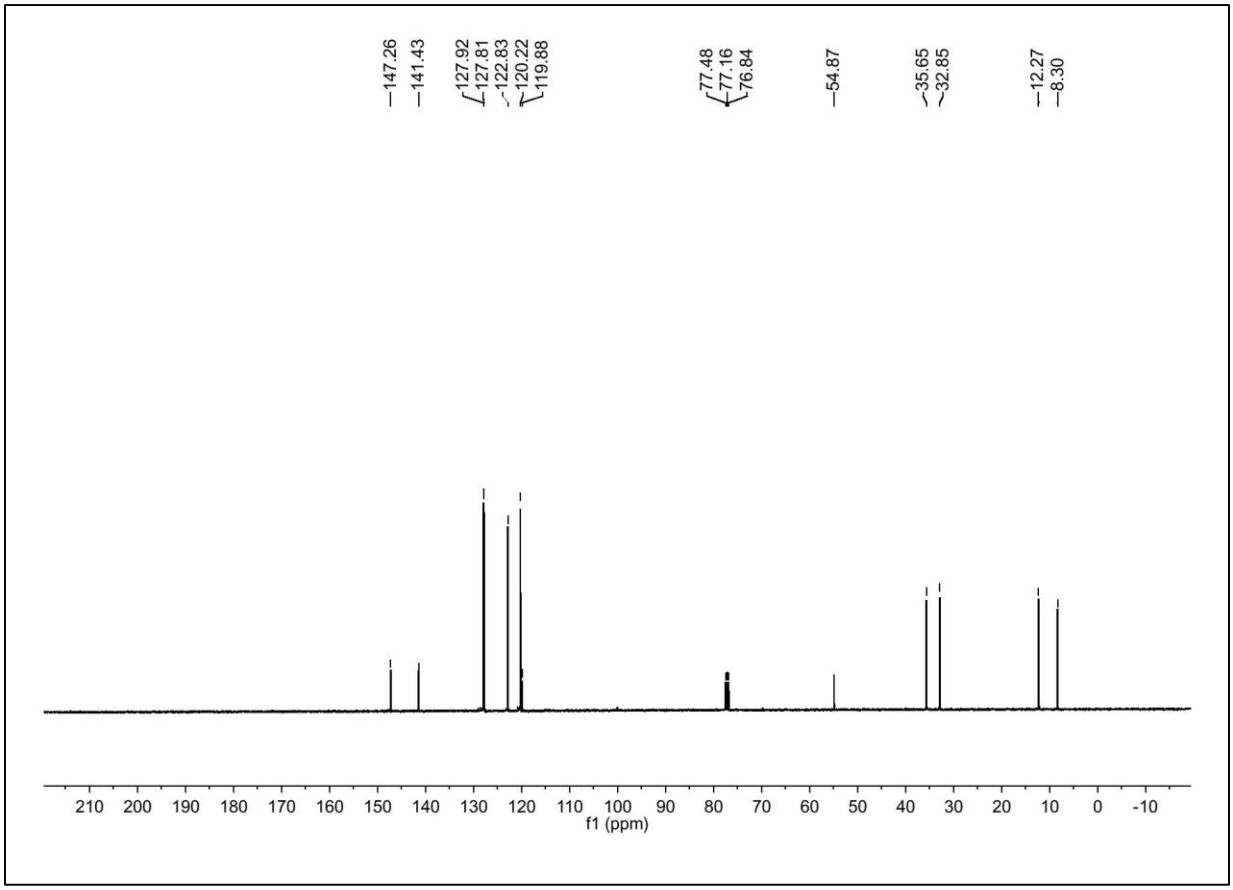
147.26
141.43
127.92
127.81
122.83
120.22
119.88
77.48
77.16
76.84
54.87
35.65
32.85
12.27
8.30
210 200 190 180 170 160 150 140 130 120 110 100 90 80 70 60 50 40 30 20 10 0 -10
f1 (ppm)

LC-MASS OF 2

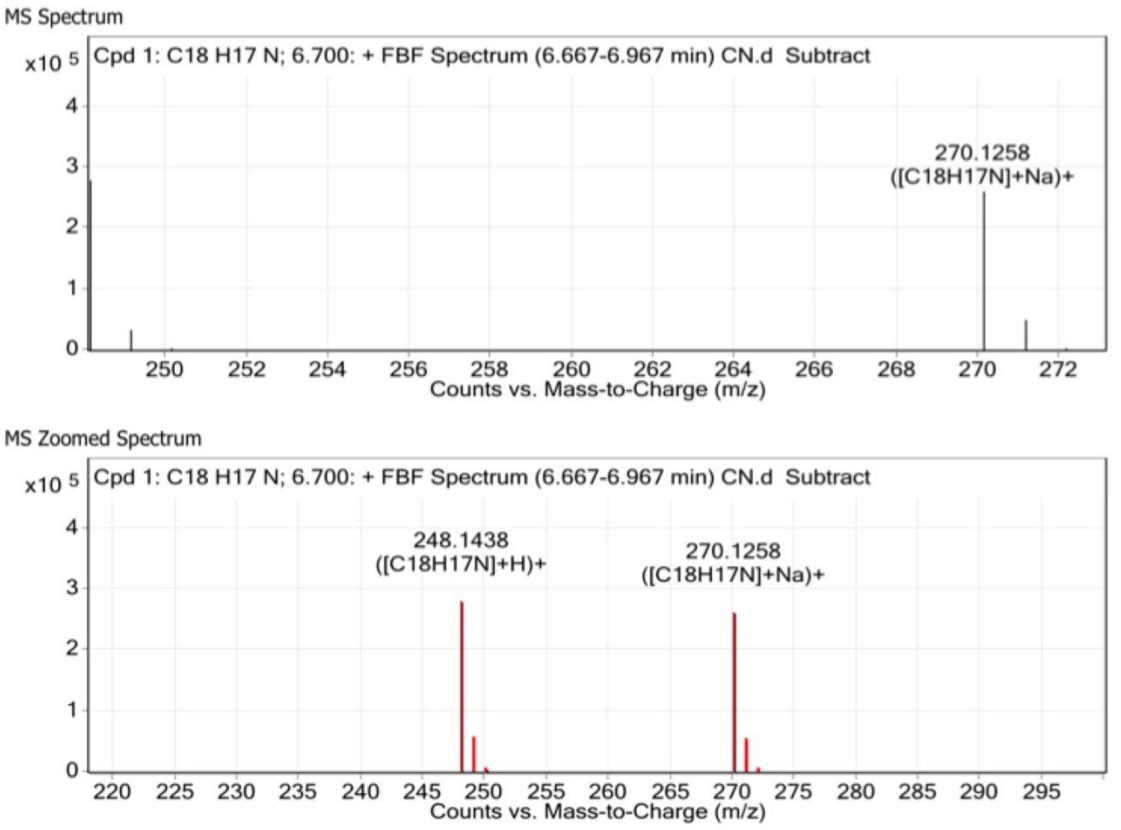
MS Spectrum
Cpd 1: C18 H17 N; 6.700: + FBF Spectrum (6.667-6.967 min) CN.d Subtract
x10 5
270.1258
([C18H17N]+Na)+
Counts vs. Mass-to-Charge (m/z)
MS Zoomed Spectrum
Cpd 1: C18 H17 N; 6.700: + FBF Spectrum (6.667-6.967 min) CN.d Subtract
x10 5
248.1438
([C18H17N]+H)+
270.1258
([C18H17N]+Na)+
Counts vs. Mass-to-Charge (m/z)

^{1}H NMR of 3

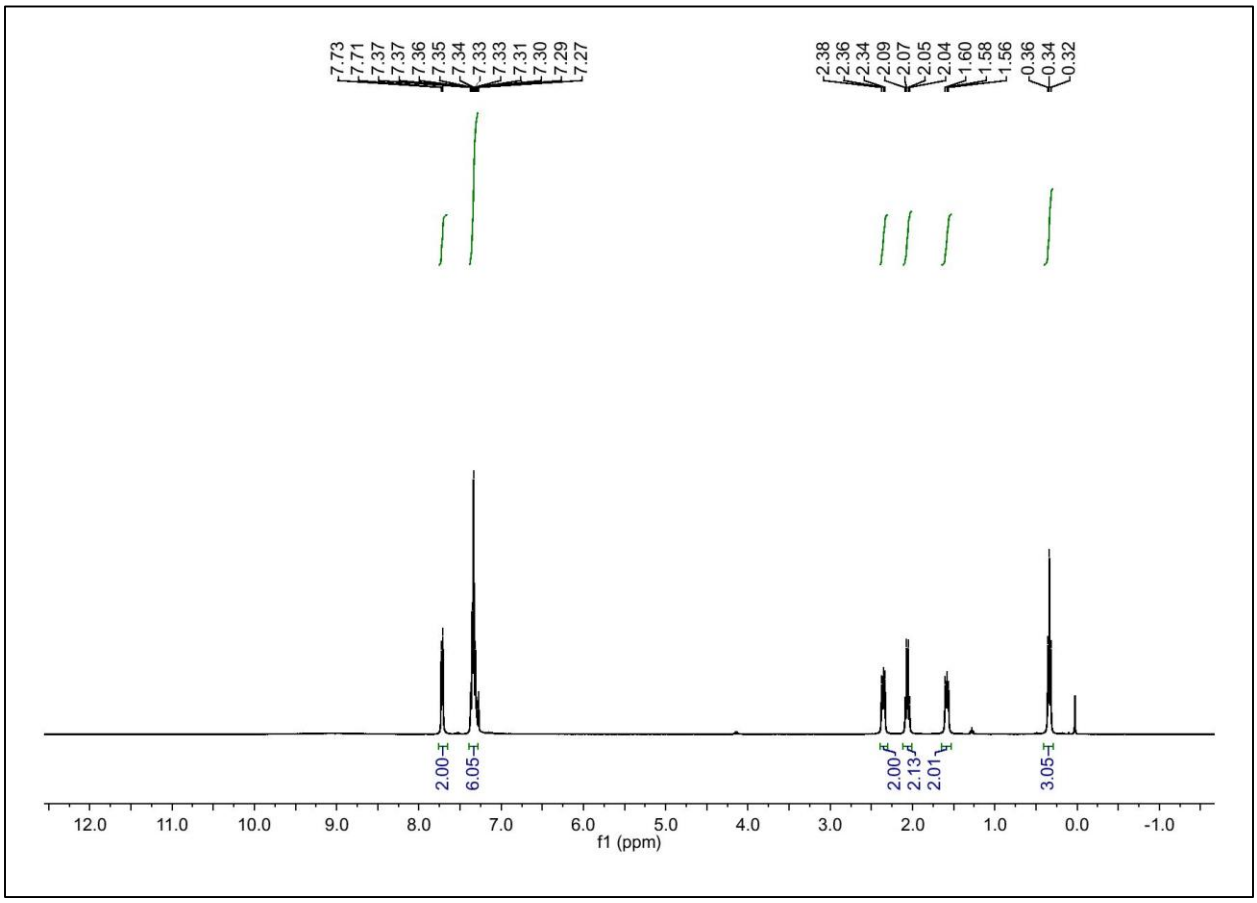
7.73
7.71
7.37
7.37
7.36
7.35
7.34
7.33
7.33
7.31
7.30
7.29
7.27
2.38
2.36
2.34
2.09
2.07
2.05
2.04
1.60
1.58
1.56
0.36
0.34
0.32
2.00
6.05
2.00
2.13
2.01
3.05
12.0
11.0
10.0
9.0
8.0
7.0
6.0
5.0
4.0
3.0
2.0
1.0
0.0
-1.0
f1 (ppm)

^{13}C NMR of 3

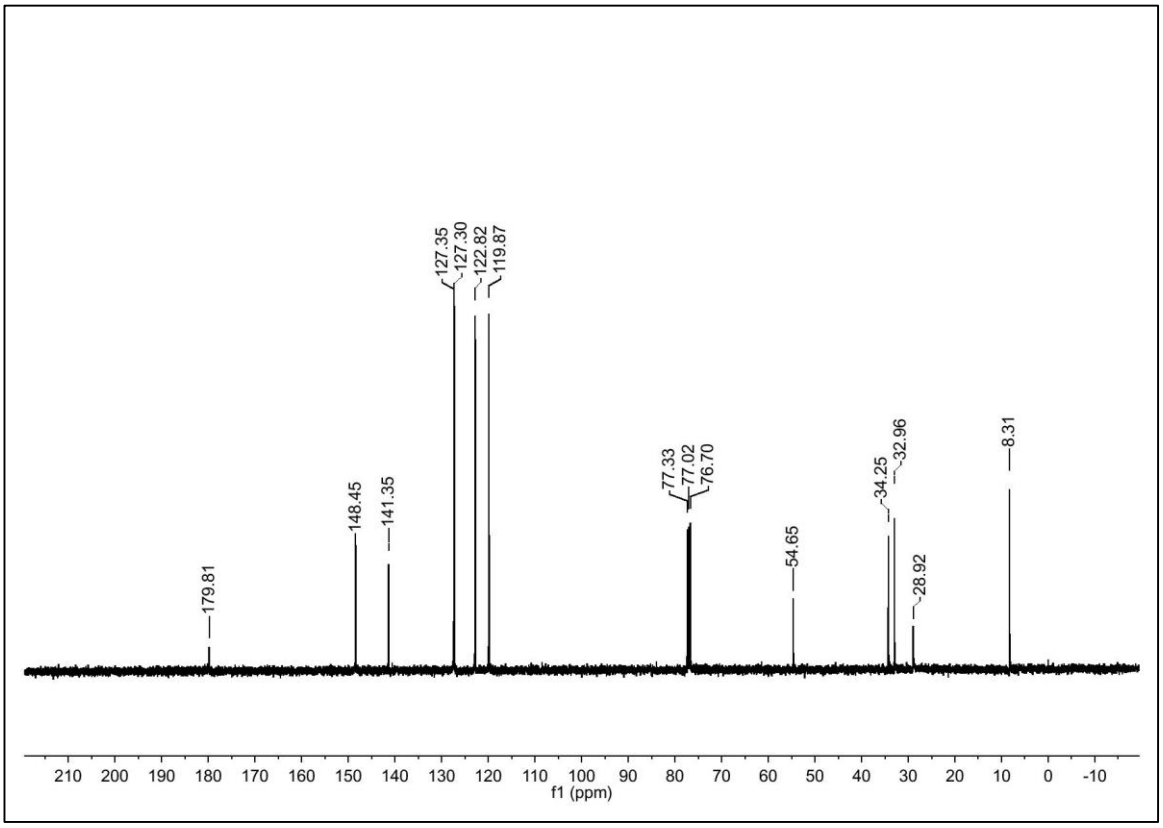

LC-MASS of 3

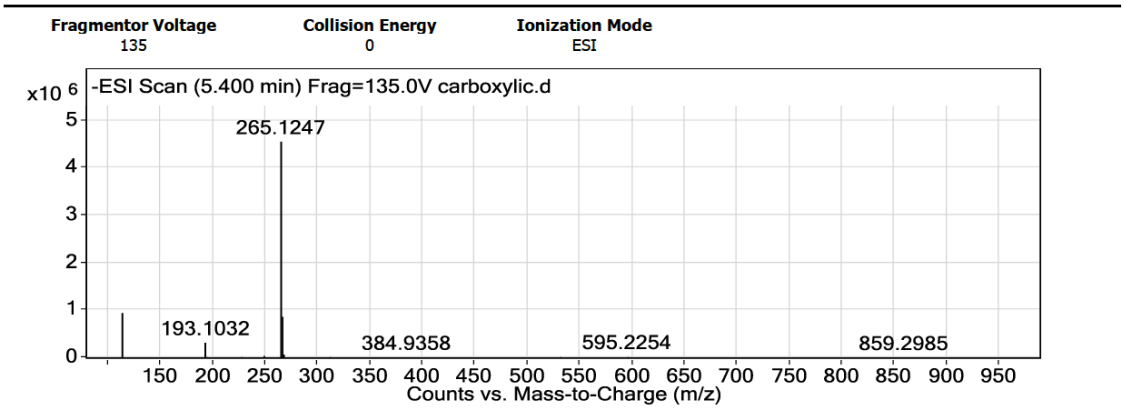

^{1}H NMR of 4

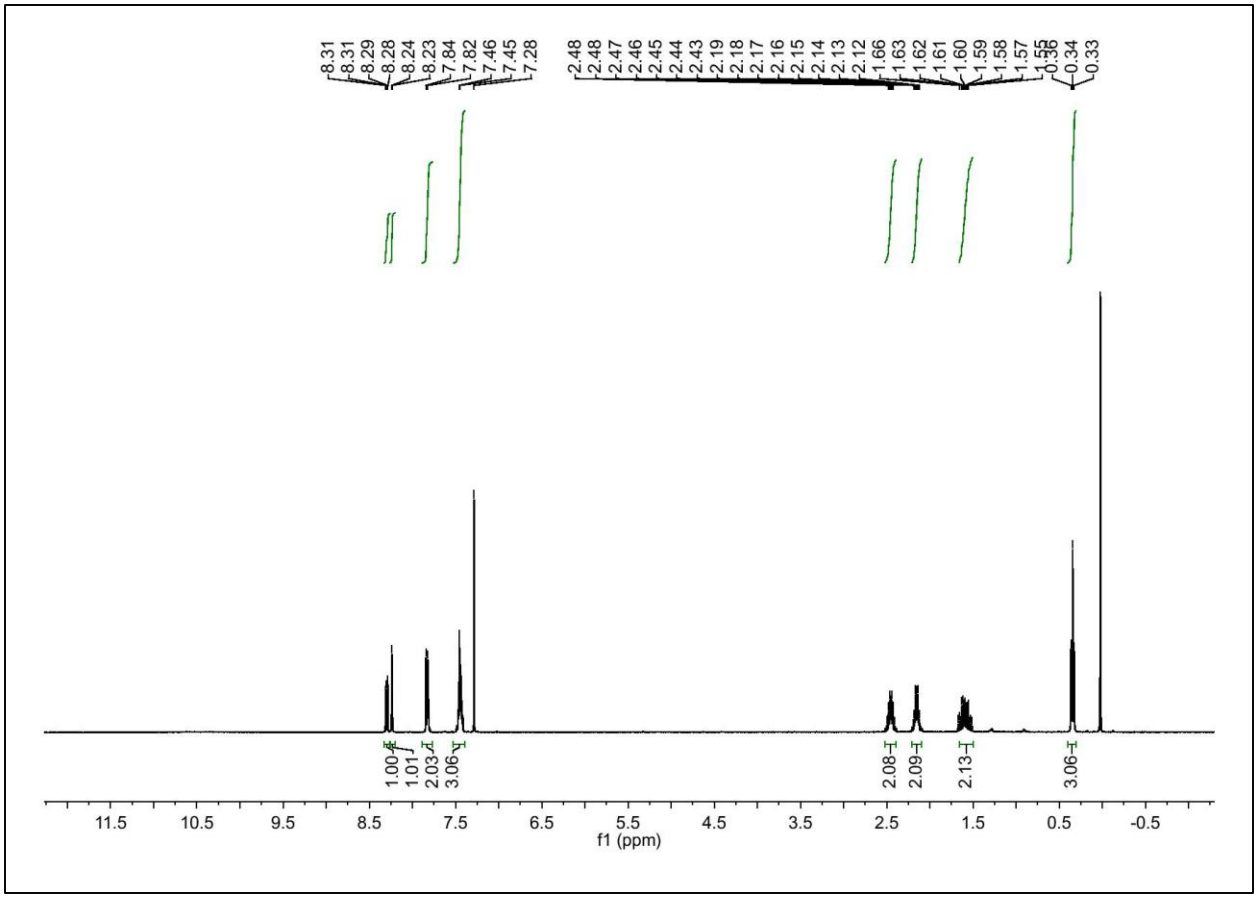
8.31
8.31
8.29
8.28
8.24
8.23
7.84
7.82
7.46
7.45
7.28
2.48
2.48
2.47
2.46
2.45
2.44
2.43
2.19
2.18
2.17
2.16
2.15
2.14
2.13
2.12
1.66
1.63
1.62
1.61
1.60
1.59
1.58
1.57
0.34
0.33
1.00
1.01
2.03
3.06
2.08
2.09
2.13
3.06
11.5
10.5
9.5
8.5
7.5
6.5
5.5
4.5
3.5
2.5
1.5
0.5
-0.5
f1 (ppm)

^{13}C NMR of 4

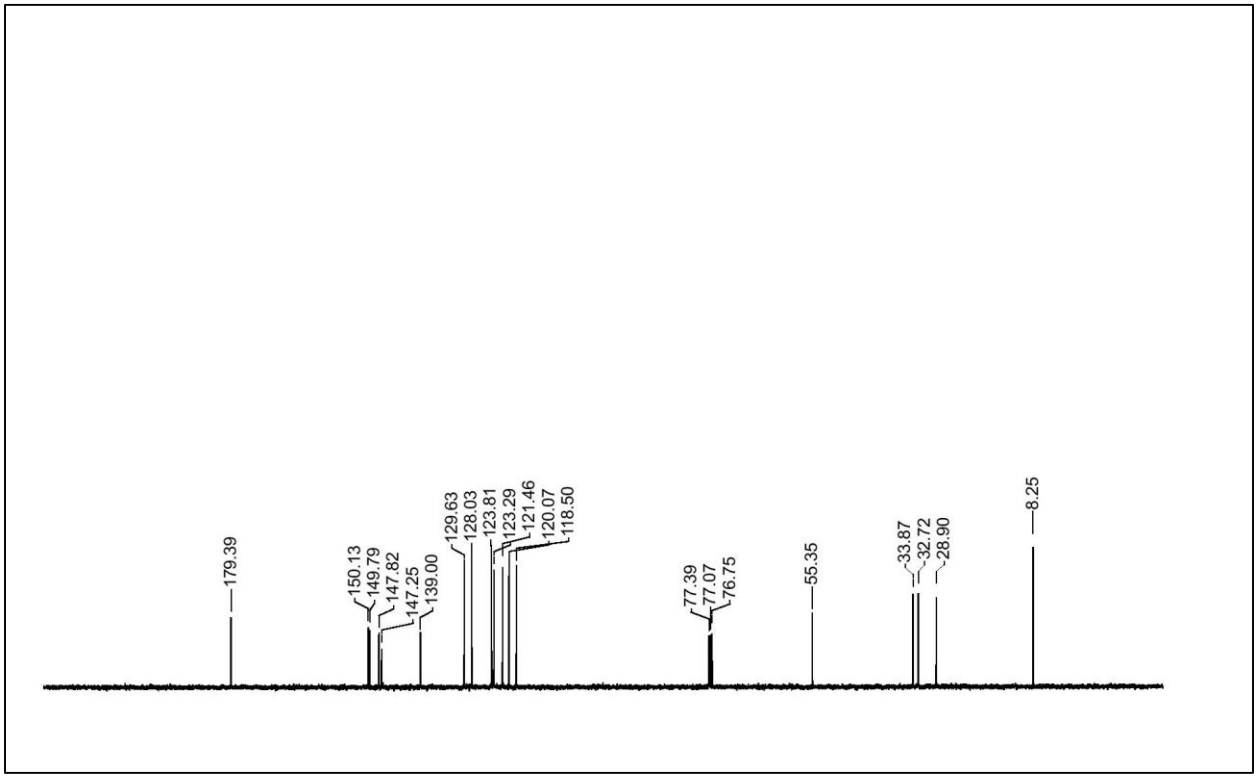
179.39
150.13
149.79
147.82
147.25
139.00
129.63
128.03
123.81
123.29
121.46
120.07
118.50
77.39
77.07
76.75
55.35
33.87
32.72
28.90
8.25

HRMS of 4

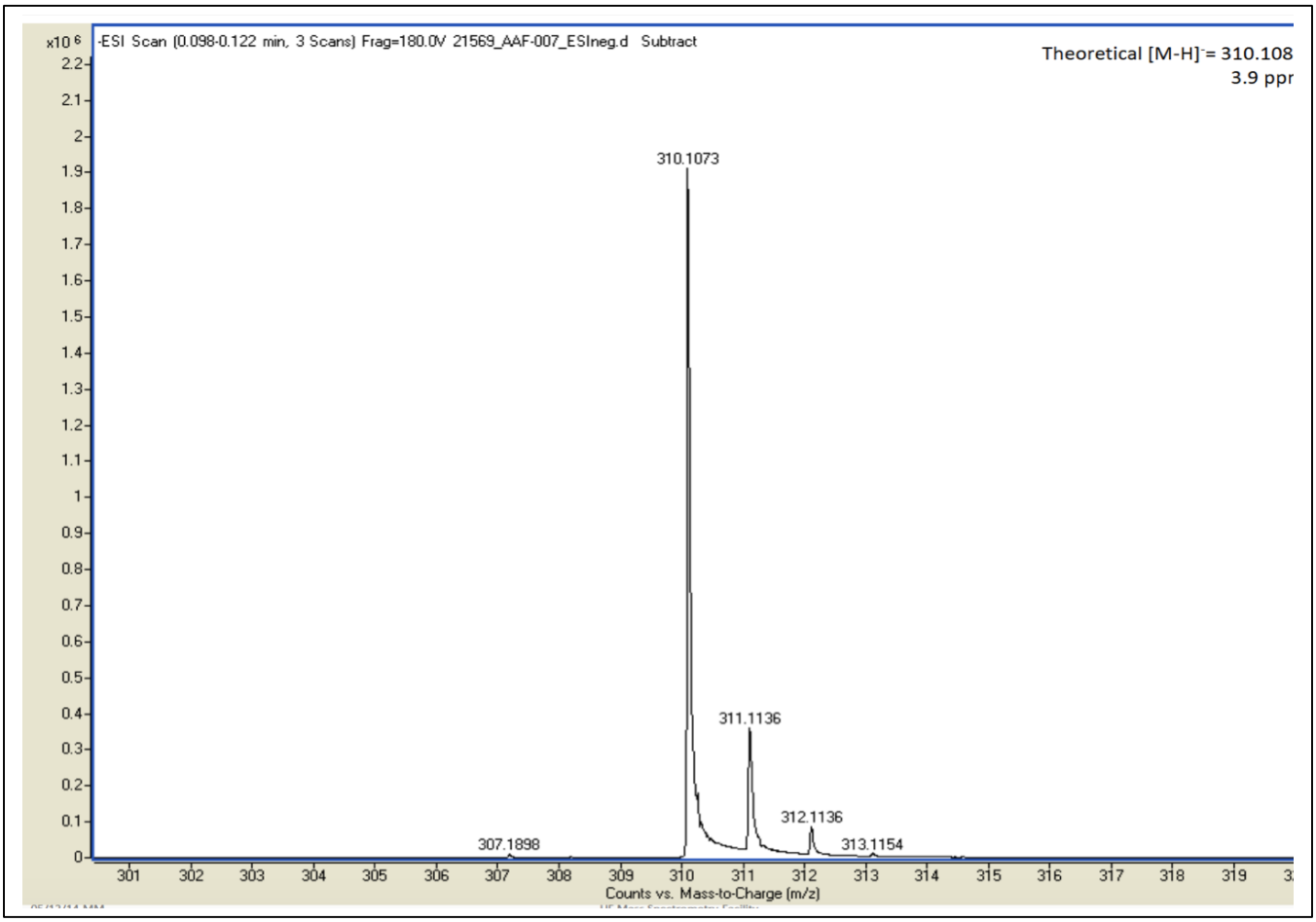
x10 6
-ESI Scan (0.098-0.122 min, 3 Scans) Frag=180.0V 21569_AAF-007_ESIneg.d Subtract
Theoretical [M-H]⁻= 310.108
3.9 ppr
310.1073
311.1136
312.1136
313.1154
307.1898
Counts vs. Mass-to-Charge (m/z)

^{1}H NMR of 5

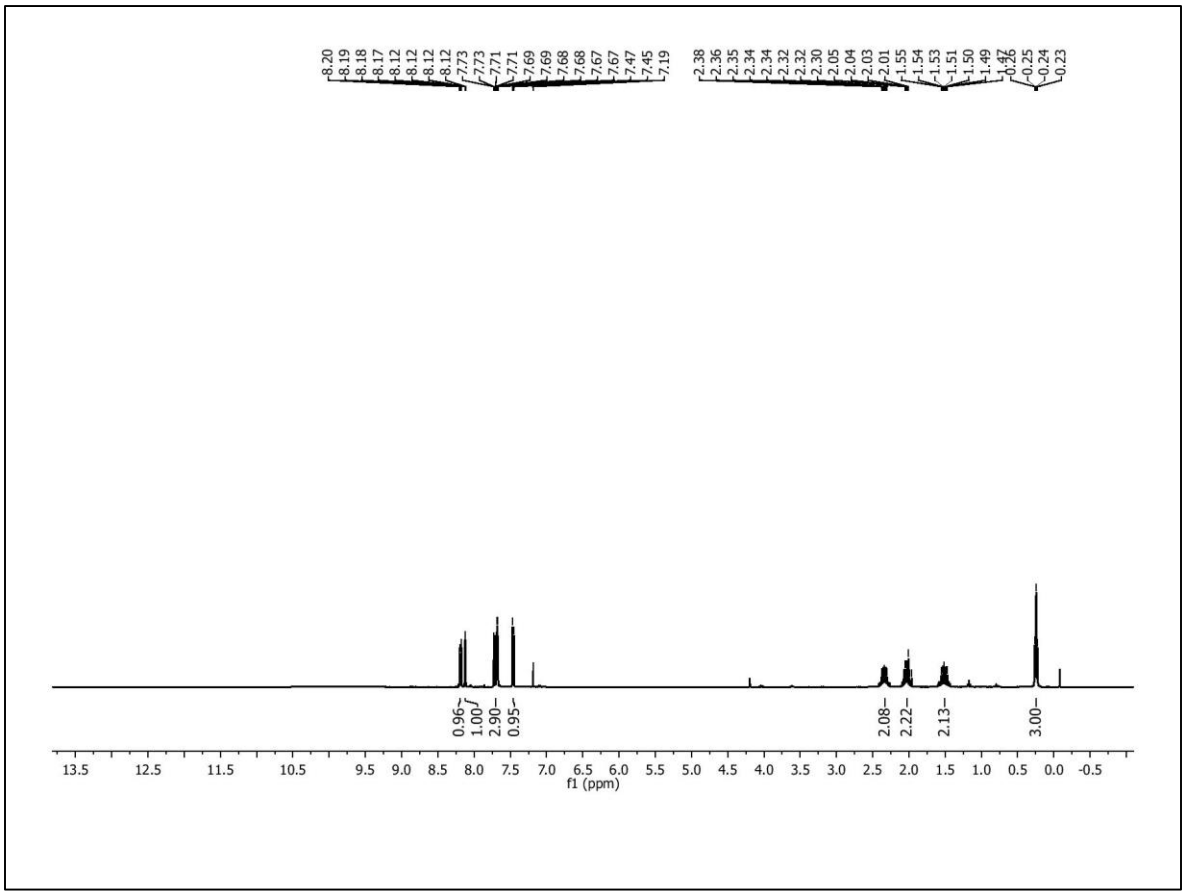
8.20
8.19
8.18
8.17
8.12
8.12
8.12
8.12
7.73
7.73
7.71
7.71
7.69
7.69
7.68
7.68
7.67
7.67
7.47
7.45
7.19
2.38
2.36
2.35
2.34
2.34
2.32
2.32
2.30
2.05
2.04
2.03
2.01
1.55
1.54
1.53
1.51
1.50
1.49
1.47
0.26
0.25
0.24
0.23
0.96
1.00
2.90
0.95
2.08
2.22
2.13
3.00
13.5 12.5 11.5 10.5 9.5 9.0 8.5 8.0 7.5 7.0 6.5 6.0 5.5 5.0 4.5 4.0 3.5 3.0 2.5 2.0 1.5 1.0 0.5 0.0 -0.5
f1 (ppm)

^{13}C NMR of 5

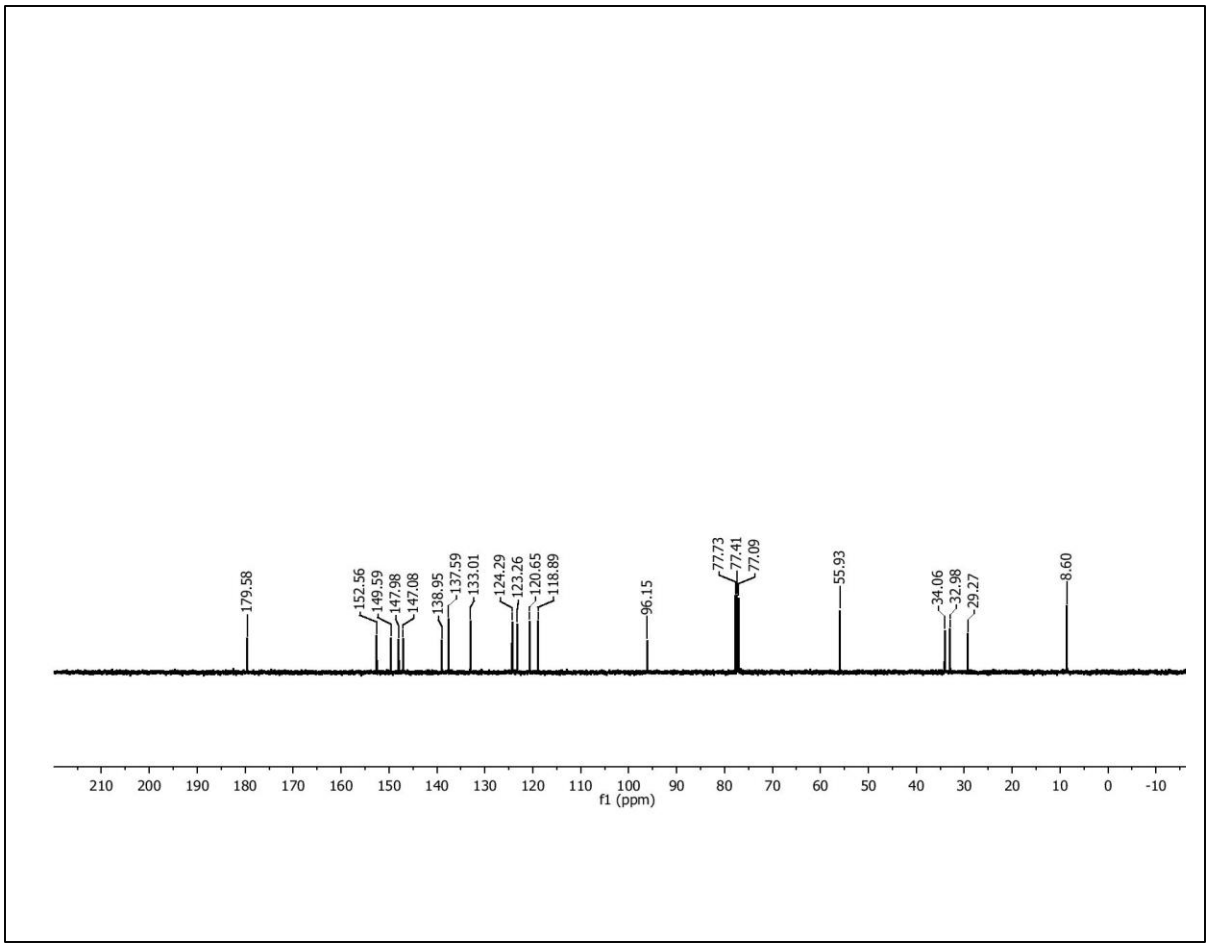

LC-MASS of 5

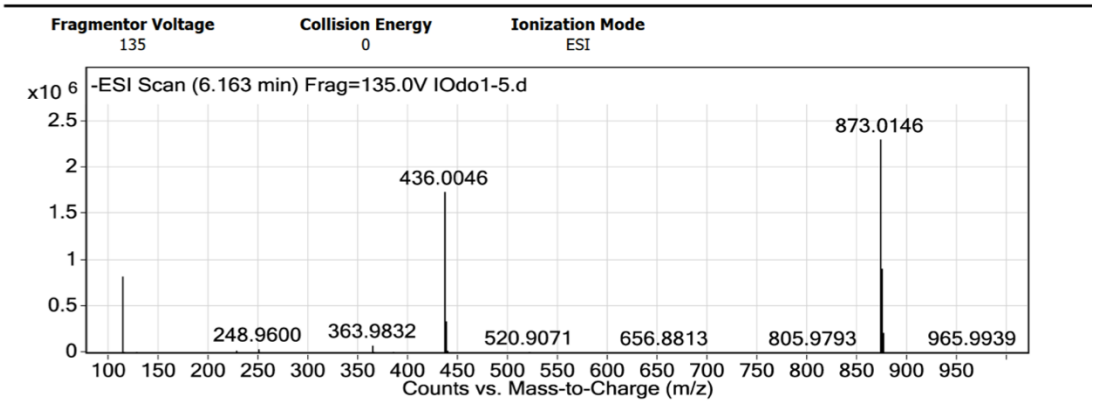

^{1}H NMR of 8

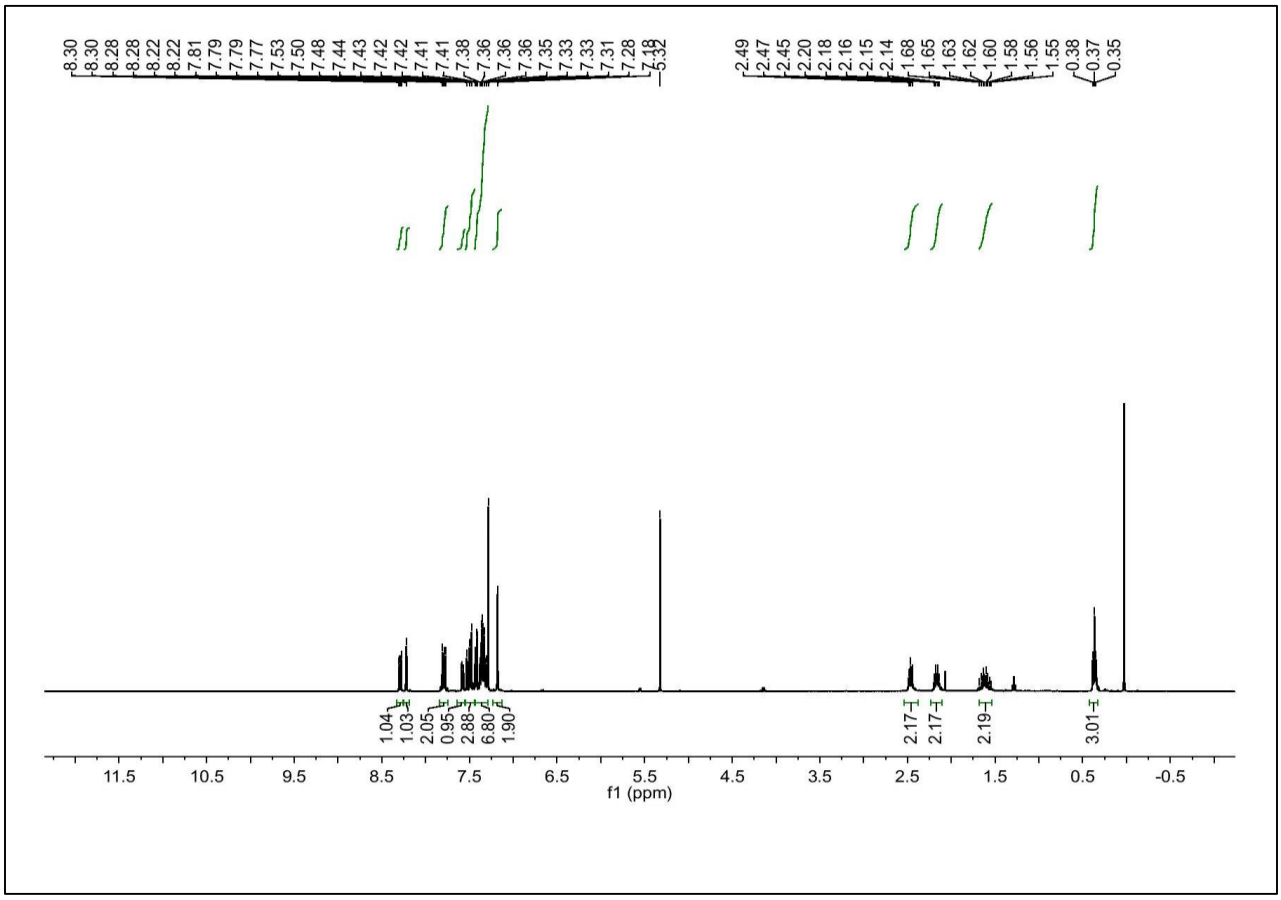
8.30
8.30
8.28
8.28
8.22
8.22
7.81
7.79
7.79
7.77
7.53
7.50
7.48
7.44
7.43
7.42
7.42
7.41
7.41
7.38
7.36
7.36
7.36
7.35
7.33
7.33
7.31
7.28
5.32
2.49
2.47
2.45
2.20
2.18
2.16
2.15
2.14
1.68
1.65
1.63
1.62
1.60
1.58
1.56
1.55
0.38
0.37
0.35
1.04
1.03
2.05
0.95
2.88
6.80
1.90
2.17
2.17
2.19
3.01
11.5
10.5
9.5
8.5
7.5
6.5
5.5
4.5
3.5
2.5
1.5
0.5
-0.5
f1 (ppm)

^{1}H NMR of 8

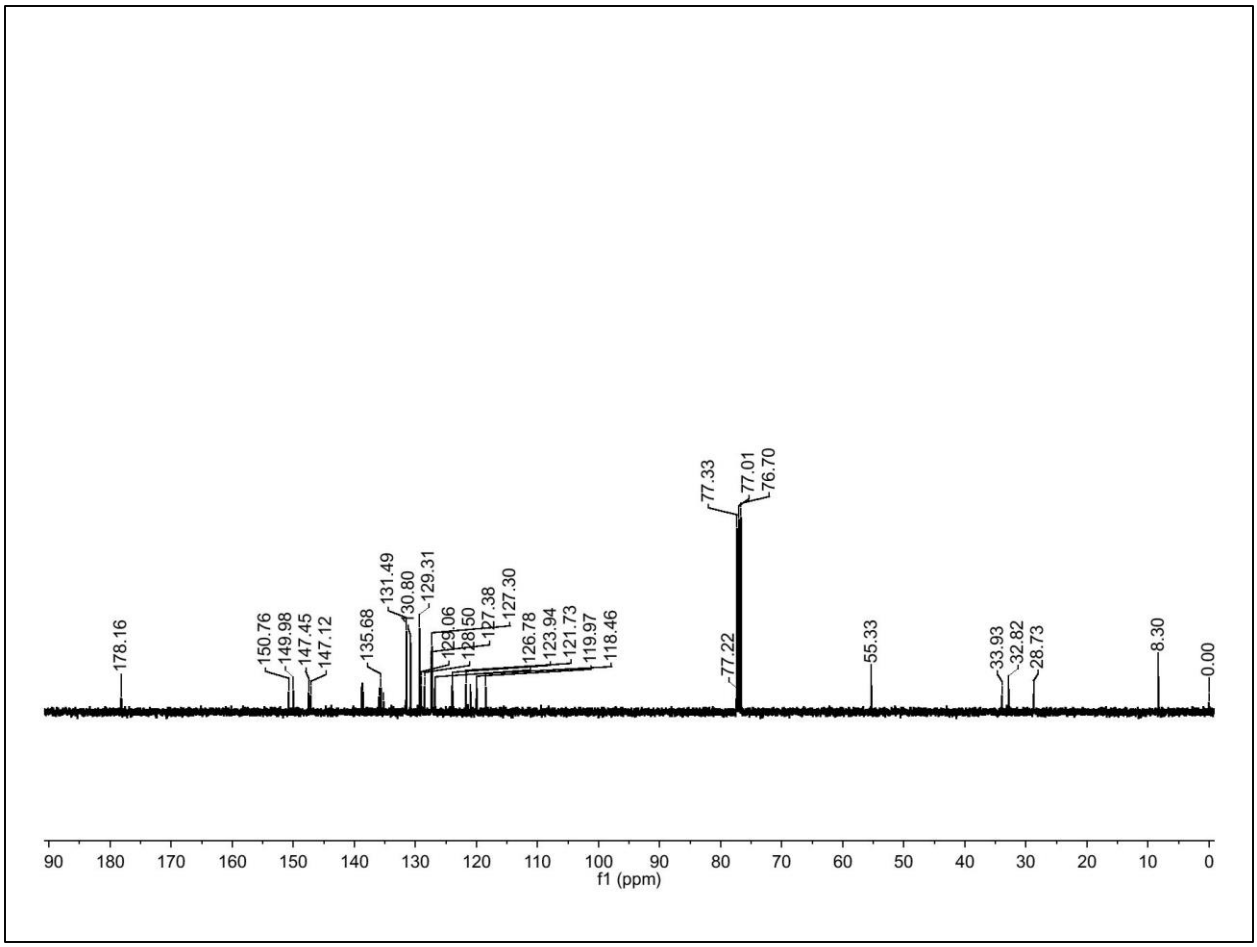
178.16
150.76
149.98
147.45
147.12
135.68
131.49
130.80
129.31
129.06
128.50
127.38
127.30
126.78
123.94
121.73
119.97
118.46
77.33
77.01
76.70
77.22
55.33
33.93
32.82
28.73
8.30
0.00
90 180 170 160 150 140 130 120 110 100 90 80 70 60 50 40 30 20 10 0
f1 (ppm)

HRMS of 8

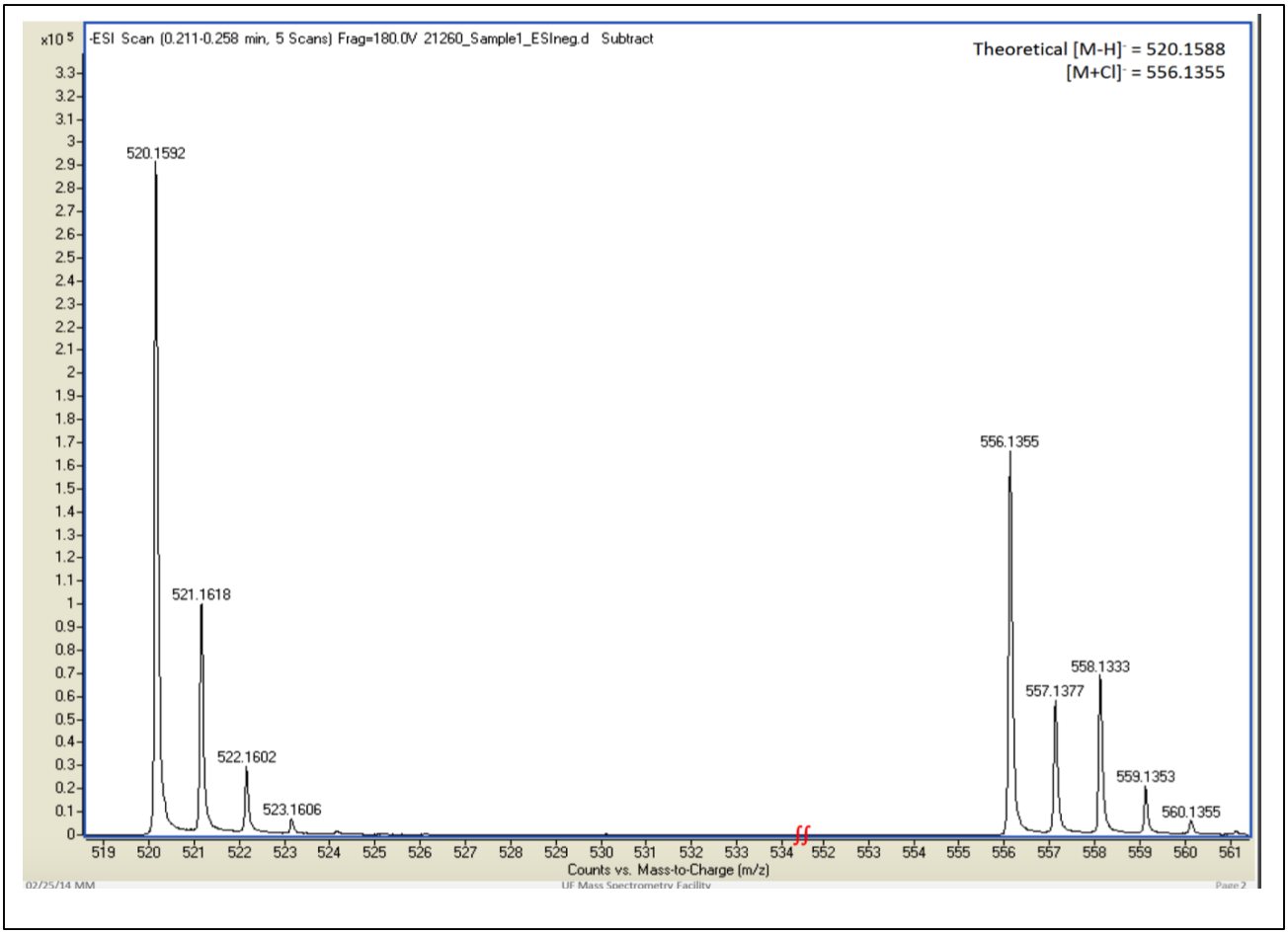
x10 5
-ESI Scan (0.211-0.258 min, 5 Scans) Frag=180.0V 21260_Sample1_ESIneg.d Subtract
Theoretical [M-H]- = 520.1588
[M+Cl]- = 556.1355
520.1592
521.1618
522.1602
523.1606
556.1355
557.1377
558.1333
559.1353
560.1355
Counts vs. Mass-to-Charge (m/z)
02/25/14 MM
UF Mass Spectrometry Facility
Page 2

^{1}H NMR of PAG 9

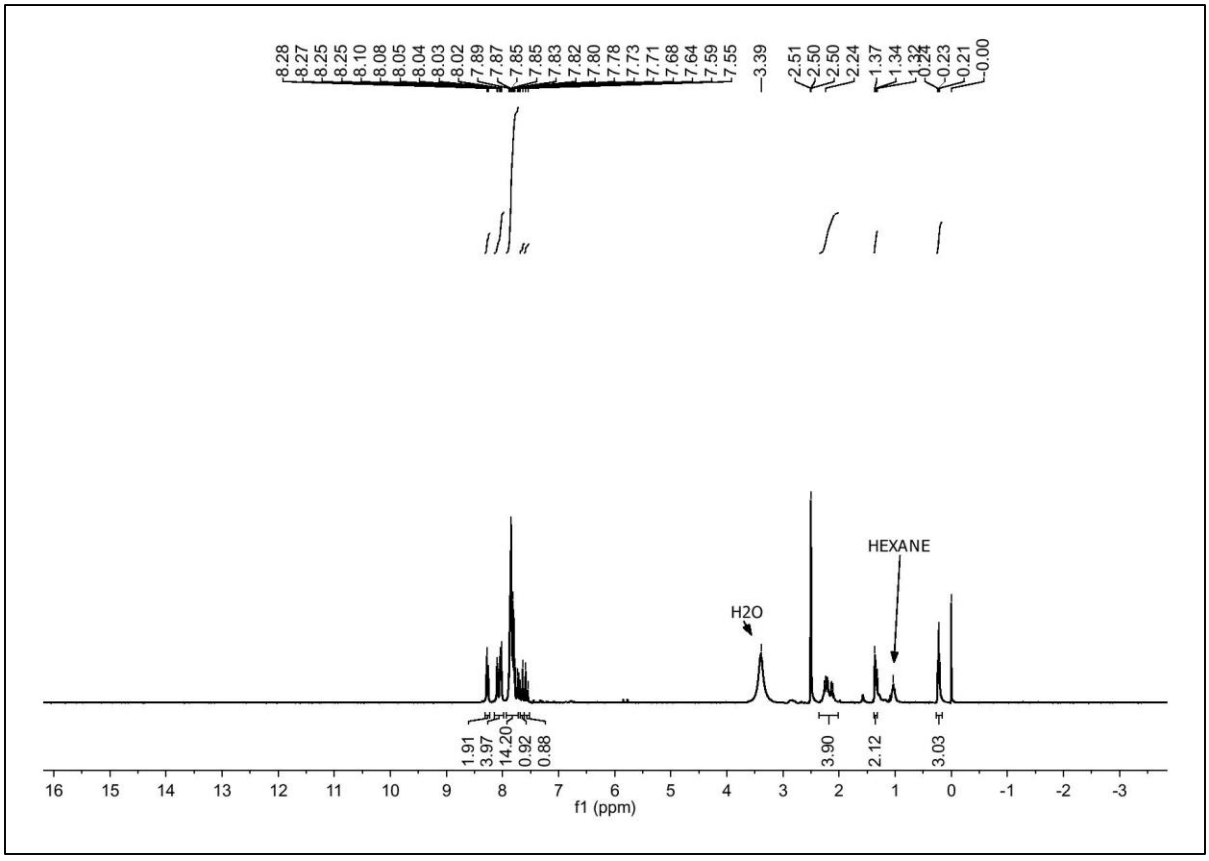

^{13}C NMR of PAG 9

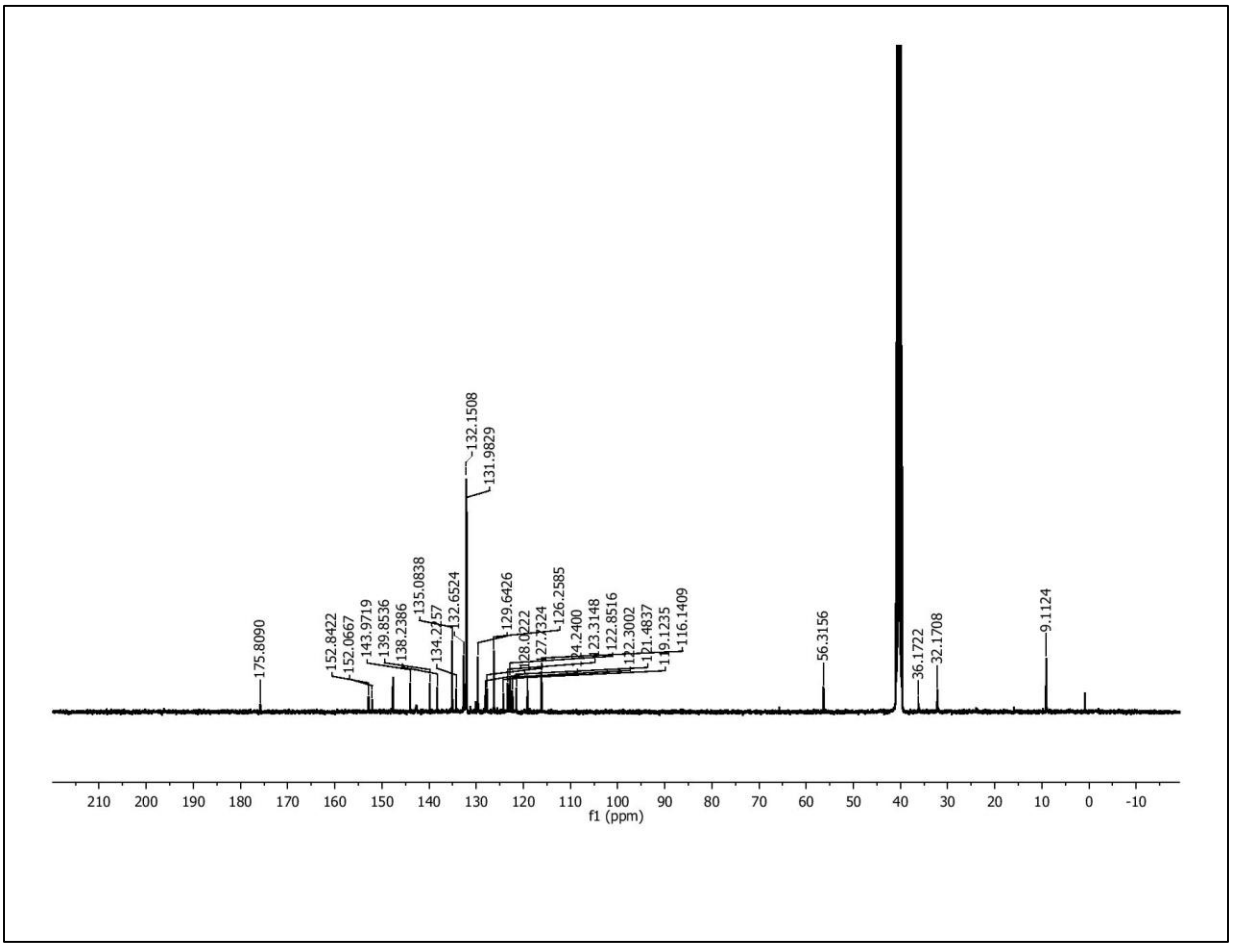

HRMS of PAG 9

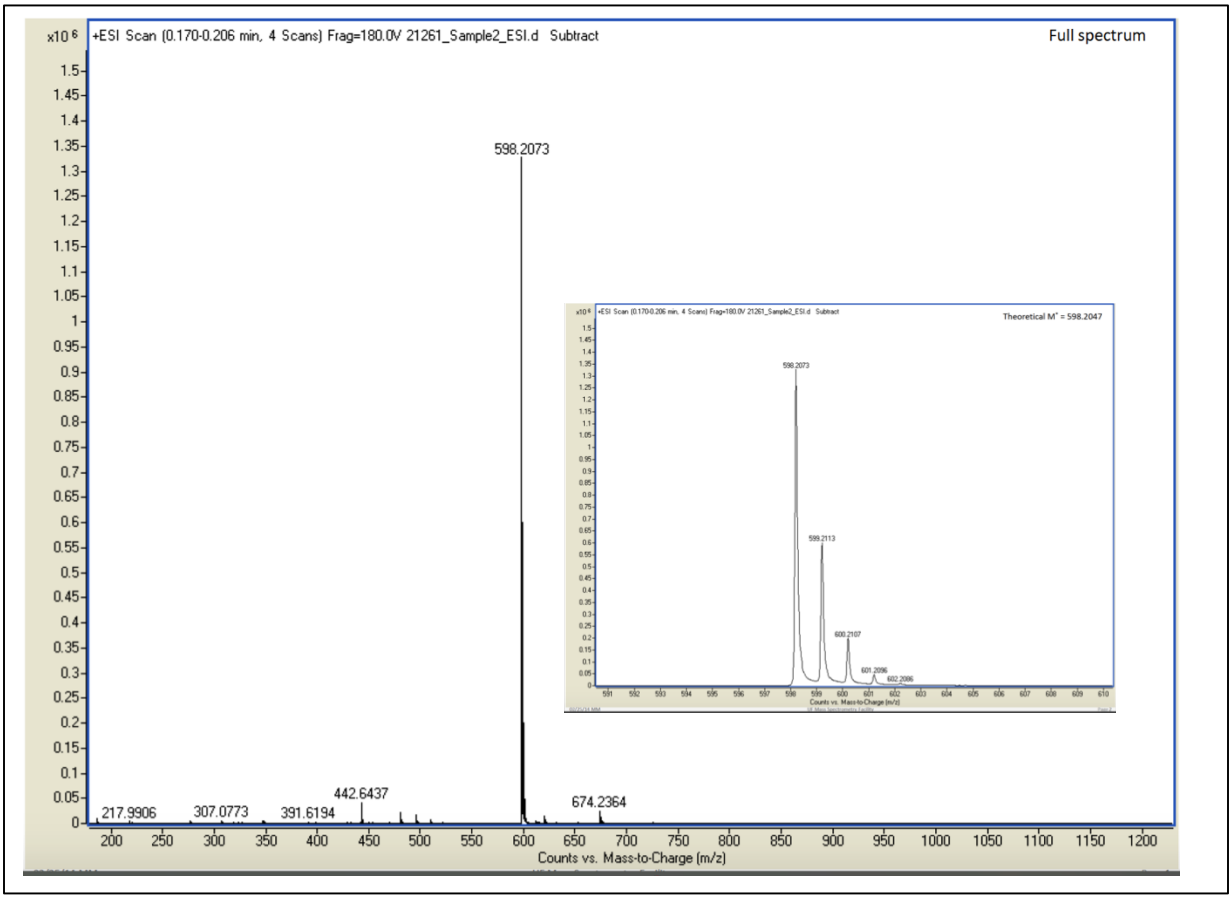
x10 6
+ESI Scan (0.170-0.206 min, 4 Scans) Frag=180.0V 21261_Sample2_ESI.d Subtract
Full spectrum
598.2073
442.6437
674.2364
217.9906
307.0773
391.6194
Counts vs. Mass-to-Charge (m/z)
Theoretical M+ = 598.2047
599.2113
600.2107
601.2096
602.2086

^{1}H NMR of PAG-PEG

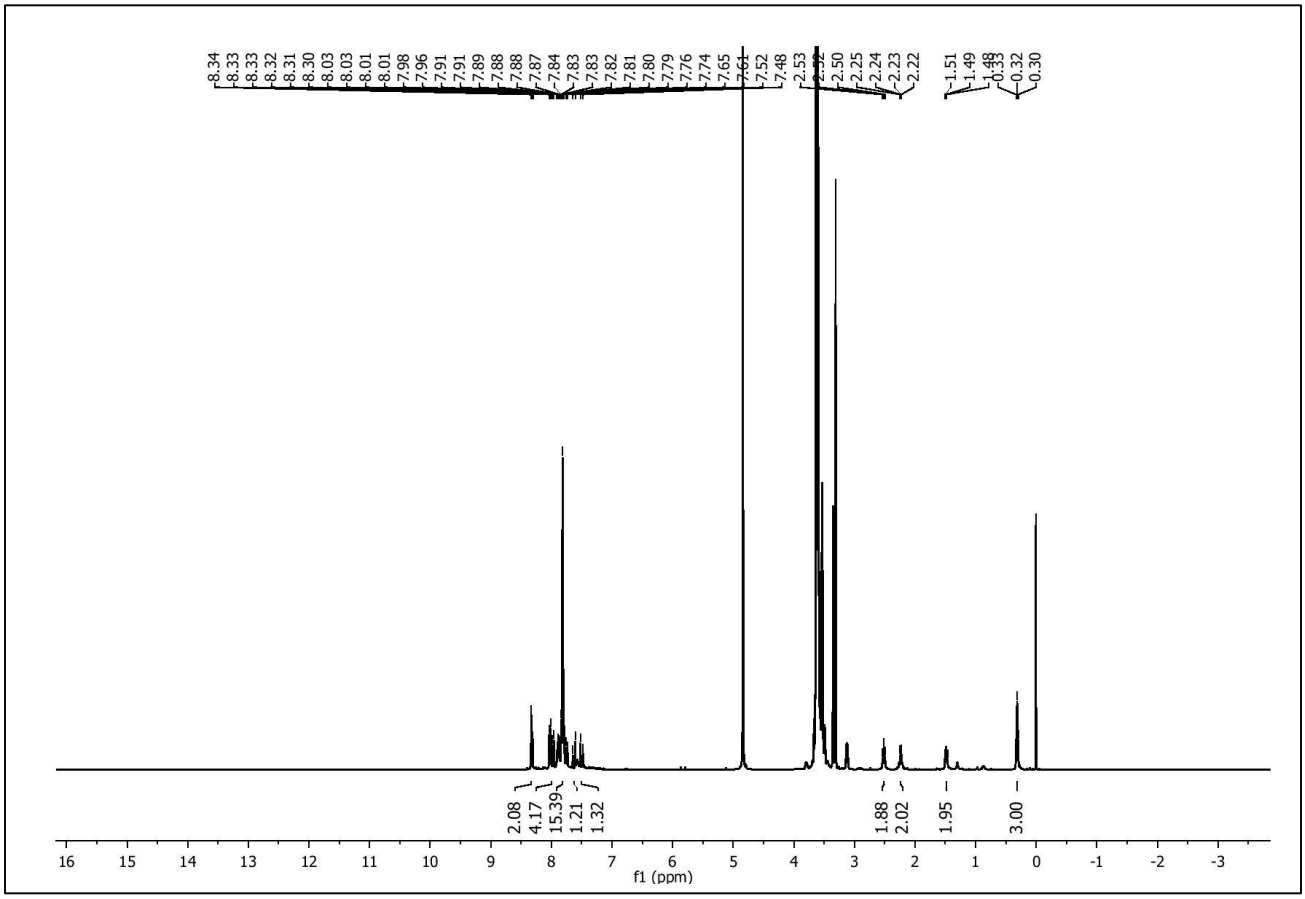

^{13}C NMR of PAG-PEG

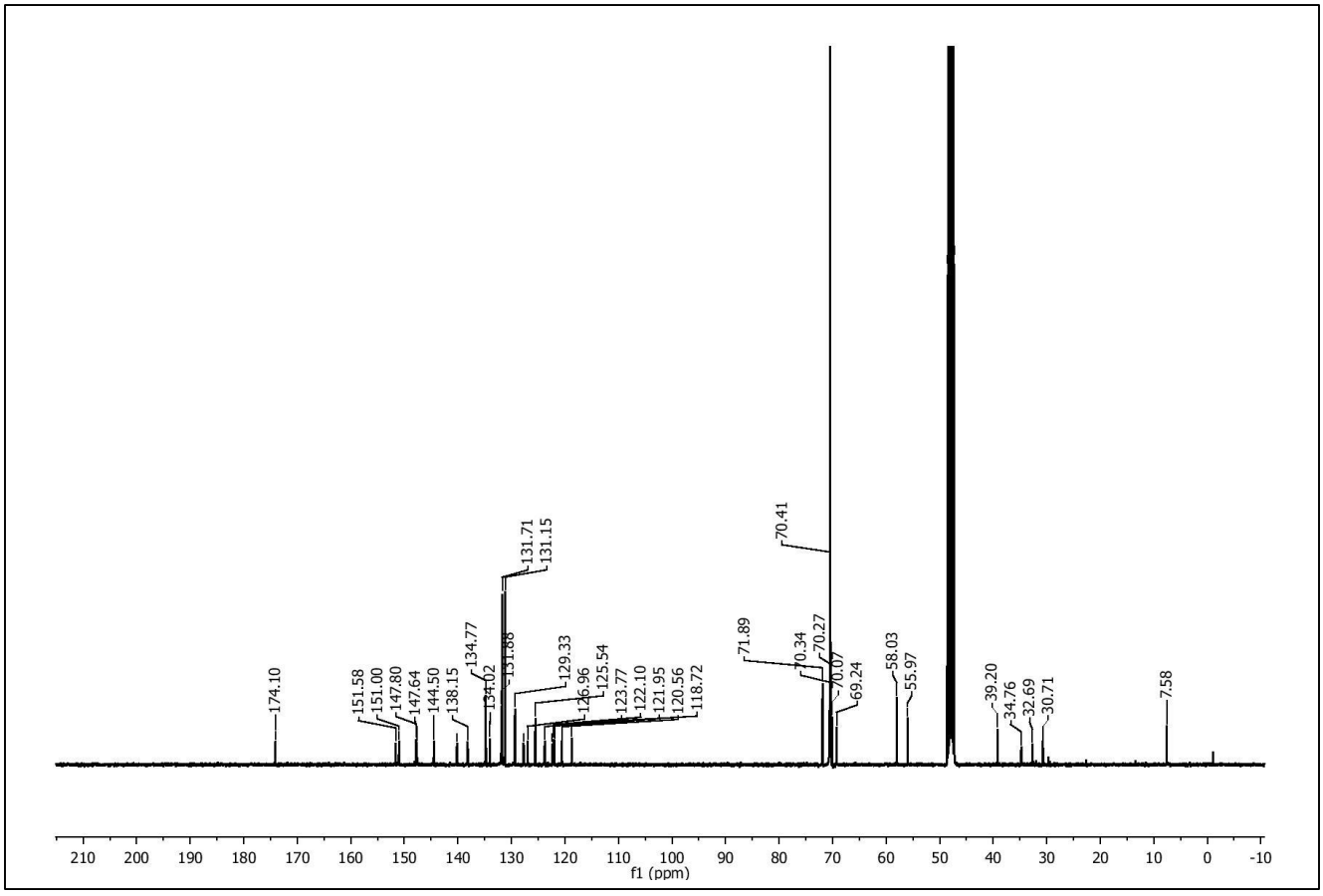

MALDI-TOF-MS of PAG-PEG

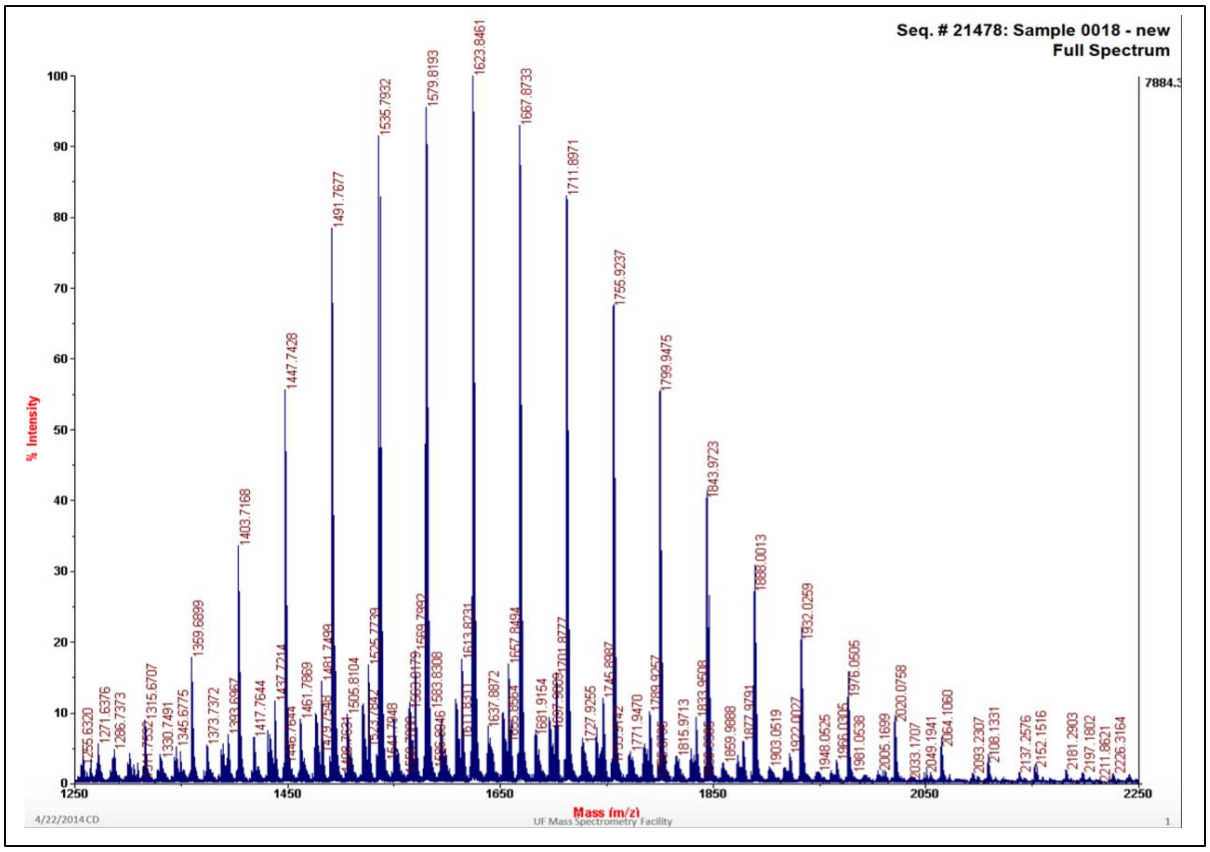

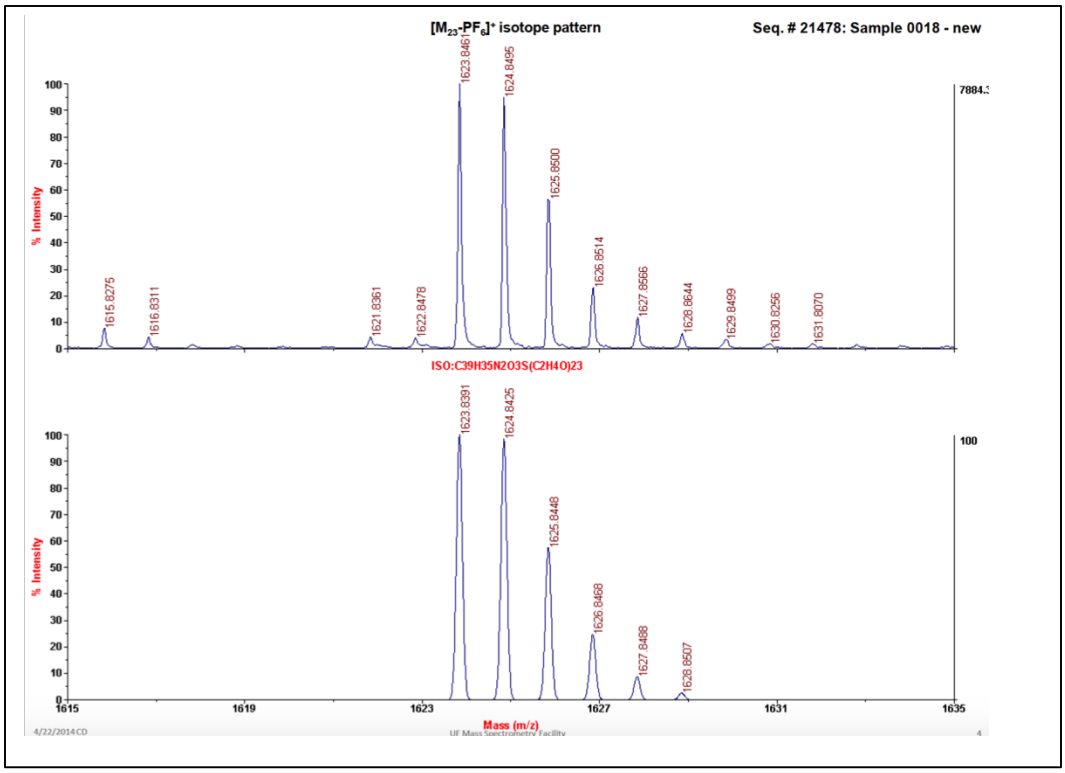

^{1}H NMR of PAG-NH-BOC

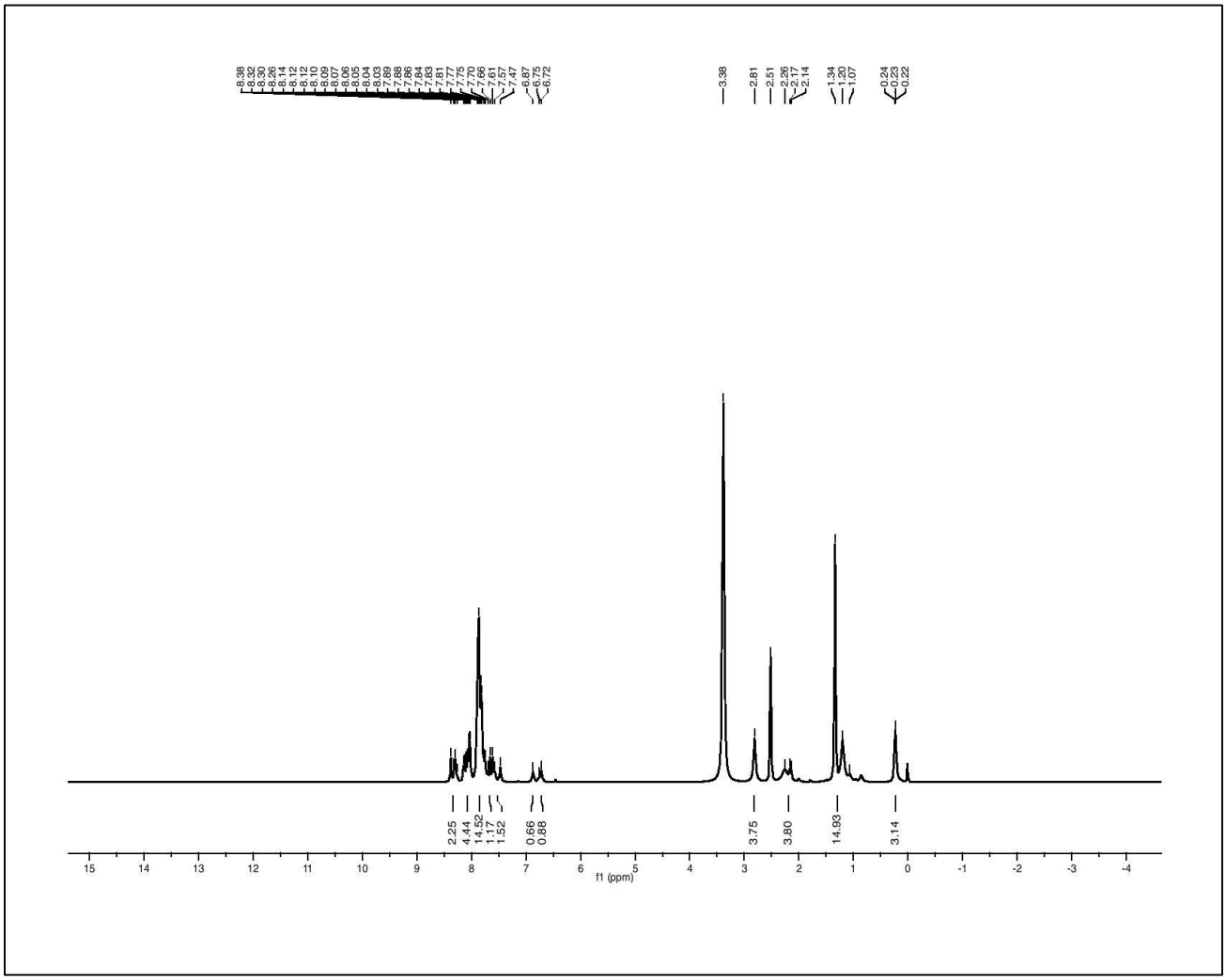

^{13}C NMR of PAG-NH-BOC

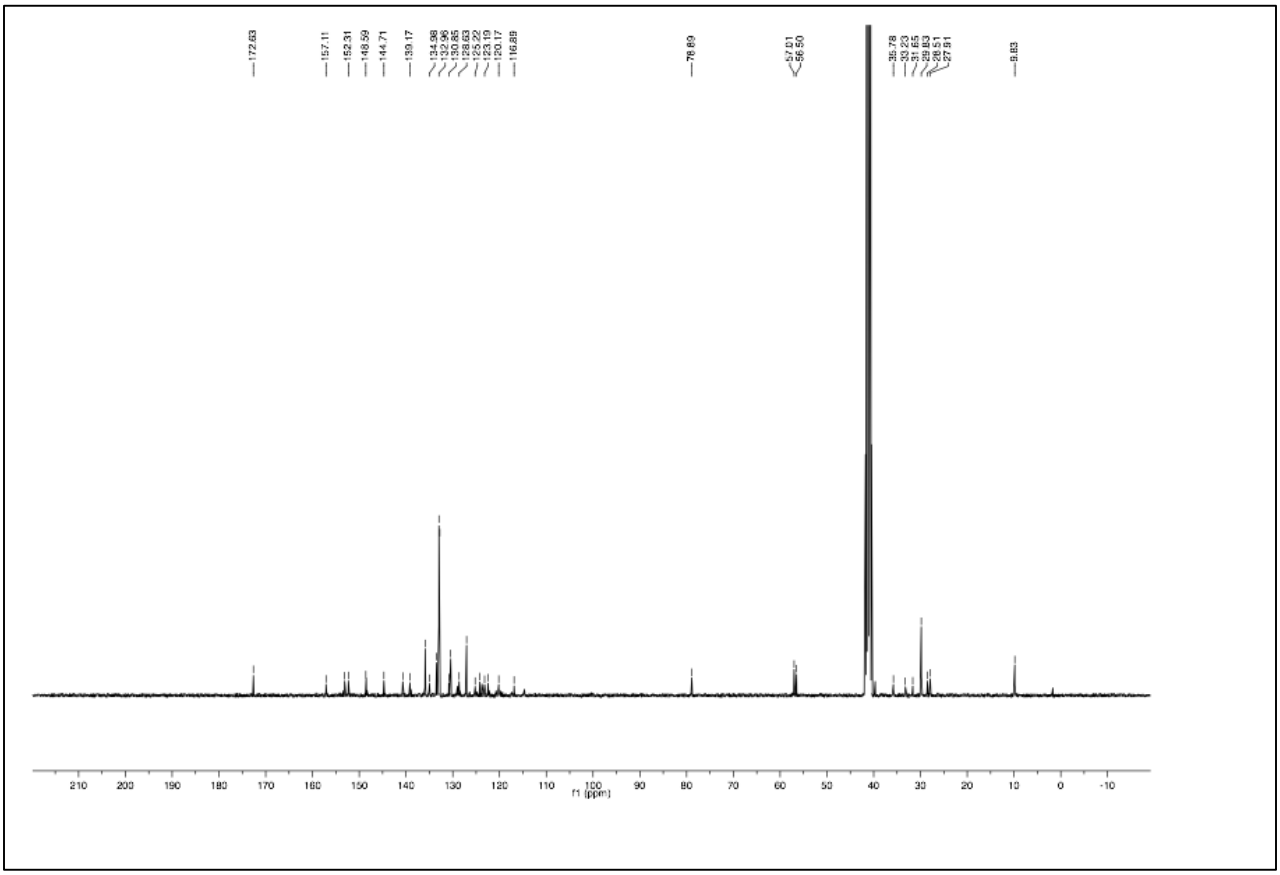

LC MASS of PAG-NH-BOC

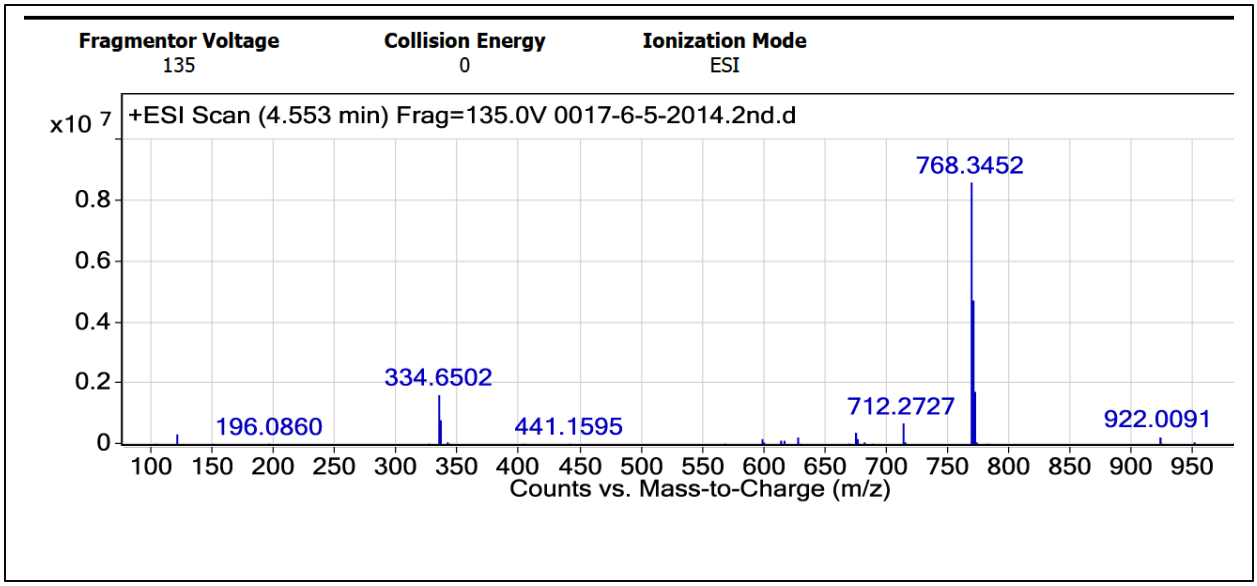

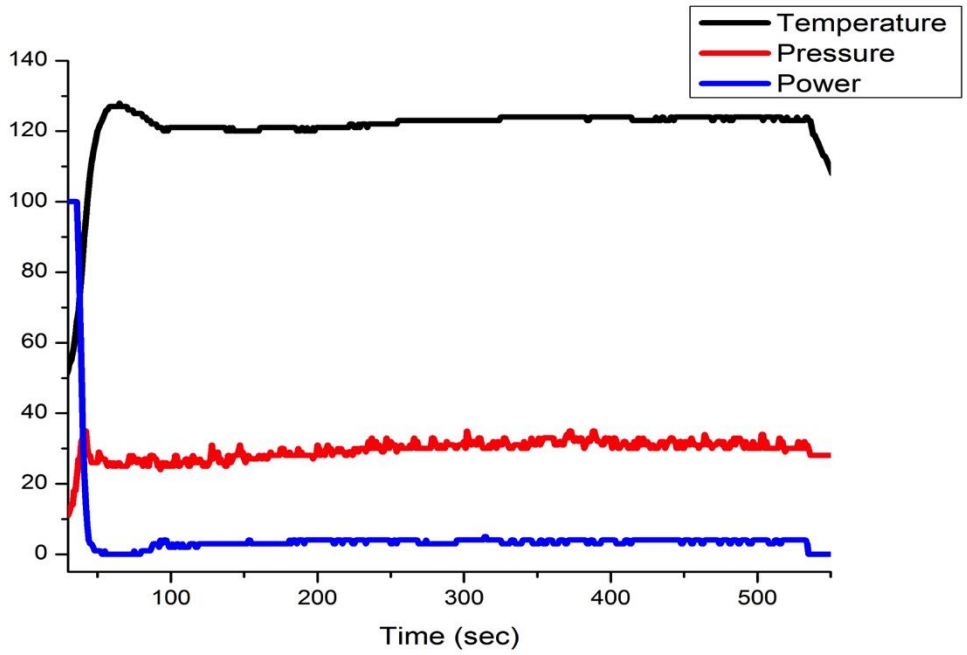
Temperature
Pressure
Power
140
120
100
80
60
40
20
0
100
200
300
400
500
Time (sec)

REFERENCES

1. Anand P, Kunnumakara AB, Sundaram C, et al. Cancer is a Preventable Disease that Requires Major Lifestyle Changes. *Pharmaceutical Research*. **2008**;25(9):2097-2116.

2. Parkin, DM; Boyd, L; Walker, LC (6 December 2011). The fraction of cancer attributable to lifestyle and environmental factors in the UK. *British journal of cancer*. **2010**;105 Suppl 2: S77–81.

3. (a) Oleinick, N. L.; Morris, R. L.; Belichenko, I. The role of apoptosis in response to photodynamic therapy: what, where, why, and how. Photochem. Photobiol. Sci. 2002, 1, (b) Sharman, W. M.; Allen, C. M.; van Lier, *J. E. Methods Enzymol*. **2000**, 319, 376.

4. Yavari, N.; Andersson-Engels, S.; Segersten, U.; Malmstrom, P. U. An overview on preclinical and clinical experiences with photodynamic therapy for bladder cancer. *Can. J. Urol.* **2011**, 18, 5778.

5. Allison, R. R.; Downie, G. H.; Cuenca, R.; Hu, X. H.; Childs, C. J. H.; Sibata, C. H., Photosensitizers in clinical PDT. *Photodiagn Photodyn.* **2004**, 1 (1), 27-42.

6. Wang, I.; Bendsoe, N.; Klinteberg, C. A. F.; Enejder, A. M. K.; Andersson-Engels, S.; Svanberg, S.; Svanberg, K., Photodynamic therapy vs. cryosurgery of basal cell carcinomas: results of a phase III clinical trial. *Brit J Dermatol.* **2001**, 144 (4), 832-840.

7. Morton, C. A.; Whitehurst, C.; McColl, J. H.; Moore, J. V.; MacKie, R. M., Photodynamic therapy for large or multiple patches of Bowen disease and basal cell carcinoma. *Arch Dermatol.* **2001**, 137 (3), 319-324.

8. Sibata, C. H.; Colussi, V. C.; Oleinick, N. L.; Kinsella, T. J., Photodynamic therapy: a new concept in medical treatment. *Brazilian journal of medical and biological research*. **2000**, 33 (8), 869-80.

9. Kato, H.; Okunaka, T.; Konaka, C., Photodynamic therapy for bronchogenic carcinoma. *Nihon Geka Gakkai zasshi* **1997**, 98 (1), 36-40.

10. Runfola, M. A.; Weber, T. K.; Rodriguez-Bigas, M. A.; Dougherty, T. J.; Petrelli, N. J., Photodynamic therapy for residual neoplasms of the perianal skin. *Dis Colon Rectum* **2000**, 43 (4), 499-502.

11. Popovic, E. A.; Kaye, A. H.; Hill, J. S., Photodynamic therapy of brain tumors. *Journal of clinical laser medicine & surgery* **1996**, 14 (5), 251-61.

12. Davis, M.E., Z. Chen, and D.M. Shin, Nanoparticle therapeutics: an emerging treatment modality for cancer. *Nature Reviews Drug Discovery*, **2008**. 7(9): p. 771-782.

13. Gabizon, A., et al., Prolonged Circulation Time and Enhanced Accumulation in Malignant Exudates of Doxorubicin Encapsulated in Polyethylene-glycol Coated Liposomes. *Cancer Research*, **1994**. 54(4): p. 987-992.

14. Gao, X., et al., In vivo cancer targeting and imaging with semiconductor quantum dots. *Nat Biotech*, **2004**. 22(8): p. 969-976.

15. Liong, M., et al., Multifunctional Inorganic Nanoparticles for Imaging, Targeting, and Drug Delivery. *Acs Nano*, **2008**. 2(5): p. 889-896.

16. R. Biolo, G. Jori, M. Soncin, B. Rihter, M.E. Kenney, M.A. Rodgers, Effect of photosensitizer delivery system and irradiation parameters on the efficiency of photodynamic therapy of B16 pigmented melanoma in mice, *Photochem. Photobiol*. 63 **1996,** 224–228.

17. D.Wohrle,S.Muller,M.Shopova,V.Mantareva,G.Spassova,F.Vietri,F.Ricchelli,G.Jori, Effect of delivery system on the pharmacokinetic and phototherapeutic properties of bis(methyloxyethyleneoxy) silicon-phthalocyanine in tumor-bearing mice, *J. Photochem. Photobiol.*, B 50 **1999,** 124–128.

18. G. Birrenbach, P.P. Speiser, Polymerized micelles and their use as adjuvants in immunology, *J. Pharm. Sci*. 65 **1976** ,1763–1766.

19. P. Courvreur, L. Grislain, V. Lenaerts, F. Brasseur, P. Guiot, A. Biornacki, Biodegradable polymeric nanoparticles as drug carrier for antitumor agents, in: P Guiot, P. Corvreur (Eds.), Polymeric Nanoparticles and Microspheres, Boca Raton, *CRC Press*; **1986**, pp. 27–93.

20. A.T. Florence, N. Hussain, Transcytosis of nanoparticle and dendrimer delivery systems: evolving vistas, *Adv. Drug Deliv*. Rev. 50 (Suppl 1) **2001**, S69–S89.

21. Bechet, D.; Couleaud, P.; Frochot, C.; Viriot, M. L.; Guillemin, F.; Barberi-Heyob, M. *Trends Biotechnol*. **2008**, 26, 612.

22. Belfield, K. D.; Yao, S.; Bondar, M. V., Two-photon Absorbing Photonic Materials: From Fundamentals to Applications. *Adv Polym Sci* **2008**, 213, 97-156.

23. Bisland, S. K.; Lilge, L.; Lin, A.; Rusnov, R.; Bogaards, A.; Wilson, B. C., Metronomic photodynamic therapy as a new paradigm for photodynamic therapy: Rationale and preclinical evaluation of technical feasibility for treating malignant brain tumors *Photochem Photobiol* **2004**, 80 (2), 373-373.

24. Bhawalkar, J. D.; Kumar, N. D.; Zhao, C. F.; Prasad, P. N., Two-photon photodynamic therapy. *Journal of clinical laser medicine & surgery* **1997**, 15 (5), 201-4.

25. Yue, X.; Yanez, C. O.; Yao, S.; Belfield, K. D., Selective cell death by photochemically induced pH imbalance in cancer cells. *J Am Chem Soc.* **2013**, 135 (6), 2112-5.

26. Wang, X. H.; Morales, A. R.; Urakami, T.; Zhang, L. F.; Bondar, M. V.; Komatsu, M.; Belfield, K. D., Folate Receptor-Targeted Aggregation-Enhanced Near-IR Emitting Silica Nanoprobe for One-Photon in Vivo and Two-Photon ex Vivo Fluorescence Bioimaging. *Bioconjugate Chemistry* **2011**, 22 (7), 1438-1450.

27. Yanez, C. O.; Morales, A. R.; Yue, X. L.; Urakami, T.; Komatsu, M.; Jarvinen, T. A. H.; Belfield, K. D., Deep Vascular Imaging in Wounds by Two-Photon Fluorescence Microscopy. *Plos One.* **2013**, 8 (7).

28. Schenke-Layland, K.; Riemann, I.; Damour, O.; Stock, U. A.; Konig, K., Two-photon microscopes and in vivo multiphoton tomographs - Powerful dicagnostic tools for tissue engineering and drug delivery. *Advanced Drug Delivery Reviews* **2006**, 58 (7), 878-896.

29. Belfield, K. D.; Yanez, C. O.; Yao, S.; Huang, Z. L.; Corredor, C. C., Improved photosensitive polymeric materials for 3-D WORM optical data storage using two-photon fluorescent writing and readout. *Abstr Pap Am Chem* S **2007**, 233. 9.

30. Belfield, K. D.; Yanez, C. O.; Andrade, C. D.; Yao, S., POLY 598-New photosensitive polymeric materials for two-photon 3-D WORM optical data storage. *Abstr Pap Am Chem* S **2008**, 236.

31. Yanez, C. O.; Andrade, C. D.; Yao, S.; Luchita, G.; Bondar, M. V.; Belfield, K. D., Photosensitive Polymeric Materials for Two-Photon 3D WORM Optical Data Storage Systems. *Acs Appl Mater Inter* **2009**, 1 (10), 2219-2229.

32. Mennel, S.; Barbazetto, I.; Meyer, C. H.; Peter, S.; Stur, M., Ocular photodynamic therapy - Standard applications and new indications (Part 1). *Ophthalmologica* **2007**, 221 (4), 216-226.

33. Brown, S. B.; Brown, E. A.; Walker, I., The present and future role of photodynamic therapy in cancer treatment. *Lancet Oncol* **2004**, 5 (8), 497-508.

34. Wilson, B. C.; Patterson, M. S., The physics, biophysics and technology of photodynamic therapy. *Phys Med Biol* **2008**, 53 (9), R61-R109.

35. Maruo, S.; Nakamura, O.; Kawata, S., Three-dimensional microfabrication with two-photon-absorbed photopolymerization. *Optics Letters* **1997**, 22 (2), 132-134.

36. Parthenopoulos, D. A.; Rentzepis, P. M., 3-Dimensional optical storage memory. *Science* **1989**, 245 (4920), 843-845. 88.

37. Strickler, J. H.; Webb, W. W., 3-Dimensional optical-data storage in refractive media by 2-photon point excitation. *Optics Letters* **1991**, 16 (22), 1780-1782.

38. Wagnieres, G. A.; Star, W. M.; Wilson, B. C., In vivo fluorescence spectroscopy and imaging for oncological applications. *Photochem Photobiol* **1998**, 68 (5), 603-632.

39. Allison, R. R.; Downie, G. H.; Cuenca, R.; Hu, X. H.; Childs, C. J. H.; Sibata, C. H., Photosensitizers in clinical PDT. *Photodiagn Photodyn* **2004**, 1 (1), 27-42.

40. Rumi, M.; Ehrlich, J. E.; Heikal, A. A.; Perry, J. W.; Barlow, S.; Hu, Z. Y.; McCord-Maughon, D.; Parker, T. C.; Rockel, H.; Thayumanavan, S.; Marder, S. R.; Beljonne, D.; Bredas, J. L., Structure-property relationships for two-photon absorbing chromophores: Bis-donor diphenylpolyene and bis(styryl)benzene derivatives. *Journal of the American Chemical Society* **2000**, 122 (39), 9500-9510.

41. Albota, M.; Beljonne, D.; Bredas, J. L.; Ehrlich, J. E.; Fu, J. Y.; Heikal, A. A.; Hess, S. E.; Kogej, T.; Levin, M. D.; Marder, S. R.; McCord-Maughon, D.; Perry, J. W.; Rockel, H.; Rumi, M.; Subramaniam, C.; Webb, W. W.; Wu, X. L.; Xu, C., Design of organic molecules with large two-photon absorption cross sections. *Science* **1998**, 281 (5383), 1653-1656.

42. Audebert, P.; Kamada, K.; Matsunaga, K.; Ohta, K., The third-order NLO properties of D-pi-A molecules with changing a primary amino group into pyrrole. *Chem Phys Lett* **2003**, 367 (1-2), 62-71.

43. Cherioux, F.; Maillotte, H.; Dudley, J. M.; Audebert, P., Enhancement of non-resonant non-linear refractive index with reduction of absorption in push-pull molecules by reduction of their donor group strength. *Chem Phys Lett* **2000**, 319 (5-6), 669-673.

44. Yang, W. J.; Kim, D. Y.; Jeong, M. Y.; Kim, H. M.; Jeon, S. J.; Cho, B. R., 2,6-Bis(styryl)anthracene derivatives with large two-photon cross-sections. *Chemical Communications* **2003**, (20), 2618-2619.

45. Mongin, O.; Porres, L.; Charlot, M.; Katan, C.; Blanchard-Desce, M., Synthesis, fluorescence, and two-photon absorption of a series of elongated rodlike and banana-shaped quadrupolar fluorophores: A comprehensive study of structure-property relationships. *Chem-Eur J.* **2007**, 13 (5), 1481-1498.

46. C. Mattson Porth (Ed.), Lippincott–Raven, Pathophysiology: concepts of altered health states, 8th Edition. Philadelphia, 1998.

47. Schussler, G. C., et al., Phosphaturia in hypercalcemic breast cancer patients. *The Journal of Clinical Endocrinology & Metabolism* **1972,** 35(4) 497-504.

48. Norenstedt S, Granath F, Ekbom A, et al, Breast cancer associated with primary hyperparathyroidism: A nested case control study. *Clinical Epidemiology*. **2011**; 3:103-106.

49. Sharretts JM, Kebebew E, Simonds WF. Parathyroid cancer. *Seminars in oncology*. **2010**;37(6):580-590.

50. Themelis, D. G., et al. "Direct determination of phosphate in urine by sequential-injection analysis with single on-line dilution-calibration method and photometric detection." *Anal Biochem* **2004**, 330(2): 193-198.

51. Elisa Lozano-Chaves, M.P. Hernández-Artiga, A. Muñoz-Leyva, Spectrophotometric phosphate determination in urine by ligand exchange extraction, *Microchim. Acta* **1994,** 116 91–99.

52. A. Classen, W.D. Miersch, A. Hesse, Simultaneous determination of urinary phosphate and sulphate by ion-chromatography, *J. Clin. Chem. Clin. Biochem*. 28 **1990** 91–94.

53. http://www.abcam.com/phosphate-assay-kit-fluorometric-ab102508-references.html.

54. Gilbert, L., et al. "Development of an amperometric assay for phosphate ions in urine based on a chemically modified screen-printed carbon electrode." *Anal Biochem* **2009** 393(2): 242-247.

55. Hatai, J., et al. "An inorganic phosphate (Pi) sensor triggers 'turn-on' fluorescence response by removal of a Cu2+ ion from a Cu2+-ligand sensor: determination of Pi in biological samples." *Tetrahedron Letters* **2012** 53(33): 4357-4360.

56. Slowing, II, et al. "Mesoporous silica nanoparticles as controlled release drug delivery and gene transfection carriers." *Adv Drug Deliv Rev* **2008**. 60(11): 1278-1288.

57. Stober, W.; Fink, A.; Bohn, E., Controlled Growth of Monodisperse Silica Spheres in Micron Size Range. *J Colloid Interf Sci* **1968**, 26 (1), 62.

58. Larson, D. R.; Ow, H.; Vishwasrao, H. D.; Heikal, A. A.; Wiesner, U.; Webb, W. W., Silica nanoparticle architecture determines radiative properties of encapsulated fluorophores. *Chem Mater* **2008**, 20 (8), 2677-2684.

59. W. Stober, A. Fink, E. Bohn, Controlled growth of monodisperse silica spheres in the micron size range. *J. Colloid Interface Sci*. 26 (**1968**) 62.

60. Yanez, C. O., et al. "Characterization of novel sulfonium photoacid generators and their microwave-assisted synthesis." *Chem Commun (Camb)* **2009**. (7): 827-829.

61. H.M. Pitt, U.S. Patent 2 807 648, sept. 24, 1957.

62. W. Hahn and R. Stroh, U.S. Patent 2 833 827, May 6, 1958.

63. T. Oishi, M. Mori, and Y. Ban, Chem. Synthesis of alkaloids. *Pharm. Bull*., 19 (9), 1863 (**1971**).

64. L.G. Makarova and A. N. Nesmeyanov, lzv. Akad, Nauk SSSR, Ser. Synthesis of aryloxysulphoxonium salts. *Khim*., 617 (**1945**).

65. J. W. Knapczyk and W. E. McEwen, *J. Am. Chem. Soc*., 91 (1), 145 (**1969**).

66. Crivello, J. V.; Lam, J. H. W. Abstract of papers of the American chemical society. *J. Org. Chem*. **1978**, 43, 3055.

67. F. M. Beringer and P. Bodlaender, Iodanes with Cu species ligated to the hypervalent iodine (III) atom. *J. Org. Chem*., 34, 1981 (**1969**).

68. M.C. Caserio, D. L. Glusker, and J.D. Roberts, *J. Am. Soc.*, 81, 336 (**1959**).

69. Caumes, C., T. Hjelmgaard, O. Roy, M. Reynaud, D. Servent, C. Taillefumier and S. Faure. "Synthesis and binding affinities for sst receptors of cyclic peptoid SRIF-mimetics." *MedChemComm* **2012**, 3(12): 1531.

70. R. Kumar, I. Roy, T. Y. Ohulchanskyy, L. N. Goswami, A. C. Bonoiu, E. J. Bergey, K. M. Tramposch, A.Maitra, and P. N. Prasad, "Covalently dye-linked, surface-controlled, and bioconjugated organically modified silica nanoparticles as targeted probes for optical imaging," *ACS Nano* 2(3), **2008,** 449–456.

71. Sheikbahae, M.; Said, A. A.; Wei, T. H.; Hagan, D. J.; Vanstryland, E. W. Sensitive measurement of optical nonlinearities using a single beam. Ieee . *J Quantum Elect* **1990**, 26, 760-769.

72. Dennis E.J.G.J. Dolmans, Dai Fukumura and Rakesh K. Jain , Photodynamic therapy for cancer. *Nature Reviews Cancer***, 2003**, 3 380-387.

73. Aisling E. O'Connor1, Margaret M. Mc Gee1, Yury Likar2, Vladimir Ponomarev2, John J. Callanan3, Donal F. O'shea4, Annette T. Byrne5 and William M. Gallagher (Mechanism of cell death mediated by a BF2-chelated tetraaryl-azadipyrromethene photodynamic therapeutic:dissection of the apoptotic pathway in vitro and in vivo. *Int. J. Cancer*. **2012**, 130 705-715

74. Zhu, T. C.; Finlay, J. C.; Hahn, S. M. determination of the distribution of light, optical properties, drug concentration, and tissue oxygenation in-vivo in human prostate during motexafin lutetium-mediation photodynamic therapy *J. Photochem. Photobiol*. *B: Biol*. **2005**, 79, 231.

75. Moore, R. B.; Chapman, J. D.; Mercer, J. R.;Mannan, R. H.; Wiebe, L. I.; McEwan, A. J.; McPhee, M. S. Measurement of PDT-induced hypoxia in Dunning prostate tumors by iodine-123 iodoazomycin arabinoside. *J. Nucl. Med*. **1993**, 34, 405.

76. Brown, J. M.; William, W. R. Exploiting tumour hypoxia in cancer treatment. *Nat. Rev. Cancer* **2004**, 4, 437.

77. Sharma SV, Bell DW, Settleman J, Haber DA. Epidermal growth factor receptor mutations in lung cancer. *Nat. Rev. Cancer*. **2007**; 7:169–181.

78. M. Ferrari, "Cancer nanotechnology: opportunities and challenges," *Nat. Rev. Cancer* **2005;** 5(3), 161–171.

79. E. Ruoslahti, S. N. Bhatia, and M. J. Sailor, "Targeting of drugs and nanoparticles to tumors," *J. Cell Biol*. **2010;** 188(6), 759–768.

80. T. Y. Ohulchanskyy, I. Roy, K. T. Yong, H. E. Pudavar, and P. N. Prasad, "High-resolution light microscopy using luminescent nanoparticles," *Wiley Interdiscip Rev Nanomed Nanobiotechnol.* **2010**; 2(2), 162–175.

81. D. J. Bharali, I. Klejbor, E. K. Stachowiak, P. Dutta, I. Roy, N. Kaur, E. J. Bergey, P. N. Prasad, and M. K. Stachowiak, "Organically modified silica nanoparticles: a nonviral vector for in vivo gene delivery and expression in the brain," *Proc. Natl. Acad. Sci. U.S.A.* **2005**; 102(32), 11539–11544.

82. S. Kim, T. Y. Ohulchanskyy, H. E. Pudavar, R. K. Pandey, and P. N. Prasad, "Organically modified silica nanoparticles co-encapsulating photosensitizing drug and aggregation-enhanced two-photon absorbing fluorescent dye aggregates for two-photon photodynamic therapy," *J. Am. Chem. Soc*. **2007**;129(9), 2669–2675 ().

83. T. Y. Ohulchanskyy, I. Roy, L. N. Goswami, Y. H. Chen, E. J. Bergey, R. K. Pandey, A. R. Oseroff, and P. N. Prasad, "Organically modified silica nanoparticles with covalently incorporated photosensitizer for photodynamic therapy of cancer," *Nano Lett*. **2007**; 7(9), 2835–2842.

84. J. Qian, X. Li, M. Wei, X. Gao, Z. Xu, and S. He, "Bio-molecule-conjugated fluorescent organically modifiedsilica nanoparticles as optical probes for cancer cell imaging," *Opt. Express.* **2008**; 16(24), 19568–19578.

85. Hasan, T. Photodynamic Therapy: Basic Principles and Clinical Applications; *Mercel Dekker*: New York, **1992**.

86. Malich, G.; Markovic, B.; Winder, C., The sensitivity and specificity of the MTS tetrazolium assay for detecting the in vitro cytotoxicity of 20 chemicals using human cell

lines. *Toxicology* **1997**, 124 (3), 179-192.

87. B. Tuleva, E. Vasileva-Tonkova, and D. Galabova, "A specific alkaline phosphatase from Saccharomyces cerevisiae with protein phosphatase activity," *FEMS Microbiology Letters*, **1998**; vol. 161, no. 1, pp. 139–144,.

88. Mathis, G., Probing molecular interactions with homogeneous techniques based on rare earth cryptates and fluorescence energy transfer. *Clinical Chem.*, **1995**. 41(9): p. 1391-1397.

89. Clegg, R. M. Fluorescence resonance energy transfer and nucleic acids. *Methods Enzymol*. **1992**; 211, 353-388.

90. Selvin, P. R. Fluorescence resonance energy transfer. *Methods Enzymol*. **1994**; 246, in press.

91. Swierczewska, M., et al. "The design and application of fluorophore-gold nanoparticle activatable probes." *Phys Chem Chem Phys.* **2011**; 13(21): 9929-9941.

92. Burda C, Chen XB, Narayanan R, El-Sayed MA. Chemistry and properties of nanocrystals of different shapes. *Chem Rev.* **2005**; 105(4):1025–1102.

93. Daniel MC, Astruc D. Gold nanoparticles: assembly, supramolecular chemistry, quantum size-related properties, and applications toward biology, catalysis, and nanotechnology. *Chem Rev.* **2004**; 104(1):293–346.

94. Homola J. Surface plasmon resonance sensors for detection of chemical and biological species. *Chem Rev.* **2008**; 108 (2):462–493.

95. Njoki PN, Lim IIS, Mott D, Park HY, Khan B, Mishra S, Sujakumar R, Luo J, Zhong C J. Size correlation of optical and spectroscopic properties for gold nanoparticles. *J Phys Chem C*. **2007**; 111(40):14664–14669.

96. Lassiter, S. J.; Stryjewski, W.; Owens, C. V.; Flanagan, J. H.; Hammer, R. P.; Khan, S.; Soper, S. A. Optimization of sequencing conditions using near-infrared lifetime identification methods in capillary gel electrophoresis. *Electrophoresis* **2002**, 23, 1480.

97. Zhu, L.; Stryjewiski, W.; Lassiter, S.; Soper, S. A. Fluorescence multiplexing with time resolved and spectral discrimination using a near IR detector. *Anal. Chem*. **2003**, 75, 2280.

98. Barbieri, R.; Bertini, I.; Cavallaro, G.; Lee, Y. M.; Luchinat, C. Rosato, A. paramagnetically induced residual dipolar couplings for solution structure determination of lanthanide binding proteins. *J. Am. Chem. Soc*. **2002**, 124, 5581.

99. Bemquerer, M. P.; Bloch, C.; Brito, H. F.; Teotonio, E. E. S.; Miranda, M. T. M. Luminescence investigation of binding Eu and Tb ions with the synthetic peptides derived from the plant thionins. J. *Inorg. Biochem.* **2002**, 9, 363-370.

100. Franz, K. J.; Nitz, M.; Imperiali, B. Lanthanide-binding tags as versatile protein coexpression probes. *ChemBioChem* **2003**, 4, 265.

101. Selvin, P.R., Lanthanide-based resonance energy transfer. IEEE J. of Selected Topics in Quantum Electronics: *Lasers in Biology*, **1996**. 2(4): p. 1077-1087.

102. Sankararamakrishnan, N., et al. "One pot green synthetic route for the preparation of cetyl trimethyl ammonium bromide grafted multiwalled carbon nanotubes and their application towards defluoridation." *RSC Advances.* **2013**. 3(44): 22421.

103. Babak Nikoobakht and and Mostafa A. El-Sayed, Preparation and growth mechanism of gold nanorods (NRs) using seed-mediated growth. *Chemistry of Materials* **2003** 15 (10), 1957-1962.

104. Ivan H. El-Sayed et al. Calculated Absorption and scattering properties of gold nanoparticles of different size, shape, and composition: application in biological Imaging and biomedicine. *J. Phys. Chem. B* **2006** 110, 7238-7248.

105. M. Santos, B.C. Roy, H.C. Goicoechea, A.D. Campiglia, S. Mallik, Aninvestigation on the analytical potential of polymerized liposomes bound to lanthanide ions for protein analysis. *J. Am. Chem. Soc.* **2004** 10738-10745.

106. Hun-Tsung Chang, et al. detection nucleoside monophosphate through surface assisted laser desoption/ionization mass spectrometry using CTAB-adorbed gold nanoparticles. J. Chinese chemical society. **2011**, 58, 761-768.

107. Mahajan, P. G., et al. "Cetyltrimethylammonium bromide capped 9-anthraldehyde nanoparticles for selective recognition of phosphate anion in aqueous solution based on fluorescence quenching and application for analysis of chloroquine." *J Fluoresc* **2015** 25(1): 31-38.

108. Dewhirst, M. W.; Cao, Y.; Moeller, B., Cycling hypoxia and free radicals regulate angiogenesis and radiotherapy response. *Nat Rev Cancer* **2008**, 8 (6), 425-437.